Title

Microfluidics System for Cell Reprogramming

Author

Chen, Binru

Publication Date

2023

Peer reviewed|Thesis/dissertation

UNIVERSITY OF CALIFORNIA

Los Angeles

Microfluidics System for Cell Reprogramming

A dissertation submitted in partial satisfaction of the requirements for the degree Doctor of Philosophy in Bioengineering

by

Binru Chen

2023

ABSTRACT OF THE DISSERTATION

Microfluidics System for Cell Reprogramming

by

Binru Chen

Doctor of Philosophy in Bioengineering

University of California, Los Angeles, 2023

Professor Song Li, Chair

Cell reprogramming has great potential in biomedical applications, including disease modeling, drug screening, tissue regeneration and personalized medicine. A major limitation of cell reprogramming is the low conversion efficiency due to epigenetic barriers. Extensive research has focused on how to enhance reprogramming; in addition to biochemical cues, mechanical stimulation can also modulate epigenetic state and various cell functions through distinct mechanisms that are not fully understood. Here I developed novel microfluidics devices to induce the deformation of cell nucleus in a high throughput manner, by forcing cells moving through microchannels with well-defined sizes, and studied the direct effect of nuclear deformation on cell reprogramming. This milli-second nuclear deformation promotes the reprogramming of mouse fibroblasts into neuronal cells, which are attributed to the transient decrease of histone H3 lysine 9 trimethylation and DNA methylation after squeezing. This epigenetic change and the enhancement of reprogramming are dependent on the geometric features of microchannels cross-sections. To optimize the microfluidic device design to achieve

the highest reprogramming efficiency, I constructed a second-order quadratic model and parabolic response surface. By integrating the experiment results and theoretical prediction, I generated a design guideline for the cross-section geometry of microfluidic channels that can be generalized for various cell types, which was validated by reprogramming mouse macrophages into neuronal cells. This innovative mechanobiology approach using microfluidic device for epigenetic modulation and reprogramming enhancement, together with the parabolic response surface-based optimization process, open a new avenue for cell engineering.

The dissertation of Binru Chen is approved.

Dino Di Carlo

Tzung Hsiai

Amy Catherine Rowat

Song Li, Committee Chair

University of California, Los Angeles

2023

Table of Contents

List of Figures

Chapter I

Chapter II

Chapter III

List of Tables

Acknowledgements

First, I would like to express my deepest gratitude to my advisor, Dr. Song Li, for his unwavering support, insightful suggestions, and constant encouragement throughout my PhD career. I am truly grateful for your guidance.

I am also immensely grateful to my committee members, Dr. Dino Di Carlo, Dr. Tzung Hsiai and Dr. Amy Rowat, for their valuable advice and insights on my research. Your guidance kept me on the right track, and I do appreciate it.

Special thanks go to my colleagues and friends at Li Lab, especially Dr. Yang Song and Dr. Jennifer Soto, who taught me all the necessary biological experimental techniques, helping me make a smooth transition from electrical engineering to bioengineering. Our friendship and collaboration made this journey enjoyable and rewarding.

I extend my gratitude to my collaborators, Dr. Chih-Ming Ho, and his student Brian Jeong on PRS optimization; Dr. Yingxiao Wang and his postdocs, Dr. Qin Peng and Dr. Longwei Liu on FRET experiment; Dr. Liang Gao and his student Yayao Mao on 3D imaging; Dr. Amy Rowat and her student Chau Ly on qDC experiment; Dr. Dino Di Carlo and his student Vivek Rajasenan on high speed camera and hydrodynamic stretching devices; Dr. Aydogan Ozcan and his student Yuzhu Li on imaging processing. Their support and contribution have been crucial to my research.

To my family, especially my Fiancé and my mom, thank you for your endless love, patience, and understanding during this challenging process. Your unwavering belief in my capabilities has been my driving force.

Lastly, my sincere thanks to the Department of Bioengineering at UCLA, for providing me with a stimulating and supportive academic environment.

This journey has been a collective effort, and each one of you has been a part of this. Thank you.

This research was supported by UCLA HSSEAS startup funding, NIH grant GM143485 and UCLA Summer Mentored Research Fellowship, 2021.

Chapter II includes data and text from published paper, Song, Y., Soto, J., Chen, B., Hoffman, T., Zhao, W., Zhu, N., Peng, Q., Liu, L., Ly, C., Wong, P.K., Wang, Y., Rowat, A.C., Kurdistani, S.K. and Li, S., 2022. "Transient nuclear deformation primes epigenetic state and promotes cell reprogramming." *Nature Materials*, 21(10), pp.1191-1199. Y.S., S.L., P.K.W. and S.K.K. designed the experiments. Y.S., J.S., B.C., W.Z., N.Z., Q.P., L.L. and C.L. performed the experiments. Y.S., J.S., B.C., W.Z., T.H. and Q.P. analysed the data. Y.S., P.K.W., Y.W., A.C.R., C.L., S.K.K. and S.L. contributed to data interpretation and discussion. Y.S., J.S. and S.L. wrote the manuscript.

Chapter III includes data and text from an unpublished manuscript in preparation.

Appendix includes data and text from manuscript, Soto, J., Song, Y., Wu, Y., Chen, B., Park, H., Akhtar, N., Wang, P.Y., Hoffman, T., Ly, C., Sia, J., Wong, S.Y., Kelkhoff, D.O., Chu, J., Poo, M.M., Downing, T.L., Rowat, A.C. and Li, S. "Reduction of Intracellular Tension and Cell Adhesion Promotes Open Chromatin Structure and Enhances Cell Reprogramming." Manuscript under review. J.S. and S.L. designed the experiments. J.S., Y.S., B.C., H.P., N.A., P.Y.W., C.L., S.W., D.O.K. and J.C. performed the experiments. J.S., Y.S., Y.W., B.C., H.P., P.Y.W., T.H., C.L., J.S., S.W. and D.O.K. analyzed the data. J.S., M.P., T.D., A.R. and S.L. contributed to data interpretation and discussion. J.S. and S.L. wrote the manuscript.

Vita

Education

Bachelor of Engineering, Microelectronics Science & Engineering,

South University of Science & Technology of China *Mar 2011 – Jun 2015*

Honors & Awards

First place, Easton Innovation Challenge, Healthcare Track, 2023

University of California, Los Angeles

First place, Lowell Milken Institute-Sandler Prize for New Entrepreneurs, 2023

University of California, Los Angeles

Summer Mentored Research Fellowship, 2021

University of California, Los Angeles

First Prize, Learning Merit Scholarship, 2014

China Merchants Bank, & South University of Science & Technology of China

Elite Student and Advanced Individual Award, 2014

Zhiren Academy, South University of Science & Technology of China

---

Research experience

Graduate Student Researcher *July 2017 – Present*

Song Li Lab, University of California, Los Angeles

Research Assistant *Sept 2013 – Aug 2016*

Advanced Biomaterials Lab, South University of Science & Technology of China

---

Publications

1. Soto, J., Song, Y., Wu, Y., **Chen, B.**, Park, H., Akhtar, N., Wang, P.Y., Hoffman, T., ... & Li, S. Reduction of Intracellular Tension and Cell Adhesion Promotes Open Chromatin Structure and Enhances Cell Reprogramming. Manuscript under review.
2. Song, Y., Soto, J., **Chen, B.**, Hoffman, T., Zhao, W., Zhu, N., ... & Li, S. (2022). Transient nuclear deformation primes epigenetic state and promotes cell reprogramming. *Nature Materials*, *21*(10), 1191-1199.
3. Song, Y., Soto, J., **Chen, B.**, Yang, L., & Li, S. (2020). Cell engineering: biophysical regulation of the nucleus. *Biomaterials*, *234*, 119743.

Chapter I

Background

Cell reprogramming is a revolutionary scientific technique standing at the forefront of contemporary biological research, which offers transformative implications in the fields of developmental biology, disease modeling, drug discovery, and regenerative medicine. This groundbreaking methodology involves the conversion of differentiated cells back to a pluripotent state or directly to other types of differentiated cells, thereby challenging the long-held dogma of cellular differentiation as an irreversible process. Despite the great potential of cell reprogramming, numerous challenges remained to be overcome, one of the biggest is the low conversion efficiency. Hence, my thesis aims to explore and develop techniques to enhance cell reprogramming, with a focus on the development of a high-throughput microfluidic system for cell reprogramming. In this chapter, an overview of development history, molecular mechanism of cell reprogramming, the effect of biophysical factors on epigenetics and the applications of microfluidics device will be discussed.

1.1 Development history of cell reprogramming

Waddington's landscape In 1957, Conrad Hal Waddington proposed an influential metaphor illustrating the concept of embryonic development, known as Waddington's landscape[1]. His model envisioned cellular differentiation as a ball rolling downhill following a one-way path. According to this model, the cell's developmental journey is governed by strict control mechanisms, which guide it towards a pre-determined and permanent destiny, mirroring the inescapable nature of biological development[2] (Fig. 1.1).

Somatic cell nuclear transfer Cell reprogramming is a groundbreaking area in biological research, originating in the early 20th century, when Hans Spemann and Hilde Mangold demonstrated the concept of embryonic induction, providing the earliest evidence of cellular plasticity[3]. Shortly after the proposal of Waddington's landscape, in 1962, Sir John Gurdon reported the first example of cellular reprogramming through somatic cell nuclear transfer (SCNT), demonstrating that transplantation of a nucleus from a differentiated frog intestinal cell into an enucleated frog egg could generate a viable tadpole, providing the first empirical evidence that the differentiation of a cell could be reversed[4, 5]. In the process of SCNT, the nucleus from a somatic cell is introduced into an enucleated oocyte. Subsequently, the cell begins to divide and forms an embryo genetically identical to the original somatic cell donor. Over three decades later, Ian Wilmut and colleagues reported the first mammal created through the somatic cloning of mammary epithelial cells[6]. These findings elucidated that somatic cell nuclei preserve the entire genetic information, and can be reprogrammed back to an embryonic, pluripotent state through experimental manipulation, challenging the prevailing belief that cellular differentiation is irreversible.

Cell fusion At the same time, researchers demonstrated that the fusion of somatic cells with other cell types can modify their gene expression patterns and initiate reprogramming. This was first reported in 1983 that after fusion with mouse muscle cells, the silenced muscle-specific genes in human amniocytes were activated[7]. Further studies indicated that the fusion of somatic cells, like fibroblasts and T lymphocytes, with pluripotent cells such as embryonic stem cells (ES cells), could trigger their epigenetic reprogramming, which allowed them to express pluripotency-associated genes, suggesting that pluripotent stem cells (PSCs) may hold the

potential to reprogram somatic cells towards pluripotency[8, 9]. These findings proposed that the presence of one or more reprogramming factors could ‘erase’ the 'memories' of somatic cells.

Transdifferentiation Further proof of the presence of reprogramming factors was provided by studies demonstrating direct conversion of mammalian cells through the introduction of a single transcription factor[10]. The process of cDNA subtraction was used to identify novel genes specific to myoblasts, leading to the discovery of three genes predominantly expressed in proliferating myoblasts. Remarkably, the ectopic expression of one of these genes, myoblast determination protein (MYOD), was found to be sufficient to convert mouse fibroblasts into myoblasts, as evidenced by the expression of myoblast marker genes such as myosin. Years later, research showed that the ectopic expression of the erythroid transcription factor GATA-binding protein 1 (GATA1) could transform myeloblasts into precursors of megakaryocytes and erythrocytes[11]. Furthermore, either CCAAT/enhancer-binding protein-α (CEBPα) or CEBPβ could induce the transformation of B lymphocytes into macrophages[12]. This process, wherein somatic cells are converted into a different somatic lineage, is known as transdifferentiation. It has been demonstrated in *Drosophila melanogaster* as well. For example, a mutation in the homeotic gene *Antennapedia* was identified as the cause for the transformation of an antenna into a leg[13-18]. Additionally, the targeted expression of a gene analogous to the mammalian paired box 6 (PAX6) gene resulted in the formation of ectopic eye structures in mutant *D. melanogaster* that were originally eyeless[19]. These investigations offered compelling proof that transcription factors, particularly those that serve as master regulators of cellular identity, have the capacity to alter cell fate.

iPSC cell reprogramming In 2006, Shinya Yamanaka and his team at Kyoto University made a groundbreaking discovery by introducing four transcription factors (Oct4, Sox2, Klf4, and c-

Myc), known as Yamanaka or OSKM facors, into mouse fibroblasts, reprogramming them into a pluripotent state similar to embryonic stem cells [20]. These cells, known as induced pluripotent stem cells (iPSCs), can differentiate into various cell types, opening up new possibilities for regenerative medicine and disease modeling. In 2007, Yamanaka's team and another group led by James Thomson successfully generated human iPSCs [21, 22]. Shinya Yamanaka was awarded the Nobel Prize in Physiology or Medicine in 2012 for this discovery.

Direct cell reprogramming In addition to iPSC reprogramming, researchers have developed methods to directly convert one differentiated cell type into another without reverting to a pluripotent state, known as direct reprogramming, by introducing specific transcription factors. Examples include the conversion of fibroblasts into neurons[23], cardiomyocytes[24], or hepatocytes[25]. Direct reprogramming provides a rapid and potentially more efficient approach to cellular transformation compared to iPSC reprogramming. Direct reprogramming offers unique advantages in the context of tissue repair, primarily due to its speed and efficiency[2]. Unlike iPSC reprogramming which requires the isolation of somatic cells, reprogramming into a pluripotent state, and subsequent differentiation into a different lineage, direct reprogramming could potentially allow for in-situ cell conversion within the desired tissue. This method bypasses the intermediate pluripotent state and eliminates the need for ex vivo cell expansion and transplantation[26, 27] (Fig. 1.2).

Despite successful demonstrations of direct reprogramming for various cell types both in vitro and in vivo[28-30], several challenges need to be overcome before the technique can be adopted in clinical applications. Current limitations include relatively low conversion efficiency, the immaturity of reprogrammed cells[31, 32], a lack of safe delivery methods, potential depletion of the starting cell population, and an inability to precisely guide differentiation towards a desired cell

subtype. Nevertheless, considerable progress has been made in advancing this technology for regenerative medicine applications. Importantly, our understanding of the molecular mechanisms governing direct reprogramming has substantially improved, providing critical knowledge to further refine and control cell identity manipulation.

1.2 Roles of transcription factors in cell reprogramming

To optimize cell reprogramming, a thorough understanding of the molecular mechanisms that govern this process is crucial. Cell reprogramming by using transcription factors (TFs) leads to a swift reconfiguration of the epigenetic and transcriptional profile of the resident cell. In order to activate the gene regulatory network of the target cell, TFs must gain access to genes that have been developmentally silenced (in heterochromatic or closed chromatin conformations). Therefore, numerous reprogramming approaches employ pioneer factors, which are capable of interacting with inaccessible chromatin. These pioneer factors can recruit chromatin remodelers and activators to open closed chromatin, thereby facilitating the binding of other standard transcription factors and the conversion of cell fate[27, 33, 34] (Fig. 1.3).

For example, in iPSC reprogramming, a comprehensive analysis of the binding events of the OSKM factors indicates that Oct4, Sox2, and Klf4 function as pioneer factors by binding to inaccessible chromatin regions[35]. The binding of c-Myc occurs in accessible chromatin regions and is not necessary for the reprogramming process, yet it cooperatively enhances the occupancy of Oct4, Sox2, and Klf4 sites where all factors are jointly bound. In direct reprogramming, Gata4 in cardiac reprogramming[36] and Ascl1 in neuronal reprogramming[23] serve as examples of pioneer factors. Pioneer factors can be classified as ‘on-target’ or ‘off-target’ based on their binding

specificity. In neuronal reprogramming, Ascl1 acts as an ‘on-target’ pioneer factor as it binds to lineage-specific target sites no matter if these sites are in open or closed chromatin regions in the starting cell[37]. In contrast, in iPSC reprogramming, Oct4 acts an ‘off-target’ pioneer factor as it binds less specifically to closed chromatin regions[35]. Pioneer factors also exhibit varying potency in the reprogramming process. For instance, Ascl1 itself can reprogram fibroblasts into neurons[38], while it is required to have the co-binding of Mef2 and Tbx5 with Gata4 (GMT) to activate the conversion of cardiomyocytes from fibroblasts[39].

Transcription factors are able to work together to activate gene expression and facilitate the cell reprogramming. For instance, Ascl1 can recruit Brn2 to numerous neuronal target sites, thereby inducing the reprogramming process to obtain induced neurons (iNs)[37]. In the example of cardiac reprogramming, by the forced expression of the Akt1, Gata4, Hand2, Mef2c, and Tbx5 (AGHMT)[40], at least two transcription factors were found at 50% of DNA binding sites[39]. These co-occupied sites demonstrated a stronger association with the heart-related transcription program compared to sites occupied by a single factor. A similar cooperative interaction between reprogramming factors was found in GMT-induced cardiac reprogramming[24], It is observed that the regions bound by Tbx5 and Gata4 demonstrated about a four times the chromatin accessibility compared to the regions bound solely by Tbx5 or Gata4[32]. Moreover, it is reported that transcription factors can refine the binding patterns of other factors. For instance, in cardiac reprogramming with forced expression of GMT, the binding pattern of individual expression of GMT factors differed from the pattern observed when all three factors were expressed simultaneously[32].

While reprogramming factors operate collaboratively, they don't share equal significance in the cell reprogramming process. For example, in neuronal reprogramming with Ascl1, Brn2, and

Myt1l (BAM) factors, the persistent expression of Ascl1 is reported to be more important for the efficient generation of iNs[41]. In cardiomyocyte reprogramming, Mef2c can activate cardiac-specific enhancers[32, 39], compared to Tbx5 and Gata4, plays a crucial role in both of the early activation of cardiac gene expression and the late maturation of induced cardiomyocytes (iCMs). However, Mef2c doesn't have the pioneering capacity to access heterochromatin regions. Consequently, to achieve an efficient cardiac reprogramming, it is necessary to have high Mef2c levels and low Gata4 and Tbx5 levels, both in vitro and in vivo[42-45]. These findings demonstrate that an optimal recipe of reprogramming factors is a key for successful cell reprogramming.

1.3 Epigenetics regulations in cell reprogramming

Epigenetic barrier is a significant factor hindering successful cell reprogramming. These barriers are characterized by a complex network of DNA methylation, histone modifications, chromatin remodeling, and non-coding RNAs that maintain the integrity of cellular identity and regulate gene expression. The established epigenetic signature of a cell type is resistant to change, creating an obstacle in the path of inducing a new cellular identity. The transition from one cell type to another involves overcoming these epigenetic barriers, which requires not only the silencing of genes associated with the original cell identity but also the activation of genes associated with the target cell identity. Research has shown that inefficient or incomplete epigenetic remodeling can lead to partial reprogramming, resulting in a state of cellular limbo, where cells exhibit traits of both the original and target cell types[46, 47]. Therefore, understanding the epigenetic regulations during cell reprogramming is crucial for improving the efficiency and fidelity of cellular reprogramming.

A dramatic change in chromatin accessibility is induced by the forced expression of reprogramming factors, which is a key factor that determines the efficiency of cell reprogramming. Recent studies utilizing Assay for Transposase-Accessible Chromatin using sequencing (ATAC-seq) technology have shown that chromatin remodeling starts as early as 12 hours following the introduction of reprogramming factors, and most changes occurs at distal regions from the transcription start sites[32, 48]. There are three major types of changes of chromatin accessibility, a consistent increase, a consistent decrease, or a transient reconfiguration. After the introduction of reprogramming factors, the transcription repression occurs at the regions defining the start cell type, with a major decrease in chromatin accesibility[48]. In cardiac reprogramming, Regions associated with genes related to cardiac and striated muscle development showed the maximum accessibility at 3 days after induction, while regions associated with cardiac function only displayed a transient increase in accessibility during the initial phase of reprogramming, indicating that additional factors are needed for the maturation of iCM[32]. The collaborative interaction of reprogramming factors is thought to be the cause of the changes in chromatin accessibility during. In cardiac reprogramming, most of the regions that gained accessibility displayed significant enrichment of GMT binding, but some regions bound with GMT also demonstrated decreased chromatin accessibility. This variation is also observed at the regions with the individual binding of Mef2c and Tbx5, indicating a context-dependent effect on chromatin conformation[32]. On the other hand, in neuronal reprogramming, Ascl1 binding appears to solely increase chromatin accessibility[48], due to the intrinsic strong affinity of Ascl1 to the nucleosome[49]. Therefore, changes in chromatin conformation relies on the properties of the transcription factors and the context of the chromatin.

The epigenetic regulation by post-translational modifications of histones, including methylation, phosphorylation, acetylation, and ubiquitylation, are key factors in cell reprogramming. These histone modifications can regulate gene expression by functioning as signals to recruit specific effectors[27, 50] (Fig. 1.4).

The enrichment of trimethylation histone 3 at lysine 4 (H3K4me3) is prevalent at the promoters of transcriptionally active genes. This marks the lineage-specific genes and signals the activation of transcriptional programme of the target cell. In mouse cardiac reprogramming, H3K4me3 marks were promptly deposited at the promoters of cardiac loci, while the removal from the promoters of fibroblast-specific gene occurs at a more gradual pace[51]. In neural progenitor cells (NPCs) reprogramming from mouse fibroblasts, a significant enrichment of H3K4me3 was observed on the Sox1 promoter by day 8, reaching levels akin to those in adult NPCs by day 12[52]. The establishment of H3K4me3 on chromatin appears to be essential for the full conversion of cell fate and serves as a marker of successful reprogramming. Knockdown of *Kmt2b*, which is a histone methyltransferase that catalyzes H3K4me3, during neuronal reprogramming from mouse embryonic fibroblasts substantially lowered the efficiency of iN generation, alternatively resulting in cells pursuing a myocyte fate[53]. Large chromatin domains, up to 60 kb, have been identified with H3K4me3 and predominantly contain cell identity genes. Among the 13 known promoters of induced neural stem cell reprogramming factors, 10 were found within this extensive H3K4me3 domain[54]. Consequently, the identification of these broad H3K4me3 domains and associated genes may aid in discovering new reprogramming factors.

In contrast, the trimethylation of histone 3 at lysine 27 (H3K27me3) is a histone modification closely associated with transcription repression. As such, during cardiac reprogramming, cardiac genes progressively lose H3K27me3 at their promoters, while fibroblast-specific genes gradually

gain H3K27me3 at later stages[51]. The suppression of H3K27me3 methyltransferases through small-molecule inhibitors or siRNA enhances the induction of a cardiogenic programme in mouse cardiac reprogramming mediated by miRNA[55, 56].

The trimethylation of histone 3 at lysine 9 (H3K9me3) is another repressive histone modification which marks heterochromatin. Transcription factors do not bind to the regions marked by H3K9me3, unlike that regions marked with H3K27me3 remain access to transcription factors and RNA polymerase. For example, in human hepatocyte reprogramming, hepatic genes marked by H3K9me3 in fibroblasts resist transcription activation while hepatic genes marked by H3K27me3 show an increase in transcription activation[57, 58]. The expression of hepatic genes can be enhanced during the early stages of reprogramming by knockdown of the H3K9me3 reader RBMX or the writer SUV39H1[58]. Likewise, the efficiency of mouse cardiac reprogramming can be enhanced by treatment of the histone methyltransferase inhibitor UNC0638 to disrupt H3K9me3 deposition at the early stages of reprogramming[59]. Interestingly, erasing H3K9me3 before mouse neuronal reprogramming results in fewer reprogrammed iNs, suggesting that the erasure of H3K9me3 should only be temporary to facilitate cell reprogramming[37].

Histone acetylation is generally associated with a higher activation in gene expression. A specific form, the acetylation of histone 3 at lysine 27 (H3K27ac), distinguishes active enhancers from inactive and poised enhancers. In neuronal and cardiac reprogramming, H3K27ac marks enhancers and demonstrates a strong positive correlation with reprogramming factor binding during the early phases of cell reprogramming[37, 39].

The ubiquitylation of histone H2A at lysine 119 (H2AK119Ub) and histone H2B at lysine 120 (H2BK120ub) has been associated with both activation and suppression of gene transcription, based on the genomic context[60]. In mouse cardiac reprogramming, cardiomyocyte-specific loci

bound by Bmi1 in fibroblasts were marked by the H2AK119Ub, and the same region contained binding sites for Ring1B and Ezh2, both of which are repressive chromatin remodelers[61]. The depletion of Bmi1 resulted in the total elimination of H2AK119Ub at these sites, which significantly increased the reprogramming efficiency of iCM. This suggests that H2K119Ub acts as a barrier to cardiac reprogramming.

Histone modifications often occur in a cooperative manner, with multiple modifications marking the same histone to collectively regulate transcription. For instance, active enhancers are marked by H3K4me1 and H3K27ac, while active promoters are marked by H3K4me3 and H3K27ac. In some scenarios, the same chromatin region may have both repressive and active histone modifications, a phenomenon exemplified by the antagonistic histone modifications H3K4me3 and H3K27me3[62]. These bivalent marks are critical in embryonic development, as they mark lineage-specific genes in stem or progenitor cells. This keeps the genes in a silent but poised transcriptional state, capable of rapid activation upon exposure to appropriate environmental cues[63]. For instance, the bivalent modification was discovered on genes governing the β-cell programme in pancreatic α-cells, suggesting that the poised state of the β-cell transcriptional programme in α-cells could be the reason of easy conversion from α-cells to β-cells[64]. Trivalent chromatin domains marked by H3K27ac, H3K4me1 and H3K9me3, exhibited enhanced accessibility to Ascl1 binding in neuronal reprogramming, thus facilitating its binding to target loci[37]. The enrichment of this trivalent chromatin state on neuron-specific genes in various starting cell types is correlated with a higher efficiency of neuronal reprogramming, suggesting the significance of the trivalent state for Ascl1-induced neuron-specific transcriptional programmes.

DNA methylation is considered as a significant epigenetic barrier in cell reprogramming because it maintains long-lasting cell memories to stabilize the cell identity. A comprehensive reconfiguration of DNA methylation has been observed in cell reprogramming. In cardiac reprogramming, the promoters of two cardiac lineage-defining genes, *Myh6* and *Nppa*, undergo demethylation shortly after the induction of GMT[51]. Similarly, in neuronal reprogramming, forced expression of neuron-inducing factors results in a genomic methylation pattern closely resembling that of mature cortical neurons[65]. In particular, Ascl1 expression triggers de novo methylation of fibroblast-specific gene promoters by boosting the expression of the DNA methyltransferase Dnmt3a and inhibiting Dnmt3a significantly decreased neuronal reprogramming efficiency[65]. In a similar way, a rapid, global alteration in DNA methylation was observed during the initial 10 days of reprogramming of acinar cells to pancreatic β-cells, especially at pancreatic gene loci[66]. Therefore, the reconfiguration of the global DNA methylation landscape mediated by the cooperative interactions of reprogramming factors plays a crucial role in cell reprogramming.

1.4 Mechanotransduction

Mechanotransduction encapsulates the mechanism where cells interpret and translate the mechanical stimuli from the extracellular environment into intracellular biochemical signals to initiate a range of cellular responses. This process is crucial in the regulation of diverse cellular functions during development, regeneration, and disease states[67-69]. Recent studies show that specific cellular structures act as mechanosensors, capturing and responding to mechanical force variations, or as mechanotransducers, generating a chemical signal in response to a mechanical stimulus, as part of the mechanotransduction process[70-75] (Fig. 1.5).

Focal adhesions are one kind of transmembrane receptor that establishes a physical connection between the extracellular matrix (ECM) and the cytoskeleton, which is comprised of large multiprotein complexes. In response to force, the distinct focal adhesion proteins will be recruited to the mechanosensing sites with the conformational change of integrins[76, 77]. Consequently, cells also reorganize their cytoskeleton and generate contractile forces via motor proteins, like myosin, to recalibrate their internal tension and achieve a state of mechanical stability[78, 79]. Therefore, with the potential modulation via biochemical and physical cues present in the microenvironment, focal adhesions serve not only as mechanosensors, but also as mechanotransducers being able to activate signaling pathways that regulate cytoskeletal organization[70, 80]. Actin filament is a significant force-bearing element of the cytoskeleton, which are thought to operate as primary mechanotransmitters by transmitting mechanical signals to the nucleus via the linker of nucleoskeleton and cytoskeleton (LINC) complex to regulate cell behavior[72, 81]. Accordingly, through rapid stress wave propagation, actin filaments function as the primary transmitter for a rapid response to mechanical cues, which enables cells to promptly adapt to the dynamic changes in their surrounding environment[82].

The cell nucleus stores the genetic material and transcriptional machinery of eukaryotic cells, playing a pivotal role in regulation of cell fate and behavior. DNA wraps around histones within the nucleoplasm, creating higher-order structures that occupy specific locations, which can be categorized as either open, transcriptionally active euchromatin, or densely packed, inactive heterochromatin[83]. Enclosed by the nuclear envelope (NE), a double lipid bilayer, the nucleus is interconnected by nuclear pore complexes that facilitate nuclear-cytoplasmic transport[84, 85].

The nuclear lamina, a dense protein network, consists of integral membrane proteins, such as emerin, lamina-associated polypeptide 2, and MAN1, and type V nuclear intermediate filaments,

such as lamins A, B, and C, offering mechanical support to the inner nuclear membrane[86, 87]. Not only associated with various NE proteins and transcriptional regulators, lamins also directly interact with chromatin by tethering lamina-associated chromatin domains to the nuclear periphery[87, 88]. Disruptions in lamins can result in changes of chromatin assembly, such as peripheral heterochromatin loss[89], indicating that lamins can regulate chromatin organization and gene expression. In addition to providing mechanical support to the nucleus, lamins, specifically lamins A and C, anchor the LINC complex, which allows the transmission of mechanical cues from the ECM and cytoskeleton to the nucleus[70, 72, 82, 90].

Additionally, the LINC complex operates as a conserved molecular bridge, spanning the nuclear envelope to physically couple the nucleus with the cytoskeleton[90-92]. The LINC complex consists of two protein families—Sad1/UNC-84 (SUN) and Klarsicht/ANC-1/Syne-1 homology (KASH) domain proteins, which locates in the inner and outer nuclear membranes respectively and are bridged by transmembrane segments[91]. In mammalian cells, researchers have identified five SUN domain proteins and six KASH domain proteins[91]. KASH domain proteins extend into both the cytoplasm and the perinuclear space between the inner and outer nuclear membranes, where they are tethered by SUN domain proteins. The KASH domain proteins extending into the cytoplasm interact with cytoskeletal components, such as actin, microtubules, and intermediate filaments. Conversely, SUN domain proteins span into the perinuclear space and the nucleus, enabling them to interact not only with the nuclear lamina through SUN1, SUN2, and SUN4, but also with chromatin[93].

Collectively, these intracellular structures enable the transmission of forces applied on the cell surface to the nucleus, potentially influencing nuclear structure and function. Recent

investigations have shown the critical role of the nucleus in mechanosensing, mechanotransduction, and disease pathogenesis[72, 94, 95].

1.5 Mechanical regulation of histone modifications

In addition to biochemical signals, mechanical stimuli like substrate stiffness, mechanical stretch, and fluid shear stress not only trigger immediate cellular responses but also induce long-term alterations in the epigenetic state and cell phenotype via biophysical and biochemical modulation of the nucleus and chromatin[96-98]. Chromatin, organized into compact heterochromatin and loosely packed euchromatin regions, is subject to various epigenetic modifications on the amino acid residues of histones. These modifications include acetylation, methylation, phosphorylation, ADP-ribosylation, sumoylation, and ubiquitination[99, 100]. Generally, histone acetylation promotes chromatin decondensation and gene activation[101], while histone methylation at lysine or arginine residues can induce either a more open or closed chromatin structure, based on the methylation site[102]. Histone phosphorylation is known to regulate chromosome condensation and gene activation[103]. Other histone modifications such as ADP-ribosylation and sumoylation can activate or repress gene activation, respectively, while histone ubiquitination typically participates in chromatin dynamics, transcriptional regulation, and DNA repair[104-106]. Additionally, DNA methylation leads to transcription silencing[107]. Collectively, these epigenetic modifications on histones and DNA can flip the on-and-off switch of genes. In this section, how mechanical factors modulate histone modifications to regulate cell plasticity will be discussed.

1.5.1 Substrate stiffness

In various tissues and organs, the stiffness of ECM undergoes dynamic changes. Cells, either local or recruited to the location, are capable of sensing these changes in matrix stiffness and responding by modifying their behavior, as evidenced in instances such as cancer cell migration [108], macrophage polarization[109], and stem cell differentiation[110]. Recent research has shown the significance of ECM stiffness in directing stem cell differentiation and cell reprogramming, achieved through modulating histone modifications and DNA methylation.

Softer matrices, with stiffness less than 2 kPa, can enhance global histone acetylation, thereby facilitating transitions in cell lineage. For instance, when liver stem cells differentiate into hepatocytes, softer substrates elevate acetylation levels at histone H3 lysine 9 (H3K9ac), an active chromatin modification, while reducing H3K4me3 and H3K27me3 level. These early epigenetic changes at the HNF4α promoter enhanced differentiation[111]. The process of reprogramming mesenchymal stem cells (MSCs) into iPSCs is expedited and improved on a softer matrix due to induced changes in the cytoskeleton and nucleus that enhance histone acetylation, particularly H4K16ac[112]. Similar results were observed during the reprogramming of fibroblasts into iPSCs, which could be due to the potential suppression of stress fiber formation in cells cultured on soft substrates[113].

One possible mechanism involves softer matrices promoting global acetylation by elevating the expression of histone acetyltransferase 1 (HAT1) and simultaneously reducing the expression of histone deacetylase 1 (HDAC1), as shown during the conversion of dermal fibroblasts into insulin-producing cells[114]. Conversely, it was reported that human MSCs cultured on stiffer surfaces, with stiffness larger than 25 kPa, showed increased HAT1 expression and decreased expression of HDACs 1, 2, and 3. This results in the induction of the nuclear localization of Yes-

associated protein (YAP), a mechanosensitive transcription factor. In hepatic stellate cells, stiffer substrate activated acetylation via H3K27ac which was dependent on p300, a histone acetyltransferase[115]. The discrepancy in HAT1/HDAC expression and histone acetylation may represent cell type-dependent responses to stiffness and thus requires further research.

One intriguing aspect to explore is the persistence of stiffness-induced histone modifications, or whether they are easily reversible due to dynamic stiffness alterations. Researchers have shown that in MSCs, the histone acetylation levels which is promoted by high HAT1 expression, induced by the stiff substrate, can be maintained for several days. Furthermore, when a substrate is softened from 32.7 kPa to 5.5 kPa after a day of culture, histone acetylation shows a gradual decline but still maintains overall higher levels than softer surfaces even after five days[116]. It's possible that both the initial stiffness and duration of exposure impact histone modifications, thereby affecting cellular phenotypic alterations. Hence, it's crucial to establish the minimum time necessary to induce durable histone modifications under varying circumstances.

In addition to histone acetylation, histone methylation at specific sites may also be regulated by substrate stiffness. For instance, colorectal adenocarcinoma cells cultured on a 0.4 kPa soft matrix exhibited substantially lower H3K4me3 levels compared to those on a stiff surface[117]. Similarly, human fibroblasts on stiff matrices, with a stiffness larger than 50 kPa, displayed higher H3K9me2/3 levels[118]. Furthermore, soft matrices, with a stiffness of 60 kPa, significantly enhanced the phosphorylation of H3 histone, thereby enhancing the mesoderm differentiation of human embryonic stem cells as opposed to stiff matrices with a stiffness of 400 kPa[119]. Despite clear evidence that stiffness modulates histone acetylation and methylation, current knowledge on how stiffness regulates histone ubiquitination, ADP-ribosylation, and sumoylation still remains limited.

In addition to histone modifications, researchers also showed that DNA methylation can be regulated by matrix stiffness. For instance, both umbilical artery smooth muscle cells (SMCs) and alveolar epithelial adenocarcinoma cells cultured on a matrix with a stiffness of 20 kPa exhibited lower DNA methylation levels compared to a softer matrix[117, 120]. However, fibroblasts on a soft matrix with stiffness of 1 kPa showed significantly lower DNA methylation levels compared to those on a stiff plastic surface[114]. Further studies on the effects of stiffness on DNA methylation will shed light on whether the stiffness regulation of DNA methylation is dependent on the cell type.

1.5.2 Mechanical strain

Cells in various tissues such as ligament fibroblasts[121], lung neuroepithelial cells[122], heart and blood vessel muscle cells, and dental pulp resident stem cells[123] are capable of sensing mechanical strain, a result of either static or repetitive ECM deformation (stretch/compression). This biophysical factor has also been demonstrated to affect cell differentiation and reprogramming by regulating the epigenetic state.

One early study showed that elongated MSCs exhibited decreased HDAC activity, and HDAC activity was further decreased when a static compression or stretch was applied perpendicularly to the cells' long axis[124]. In contrast, in oligodendrocyte progenitor cells (OPC), biaxial static stretching resulted in an increase in the expression of HDAC11 and global deacetylation of H3K14ac, which is an active promoter state, thereby promoting oligodendrogenesis[125]. It requires further studies whether uniaxial and biaxial stretching produce different effects and if these responses are cell type-dependent. Additionally, it is shown that uniaxial static stretching can regulate histone phosphorylation. For instance, histone 3 phosphorylation (H3P) can loosen chromatin structure, thereby encouraging cell division and differentiation. It is reported that

static strain in the range of 10–33% elongation could induce H3P by activating the Piezo1 ion channel[126].

Cyclic stretching is also reported to be able to decrease the level of HDAC1 in bone marrow MSCs (BMSCs), influencing the histone acetylation of the JAG1 promoter and thereby inducing the differentiation of BMSCs into osteoblasts[127]. MicroRNAs are suggested capable of mediating the biaxial stretch-regulation of HDAC expression, as miR-365 induced by cyclic strain to suppress the HDAC4 gene expression in rat MSCs, facilitating chondrogenic differentiation[128, 129]. Compared to static stretch, biaxial cyclic stretching of human adipose-derived stem cells (hASC) caused a decrease in H3P and FABP4 expression level, and impaired adipogenic differentiation[130]. These divergent results from those of static stretching may be due to differences in stretch mode (static vs. cyclic), axial direction (uniaxial vs. biaxial), and strain magnitude, which requires further investigation. Furthermore, it has been reported that cyclic stretching can regulate the methylation of histones and DNA to promote cell differentiation. During osteogenic differentiation of both mouse BMSCs and human adipose tissue multipotential stromal cells (hAT-MSC), biaxial cyclic stretching reduced the expression of DNA methyltransferase 3b (DNMT3B) and enhanced DNA demethylation on CpG islands, thus promoting osteogenesis[131, 132]. Additionally, biaxial cyclic stretching of BMSCs decreased the expression of H3K9me3 and promoted BMSC differentiation into fibroblasts[133]. In epidermal progenitor cells (EPCs), biaxial cyclic stretching resulted in the enrichment of Emd, a mechanosensory complex consisting of emerin, located at the outer nuclear membrane. This caused a transition from a constant repression signal (H3K9me3) to a temporary repression signal (H3K27me3) at the constitutive heterochromatin. This shift directly influenced the precocious lineage commitment[134].

1.5.3 Morphological changes in physical confinement

In addition to mechanical stretching, changes on cell morphology caused by the physical confinement of 3D environment have been observed to induce epigenetic changes that significantly impact cell reprogramming. Studies have shown that reprogramming efficiency for both mouse and human iPSCs could be increased more than twofold in a 3D PEG-based hydrogel environment. This increase was attributed to the increase in mesenchymal-to-epithelial transition (MET), and acetylation and methylation of Histone 3 induced by the morphological change of cells[135]. Another study has also shown that the use of micropatterned substrates can confine the growth of fibroblasts laterally. This restriction induces epigenetic changes and enhances the reprogramming of cells into iPSC-like cells[136]. Despite the iPSC reprogramming, these topographical cues are shown to promote direct cell reprogramming. For example, research has shown that microgrooves can stimulate the translocation of the transcription factor MRTFA, and increase histone acetylation level, thereby increasing the generation of functional cardiomyocytes from mouse fibroblasts[137]. In another study, substrates with nanogrooves have been found to upregulate MET gene expression and H3K4me3 level, resulting in increased efficiency of converting mouse embryonic fibroblasts into induced dopaminergic neurons[138].

1.5.4 Shear stress

Recent research on the effects of shear stress stimulation has primarily focused on the endothelial cells (ECs) in blood vessels due to the significant role that hemodynamic forces play in maintaining and remodeling the vascular wall. Different types of shear stress have been proven to regulate histone modification and cell plasticity. For example, during the angiogenesis process, low shear stress (below 5 dyne/cm^2) enhances matrix metalloproteinase-14 (MMP14) expression via the phosphorylation of HDAC1 in ECs. It also triggers the expression of

thrombomodulin by enhancing the levels of H3K4me3 and H3K27ac, supporting the growth and migration of ECs for angiogenesis[139, 140]. Furthermore, steady shear flow can trigger CFL2/F-actin cytoskeletal reorganization, which will induce H2B acetylation and reinforce the primed state of cells in human embryonic stem cells (hESC)[141].

High shear stress (HSS) (larger than 10 dyne/cm^2), whether steady or pulsatile, has considerable effects on vascular remodeling[142]. Pulsatile shear stress (PS) is believed to maintain cell homeostasis and protect blood vessels from atherosclerosis. For example, PS increases the level of H3K27ac through KLF4, contributing to Ca^{2+}-dependent activation of endothelial nitric oxide synthase (eNOS) and EC homeostasis[143]. Also, HSS is able to regulate the expression of polycomb methyltransferase EZH2. Steady laminar shear stress at 20 dynes/cm^2 reduces EZH2 expression and H3K27me3 level, resulting in a decrease in endothelial inflammatory factors[144, 145]. Furthermore, HSS can also regulate DNA methylation to modulate cell phenotype. DNMT1 has been observed to control arterial vascular remodeling and arteriogenic capability. Increase in the expression of DNMT1, which is able to regulate arterial vascular remodeling and arteriogenic capability, and global DNA hypermethylation is observed in a femoral artery ligation model, when collateral arterial segments are exposed to elevated steady shear stress. This was accompanied by a decrease in proatherogenic monocyte adhesion dependent on DNMT1[146].

1.6 Microfluidics devices in cell engineering

The advent of microfluidics, technology of manipulating and controlling fluids, usually in the range from10^{-9} to 10^{-18} liters, using microchannels with dimensions from tens to hundreds of micrometers[147], has revolutionized the field of cell engineering. The key attractiveness of

microfluidics lies in its ability to offer precise control of cellular microenvironment, high throughput analysis, lower reagent consumption, faster reaction times, and integration of multiple functionalities. The birth of microfluidics can be traced back to the late 20th century, emerging from endeavors to miniaturize analytical systems, especially within the fields of chromatography and capillary electrophoresis. In 1990, Manz et al. proposed the concept of micro total analysis systems (μTAS), fundamentally shifting the landscape of analytical chemistry. This innovative concept proposed the integration of several laboratory functionalities into a single chip, thus catalyzing a considerable leap in the potential of analytical technologies[148]. Following the breakthrough of μTAS, another critical milestone in the history of microfluidics was the development of soft lithography. This novel technique, introduced by Whitesides and his team in 1998, revolutionized microfabrication by utilizing polydimethylsiloxane (PDMS), an optically transparent, gas- and vapour-permeable elastomer, to make microfluidic devices. Soft lithography made microfabrication processes simpler and more accessible, enabling more sophisticated design implementations in microfluidics and further expanding the range of potential applications[149].

1.6.1 Fabrication of microfluidics device

At the beginning, microfluidic devices were primarily fabricated by techniques in semiconductor industry, including photolithography, etching, and deposition, with the materials compatibale with these microfabrication techniques, such as silicon, quartz, and glass[150-154]. Anisotropic wet etching techniques using potassium hydroxide (KOH) and tetramethylammonium hydroxide (TMAH), and dry etching techniques such as reactive ion etching (RIE) and deep reactive ion etching (DRIE) are typically employed for the pattern of silicon. Conversely, isotropic wet etching through the application of hydrofluoric acid (HF) is normally used for the patterning of

quartz and glass. Despite their widespread use, these traditional microfabrication approaches have several limitations, including the high cost of substrate per unit area, long and expensive process time, requirement of clean room, limited channel profile, and undesirable physical properties of traditional materials. To overcome these limitations and expand the application of microfluidics devices, much attention has been placed on polymers due to their advantages over the traditional materials, such as lower unit area price, a wider range of available material properties, unique properties significant for cellular applications including optical transparency, electrical insulation and gas permeability, and potential for the mass production[155].

The fabrication of microfluidics devices utilizing machining techniques is usually expensive, attributable not only to the high capital costs of the necessary equipment but also the time-consuming nature of the fabrication process. However, this manufacturing cost can be substantially reduced through the implementation of a replication approach. With this strategy, the micro- or nanostructures are fabricated only once to create the master or mould with inverted or negative features of the intended device structure, from which the final microfluidics device can be subsequently replicated.

Recently, soft lithography is usually employed to fabricate microfluidics devices, starting with creation of a master mould through photolithography[155] (Fig. 1.6). This process involves spin coating a layer of negative SU-8 photoresist onto a substrate, followed by a soft bake with a temperature profile dependent on the thickness of SU-8 resist. Following the soft bake, a photomask is used to transfer the desired pattern onto the SU-8-coated substrate through UV light exposure. A post-exposure bake is then conducted to accelerate SU-8 polymerization. Subsequent development of the SU-8 yields the master mould with designed microfluidic structure. The fabrication process proceeds with PDMS casting onto the SU-8 master mould. The

first step is the preparation of PDMS, by mixing base elastomer and curing agent. This mixture is then poured onto the SU-8 moold. Curing of the PDMS is conducted either at room temperature or at an elevated temperature (typically ranging from 40 to 70 °C) to facilitate polymeric crosslinking. The elastomer is subsequently peeled off for demolding. Degassing of the mixture in a vacuum chamber during the mixing and molding steps is typically required to remove cavities or bubbles that could compromise the integrity of the molded structure. The PDMS layer with the microfluidic structures can be sealed by bonding to another substrate, which can be achieved using oxygen plasma[156] or corona discharge[157]. With the rapid development of 3D printing technology in recent years, this technology offers the potential to fabricate microfluidics devices with a lower cost compared to traditional microfabrication techniques requiring the use of clean room. 3D printing also makes it possible to use materials with different properties to fabricate parts and assemblies of the microfluidics device in a single process. Moreover, 3D printing offers a faster and easier way to develop prototypes from conceptual design through small volume production for early-stage functional testing[158-161].

1.6.2 Applications in cell engineering

Because of the extraordinary biocompatibility and physical properties of PDMS, microfluidics devices are widely used in cell engineering. It can be used for cell culture with unique advantages compared to traditional macroscopic culture in flasks, dishes and well-plates, including flexible device design, flexible and well-controlled experimental condition, lower requirement of cell number, ability of single cell handling, real-time and on-chip analysis, automation, direct coupling to downstream analysis system, ability to perform perfusion culture, controlled co-culture, and reduced consumption on reagents[162]. For example, researchers have developed a compartmentalized microfluidics device, which mimics the physiological

environment of migrating cells, and could be used to characterize cellular locomotion mechanisms and cell morphology in single-cell level during migration of brain tumor stem cells[163].

Multiple microfluidics designs have been developed for cell sorting either in active or passive ways, by employment of external fields (acoustic, electric, magnetic, and optical), or inertial forces, filters, and adhesion mechanisms, respectively[164]. Compared to traditional cell sorting methods, microfluidics systems have unique advantages including miniaturization of necessary equipment, elimination of potentially biohazardous aerosols, and simplification of the complex protocols of conventional cell sorting platforms. For example, researchers developed a microfluidics device for high throughput label-free cell sorting based on inertial focusing. Based on the size variation, the cells could be differentially focused and sorted under laminar flow using a serpentine pattern[165]. Another microfluidics system based on size exclusion filtration was developed to sort circulating fetal cells (CFCs) from maternal blood. This device consists of a series of linear arrays of pillars with decreasing spacing, which is able to group cells selectively based on the size and shape[166].

Also, the traditional methods used to measure the mechanical properties of cells, including micropipette aspiration, atomic force microscopy (AFM) and optical and magnetic tweezers[75], are limited to measure one single cell at a time. To improve the throughput of this measurement, multiple microfluidics systems have been developed including micro-constriction arrays[167-169], microchannel resonators[170], and deformability cytometry[171-173]. In deformability cytometry systems, the transit time of cells through constrictions[171] or the cell deformation under hydrodynamic stretching[172] are used to measure the mechanical property.

Microfluidics systems are also widely used in other biomedical applications, including DNA sequencing, tissue engineering, biomarker-screening for diseases, and point-of-care (POC) diagnostics etc. It provides a new platform to address the challenges in traditional biological and biomedical studies with innovative strategies, with the unique advantages of miniaturization, multiplexing and high throughput.

References

1. Waddington, C. and H. Kacser, *The strategy of the genes. A discussion of some aspects of theoretical biology. With an appendix by H.* Kacser. Strateg. genes. A Discuss. some Asp. Theor. Biol. With an Append. by H. Kacser, 1957.
2. Takahashi, K. and S. Yamanaka, *A decade of transcription factor-mediated reprogramming to pluripotency.* Nat Rev Mol Cell Biol, 2016. **17**(3): p. 183-93.
3. Spemann, H. and H. Mangold, *Induction of embryonic primordia by implantation of organizers from a different species. 1923.* Int J Dev Biol, 2001. **45**(1): p. 13-38.
4. Gurdon, J.B., T.R. Elsdale, and M. Fischberg, *Sexually mature individuals of Xenopus laevis from the transplantation of single somatic nuclei.* Nature, 1958. **182**(4627): p. 64-5.
5. Gurdon, J.B., *The developmental capacity of nuclei taken from intestinal epithelium cells of feeding tadpoles.* J Embryol Exp Morphol, 1962. **10**: p. 622-40.
6. Wilmut, I., et al., *Viable offspring derived from fetal and adult mammalian cells.* Nature, 1997. **385**(6619): p. 810-3.
7. Blau, H.M., C.P. Chiu, and C. Webster, *Cytoplasmic activation of human nuclear genes in stable heterocaryons.* Cell, 1983. **32**(4): p. 1171-80.
8. Tada, M., et al., *Nuclear reprogramming of somatic cells by in vitro hybridization with ES cells.* Curr Biol, 2001. **11**(19): p. 1553-8.
9. Cowan, C.A., et al., *Nuclear reprogramming of somatic cells after fusion with human embryonic stem cells.* Science, 2005. **309**(5739): p. 1369-73.
10. Davis, R.L., H. Weintraub, and A.B. Lassar, *Expression of a single transfected cDNA converts fibroblasts to myoblasts.* Cell, 1987. **51**(6): p. 987-1000.

11. Kulessa, H., J. Frampton, and T. Graf, *GATA-1 reprograms avian myelomonocytic cell lines into eosinophils, thromboblasts, and erythroblasts.* Genes Dev, 1995. **9**(10): p. 1250-62.

12. Xie, H., et al., *Stepwise reprogramming of B cells into macrophages.* Cell, 2004. **117**(5): p. 663-76.

13. Postlethwait, J.H. and H.A. Schneiderman, *A clonal analysis of determination in Antennapedia a homoeotic mutant of Drosophila melanogaster.* Proc Natl Acad Sci U S A, 1969. **64**(1): p. 176-83.

14. Schneuwly, S., R. Klemenz, and W.J. Gehring, *Redesigning the body plan of Drosophila by ectopic expression of the homoeotic gene Antennapedia.* Nature, 1987. **325**(6107): p. 816-8.

15. Frischer, L.E., F.S. Hagen, and R.L. Garber, *An inversion that disrupts the Antennapedia gene causes abnormal structure and localization of RNAs.* Cell, 1986. **47**(6): p. 1017-23.

16. Schneuwly, S., A. Kuroiwa, and W.J. Gehring, *Molecular analysis of the dominant homeotic Antennapedia phenotype.* EMBO J, 1987. **6**(1): p. 201-6.

17. Scott, M.P., et al., *The molecular organization of the Antennapedia locus of Drosophila.* Cell, 1983. **35**(3 Pt 2): p. 763-76.

18. Hazelrigg, T. and T.C. Kaufman, *Revertants of Dominant Mutations Associated with the Antennapedia Gene Complex of DROSOPHILA MELANOGASTER: Cytology and Genetics.* Genetics, 1983. **105**(3): p. 581-600.

19. Halder, G., P. Callaerts, and W.J. Gehring, *Induction of ectopic eyes by targeted expression of the eyeless gene in Drosophila.* Science, 1995. **267**(5205): p. 1788-92.

20. Takahashi, K. and S. Yamanaka, *Induction of pluripotent stem cells from mouse embryonic and adult fibroblast cultures by defined factors.* Cell, 2006. **126**(4): p. 663-76.

21. Takahashi, K., et al., *Induction of pluripotent stem cells from adult human fibroblasts by defined factors.* Cell, 2007. **131**(5): p. 861-72.

22. Yu, J., et al., *Induced pluripotent stem cell lines derived from human somatic cells.* Science, 2007. **318**(5858): p. 1917-20.

23. Vierbuchen, T., et al., *Direct conversion of fibroblasts to functional neurons by defined factors.* Nature, 2010. **463**(7284): p. 1035-41.

24. Ieda, M., et al., *Direct Reprogramming of Fibroblasts into Functional Cardiomyocytes by Defined Factors.* Cell, 2010. **142**(3): p. 375-386.

25. Huang, P., et al., *Induction of functional hepatocyte-like cells from mouse fibroblasts by defined factors.* Nature, 2011. **475**(7356): p. 386-9.

26. Srivastava, D. and N. DeWitt, *In Vivo Cellular Reprogramming: The Next Generation.* Cell, 2016. **166**(6): p. 1386-1396.

27. Wang, H., et al., *Direct cell reprogramming: approaches, mechanisms and progress.* Nat Rev Mol Cell Biol, 2021. **22**(6): p. 410-424.

28. Jorstad, N.L., et al., *Stimulation of functional neuronal regeneration from Muller glia in adult mice.* Nature, 2017. **548**(7665): p. 103-107.

29. Li, H. and G. Chen, *In Vivo Reprogramming for CNS Repair: Regenerating Neurons from Endogenous Glial Cells.* Neuron, 2016. **91**(4): p. 728-738.

30. Qian, L., et al., *In vivo reprogramming of murine cardiac fibroblasts into induced cardiomyocytes.* Nature, 2012. **485**(7400): p. 593-+.

31. Cahan, P., et al., *CellNet: network biology applied to stem cell engineering.* Cell, 2014. **158**(4): p. 903-915.

32. Stone, N.R., et al., *Context-Specific Transcription Factor Functions Regulate Epigenomic and Transcriptional Dynamics during Cardiac Reprogramming.* Cell Stem Cell, 2019. **25**(1): p. 87-102 e9.

33. Iwafuchi-Doi, M. and K.S. Zaret, *Pioneer transcription factors in cell reprogramming.* Genes Dev, 2014. **28**(24): p. 2679-92.

34. Zaret, K.S. and J.S. Carroll, *Pioneer transcription factors: establishing competence for gene expression.* Genes Dev, 2011. **25**(21): p. 2227-41.

35. Soufi, A., G. Donahue, and K.S. Zaret, *Facilitators and impediments of the pluripotency reprogramming factors' initial engagement with the genome.* Cell, 2012. **151**(5): p. 994-1004.

36. Cirillo, L.A., et al., *Opening of compacted chromatin by early developmental transcription factors HNF3 (FoxA) and GATA-4.* Mol Cell, 2002. **9**(2): p. 279-89.

37. Wapinski, O.L., et al., *Hierarchical mechanisms for direct reprogramming of fibroblasts to neurons.* Cell, 2013. **155**(3): p. 621-35.

38. Chanda, S., et al., *Generation of induced neuronal cells by the single reprogramming factor ASCL1.* Stem Cell Reports, 2014. **3**(2): p. 282-96.

39. Hashimoto, H., et al., *Cardiac Reprogramming Factors Synergistically Activate Genome-wide Cardiogenic Stage-Specific Enhancers.* Cell Stem Cell, 2019. **25**(1): p. 69-86 e5.

40. Zhou, H.Y., et al., *Akt1/protein kinase B enhances transcriptional reprogramming of fibroblasts to functional cardiomyocytes.* Proceedings of the National Academy of Sciences of the United States of America, 2015. **112**(38): p. 11864-11869.

41. Treutlein, B., et al., *Dissecting direct reprogramming from fibroblast to neuron using single-cell RNA-seq.* Nature, 2016. **534**(7607): p. 391-5.

42. Liu, Z.Q., et al., *Single-cell transcriptomics reconstructs fate conversion from fibroblast to cardiomyocyte.* Nature, 2017. **551**(7678): p. 100-+.

43. Wang, L., et al., *Improved Generation of Induced Cardiomyocytes Using a Polycistronic Construct Expressing Optimal Ratio of Gata4, Mef2c and Tbx5.* Jove-Journal of Visualized Experiments, 2015(105).

44. Wang, L., et al., *Stoichiometry of Gata4, Mef2c, and Tbx5 Influences the Efficiency and Quality of Induced Cardiac Myocyte Reprogramming.* Circulation Research, 2015. **116**(2): p. 237-U82.

45. Mathison, M., et al., *"Triplet" polycistronic vectors encoding Gata4, Mef2c, and Tbx5 enhances postinfarct ventricular functional improvement compared with singlet vectors.* J Thorac Cardiovasc Surg, 2014. **148**(4): p. 1656-1664 e2.

46. Ohi, Y., et al., *Incomplete DNA methylation underlies a transcriptional memory of somatic cells in human iPS cells.* Nat Cell Biol, 2011. **13**(5): p. 541-9.

47. Bar-Nur, O., et al., *Epigenetic memory and preferential lineage-specific differentiation in induced pluripotent stem cells derived from human pancreatic islet beta cells.* Cell Stem Cell, 2011. **9**(1): p. 17-23.

48. Wapinski, O.L., et al., *Rapid Chromatin Switch in the Direct Reprogramming of Fibroblasts to Neurons.* Cell Reports, 2017. **20**(13): p. 3236-3247.

49. Soufi, A., et al., *Pioneer Transcription Factors Target Partial DNA Motifs on Nucleosomes to Initiate Reprogramming.* Cell, 2015. **161**(3): p. 555-568.

50. Bannister, A.J. and T. Kouzarides, *Regulation of chromatin by histone modifications.* Cell Research, 2011. **21**(3): p. 381-395.

51. Liu, Z.Q., et al., *Re-patterning of H3K27me3, H3K4me3 and DNA methylation during fibroblast conversion into induced cardiomyocytes.* Stem Cell Research, 2016. **16**(2): p. 507-518.

52. Kim, J., et al., *Direct reprogramming of mouse fibroblasts to neural progenitors.* Proceedings of the National Academy of Sciences of the United States of America, 2011. **108**(19): p. 7838-7843.

53. Barbagiovanni, G., et al., *KMT2B Is Selectively Required for Neuronal Transdifferentiation, and Its Loss Exposes Dystonia Candidate Genes.* Cell Reports, 2018. **25**(4): p. 988-1001.

54. Benayoun, B.A., et al., *H3K4me3 Breadth Is Linked to Cell Identity and Transcriptional Consistency.* Cell, 2014. **158**(3): p. 673-688.

55. Ezhkova, E., et al., *EZH1 and EZH2 cogovern histone H3K27 trimethylation and are essential for hair follicle homeostasis and wound repair.* Genes Dev, 2011. **25**(5): p. 485-98.

56. Dal-Pra, S., et al., *Demethylation of H3K27 Is Essential for the Induction of Direct Cardiac Reprogramming by miR Combo.* Circulation Research, 2017. **120**(9): p. 1403-+.

57. Huang, P.Y., et al., *Direct Reprogramming of Human Fibroblasts to Functional and Expandable Hepatocytes.* Cell Stem Cell, 2014. **14**(3): p. 370-384.

58. Becker, J.S., et al., *Genomic and Proteomic Resolution of Heterochromatin and Its Restriction of Alternate Fate Genes.* Mol Cell, 2017. **68**(6): p. 1023-1037 e15.

59. Hirai, H. and N. Kikyo, *Inhibitors of suppressive histone modification promote direct reprogramming of fibroblasts to cardiomyocyte-like cells.* Cardiovasc Res, 2014. **102**(1): p. 188-90.

60. Cao, J. and Q. Yan, *Histone ubiquitination and deubiquitination in transcription DNA damage response, and cancer.* Frontiers in Oncology, 2012. **2**.

61. Zhou, Y., et al., *Bmi1 Is a Key Epigenetic Barrier to Direct Cardiac Reprogramming.* Cell Stem Cell, 2016. **18**(3): p. 382-395.

62. Vastenhouw, N.L. and A.F. Schier, *Bivalent histone modifications in early embryogenesis.* Current Opinion in Cell Biology, 2012. **24**(3): p. 374-386.

63. Bernstein, B.E., et al., *A bivalent chromatin structure marks key developmental genes in embryonic stem cells.* Cell, 2006. **125**(2): p. 315-326.

64. Bramswig, N.C., et al., *Epigenomic plasticity enables human pancreatic alpha to beta cell reprogramming.* J Clin Invest, 2013. **123**(3): p. 1275-84.

65. Luo, C., et al., *Global DNA methylation remodeling during direct reprogramming of fibroblasts to neurons.* Elife, 2019. **8**.

66. Li, W., et al., *Long-term persistence and development of induced pancreatic beta cells generated by lineage conversion of acinar cells.* Nat Biotechnol, 2014. **32**(12): p. 1223-30.

67. Vining, K.H. and D.J. Mooney, *Mechanical forces direct stem cell behaviour in development and regeneration.* Nat Rev Mol Cell Biol, 2017. **18**(12): p. 728-742.

68. DuFort, C.C., M.J. Paszek, and V.M. Weaver, *Balancing forces: architectural control of mechanotransduction.* Nat Rev Mol Cell Biol, 2011. **12**(5): p. 308-19.

69. Jaalouk, D.E. and J. Lammerding, *Mechanotransduction gone awry.* Nat Rev Mol Cell Biol, 2009. **10**(1): p. 63-73.

70. Martino, F., et al., *Cellular Mechanotransduction: From Tension to Function.* Frontiers in Physiology, 2018. **9**.

71. Uhler, C. and G.V. Shivashankar, *Regulation of genome organization and gene expression by nuclear mechanotransduction.* Nat Rev Mol Cell Biol, 2017. **18**(12): p. 717-727.

72. Kirby, T.J. and J. Lammerding, *Emerging views of the nucleus as a cellular mechanosensor.* Nature Cell Biology, 2018. **20**(4): p. 373-381.

73. Charras, G. and A.S. Yap, *Tensile Forces and Mechanotransduction at Cell-Cell Junctions.* Current Biology, 2018. **28**(8): p. R445-R457.

74. Ranade, S.S., R. Syeda, and A. Patapoutian, *Mechanically Activated Ion Channels (vol 87, pg 1162, 2015).* Neuron, 2015. **88**(2): p. 433-433.

75. Song, Y., et al., *Cell engineering: Biophysical regulation of the nucleus.* Biomaterials, 2020. **234**: p. 119743.

76. Wang, N., J.P. Butler, and D.E. Ingber, *Mechanotransduction across the cell surface and through the cytoskeleton.* Science, 1993. **260**(5111): p. 1124-7.

77. Geiger, B., et al., *Transmembrane crosstalk between the extracellular matrix--cytoskeleton crosstalk.* Nat Rev Mol Cell Biol, 2001. **2**(11): p. 793-805.

78. Chrzanowska-Wodnicka, M. and K. Burridge, *Rho-stimulated contractility drives the formation of stress fibers and focal adhesions.* J Cell Biol, 1996. **133**(6): p. 1403-15.

79. Pelham, R.J., Jr. and Y. Wang, *Cell locomotion and focal adhesions are regulated by substrate flexibility.* Proc Natl Acad Sci U S A, 1997. **94**(25): p. 13661-5.

80. Stutchbury, B., et al., *Distinct focal adhesion protein modules control different aspects of mechanotransduction.* J Cell Sci, 2017. **130**(9): p. 1612-1624.

81. Ohashi, K., S. Fujiwara, and K. Mizuno, *Roles of the cytoskeleton, cell adhesion and rho signalling in mechanosensing and mechanotransduction.* J Biochem, 2017. **161**(3): p. 245-254.

82. Wang, N., J.D. Tytell, and D.E. Ingber, *Mechanotransduction at a distance: mechanically coupling the extracellular matrix with the nucleus.* Nature reviews Molecular cell biology, 2009. **10**(1): p. 75-82.

83. Dahl, K.N., A.J. Ribeiro, and J. Lammerding, *Nuclear shape, mechanics, and mechanotransduction.* Circ Res, 2008. **102**(11): p. 1307-18.

84. Soheilypour, M., et al., *On the nuclear pore complex and its roles in nucleo-cytoskeletal coupling and mechanobiology.* Cellular and Molecular Bioengineering, 2016. **9**: p. 217-226.

85. Wilson, K.L. and J.M. Berk, *The nuclear envelope at a glance.* Journal of Cell Science, 2010. **123**(12): p. 1973-1978.

86. Barton, L.J., A.A. Soshnev, and P.K. Geyer, *Networking in the nucleus: a spotlight on LEM-domain proteins.* Curr Opin Cell Biol, 2015. **34**: p. 1-8.

87. de Leeuw, R., Y. Gruenbaum, and O. Medalia, *Nuclear Lamins: Thin Filaments with Major Functions.* Trends Cell Biol, 2018. **28**(1): p. 34-45.

88. Bickmore, W.A. and B. van Steensel, *Genome architecture: domain organization of interphase chromosomes.* Cell, 2013. **152**(6): p. 1270-84.

89. Solovei, I., et al., *LBR and lamin A/C sequentially tether peripheral heterochromatin and inversely regulate differentiation.* Cell, 2013. **152**(3): p. 584-98.

90. Mejat, A. and T. Misteli, *LINC complexes in health and disease.* Nucleus, 2010. **1**(1): p. 40-52.

91. Horn, H.F., *LINC complex proteins in development and disease.* Curr Top Dev Biol, 2014. **109**: p. 287-321.

92. Chang, W., H.J. Worman, and G.G. Gundersen, *Accessorizing and anchoring the LINC complex for multifunctionality.* J Cell Biol, 2015. **208**(1): p. 11-22.

93. Gundersen, G.G. and H.J. Worman, *Nuclear positioning.* Cell, 2013. **152**(6): p. 1376-89.

94. Szczesny, S.E. and R.L. Mauck, *The Nuclear Option: Evidence Implicating the Cell Nucleus in Mechanotransduction.* J Biomech Eng, 2017. **139**(2): p. 0210061-02100616.

95. Uhler, C. and G.V. Shivashankar, *Nuclear Mechanopathology and Cancer Diagnosis.* Trends Cancer, 2018. **4**(4): p. 320-331.

96. Miroshnikova, Y.A., M.M. Nava, and S.A. Wickstrom, *Emerging roles of mechanical forces in chromatin regulation.* Journal of Cell Science, 2017. **130**(14): p. 2243-2250.

97. Sun, J., et al., *Force-induced gene up-regulation does not follow the weak power law but depends on H3K9 demethylation.* Science Advances, 2020. **6**(14): p. eaay9095.

98. Uhler, C. and G.V. Shivashankar, *Chromosome Intermingling: Mechanical Hotspots for Genome Regulation.* Trends in Cell Biology, 2017. **27**(11): p. 820-829.

99. Allshire, R.C. and H.D. Madhani, *Ten principles of heterochromatin formation and function.* Nat Rev Mol Cell Biol, 2018. **19**(4): p. 229-244.

100. Janssen, A., S.U. Colmenares, and G.H. Karpen, *Heterochromatin: Guardian of the Genome.* Annu Rev Cell Dev Biol, 2018. **34**: p. 265-288.

101. Narita, T., B.T. Weinert, and C. Choudhary, *Functions and mechanisms of non-histone protein acetylation.* Nat Rev Mol Cell Biol, 2019. **20**(3): p. 156-174.

102. Wu, X. and Y. Zhang, *TET-mediated active DNA demethylation: mechanism, function and beyond.* Nat Rev Genet, 2017. **18**(9): p. 517-534.

103. Martire, S., et al., *Phosphorylation of histone H3.3 at serine 31 promotes p300 activity and enhancer acetylation.* Nature Genetics, 2019. **51**(6): p. 941-+.

104. Liszczak, G., et al., *Acetylation blocks DNA damage-induced chromatin ADP-ribosylation.* Nat Chem Biol, 2018. **14**(9): p. 837-840.

105. Ryu, H.Y., et al., *The Ulp2 SUMO protease promotes transcription elongation through regulation of histone sumoylation.* Embo Journal, 2019. **38**(16).

106. Worden, E.J., et al., *Mechanism of Cross-talk between H2B Ubiquitination and H3 Methylation by Dot1L.* Cell, 2019. **176**(6): p. 1490-1501 e12.

107. Schubeler, D., *Function and information content of DNA methylation.* Nature, 2015. **517**(7534): p. 321-6.

108. Gkretsi, V. and T. Stylianopoulos, *Cell Adhesion and Matrix Stiffness: Coordinating Cancer Cell Invasion and Metastasis.* Front Oncol, 2018. **8**: p. 145.

109. He, X.T., et al., *Macrophage involvement affects matrix stiffness-related influences on cell osteogenesis under three-dimensional culture conditions.* Acta Biomaterialia, 2018. **71**: p. 132-147.

110. Engler, A.J., et al., *Matrix elasticity directs stem cell lineage specification.* Cell, 2006. **126**(4): p. 677-89.

111. Cozzolino, A.M., et al., *Modulating the Substrate Stiffness to Manipulate Differentiation of Resident Liver Stem Cells and to Improve the Differentiation State of Hepatocytes.* Stem Cells Int, 2016. **2016**: p. 5481493.

112. Gerardo, H., et al., *Soft culture substrates favor stem-like cellular phenotype and facilitate reprogramming of human mesenchymal stem/stromal cells (hMSCs) through mechanotransduction.* Scientific Reports, 2019. **9**.

113. Higuchi, S., et al., *Culturing of mouse and human cells on soft substrates promote the expression of stem cell markers.* J Biosci Bioeng, 2014. **117**(6): p. 749-55.

114. Pennarossa, G., et al., *Epigenetic Erasing and Pancreatic Differentiation of Dermal Fibroblasts into Insulin-Producing Cells are Boosted by the Use of Low-Stiffness Substrate.* Stem Cell Reviews and Reports, 2018. **14**(3): p. 398-411.

115. Dou, C.W., et al., *P300 Acetyltransferase Mediates Stiffness-Induced Activation of Hepatic Stellate Cells Into Tumor-Promoting Myofibroblasts.* Gastroenterology, 2018. **154**(8): p. 2209-+.

116. Killaars, A.R., et al., *Extended Exposure to Stiff Microenvironments Leads to Persistent Chromatin Remodeling in Human Mesenchymal Stem Cells.* Adv Sci (Weinh), 2019. **6**(3): p. 1801483.

117. Qu, J., et al., *Reversing Mechanoinductive DSP Expression by CRISPR/dCas9-mediated Epigenome Editing.* Am J Respir Crit Care Med, 2018. **198**(5): p. 599-609.

118. Ligresti, G., et al., *CBX5/G9a/H3K9me-mediated gene repression is essential to fibroblast activation during lung fibrosis.* Jci Insight, 2019. **4**(12).

119. Przybyla, L., J.N. Lakins, and V.M. Weaver, *Tissue Mechanics Orchestrate Wnt-Dependent Human Embryonic Stem Cell Differentiation.* Cell Stem Cell, 2016. **19**(4): p. 462-475.

120. Li, Y., C.B. Tang, and K.A. Kilian, *Matrix Mechanics Influence Fibroblast-Myofibroblast Transition by Directing the Localization of Histone Deacetylase 4.* Cell Mol Bioeng, 2017. **10**(5): p. 405-415.

121. Gracey, E., et al., *Tendon and ligament mechanical loading in the pathogenesis of inflammatory arthritis.* Nat Rev Rheumatol, 2020. **16**(4): p. 193-207.

122. Nonomura, K., et al., *Piezo2 senses airway stretch and mediates lung inflation-induced apnoea.* Nature, 2017. **541**(7636): p. 176-181.

123. Marrelli, M., et al., *Dental Pulp Stem Cell Mechanoresponsiveness: Effects of Mechanical Stimuli on Dental Pulp Stem Cell Behavior.* Front Physiol, 2018. **9**: p. 1685.

124. Li, Y., et al., *Biophysical regulation of histone acetylation in mesenchymal stem cells.* Biophys J, 2011. **100**(8): p. 1902-9.

125. Jagielska, A., et al., *Mechanical Strain Promotes Oligodendrocyte Differentiation by Global Changes of Gene Expression.* Frontiers in Cellular Neuroscience, 2017. **11**.

126. Gudipaty, S.A., et al., *Mechanical stretch triggers rapid epithelial cell division through Piezo1.* Nature, 2017. **543**(7643): p. 118-+.

127. Wang, J., et al., *Mechanical stimulation orchestrates the osteogenic differentiation of human bone marrow stromal cells by regulating HDAC1.* Cell Death Dis, 2016. **7**(5): p. e2221.

128. Guan, Y.J., et al., *MiR-365: a mechanosensitive microRNA stimulates chondrocyte differentiation through targeting histone deacetylase 4.* Faseb Journal, 2011. **25**(12): p. 4457-4466.

129. Zheng, Q., et al., *MicroRNA-365 functions as a mechanosensitive microRNA to inhibit end plate chondrocyte degeneration by targeting histone deacetylase 4.* Bone, 2019. **128**.

130. Paul, N.E., et al., *The effect of mechanical stress on the proliferation, adipogenic differentiation and gene expression of human adipose-derived stem cells.* J Tissue Eng Regen Med, 2018. **12**(1): p. 276-284.

131. Wang, C.D., et al., *Mechanical stimulation promote the osteogenic differentiation of bone marrow stromal cells through epigenetic regulation of Sonic Hedgehog.* Experimental Cell Research, 2017. **352**(2): p. 346-356.

132. Vlaikou, A.M., et al., *Mechanical stress affects methylation pattern of GNAS isoforms and osteogenic differentiation of hAT-MSCs.* Biochim Biophys Acta Mol Cell Res, 2017. **1864**(8): p. 1371-1381.

133. Zhao, B., et al., *Mechanical stretching promotes the differentiation of BMSC into pelvic floor ligament fibroblasts.* Oncotarget, 2018. **5**.

134. Le, H.Q., et al., *Mechanical regulation of transcription controls Polycomb-mediated gene silencing during lineage commitment.* Nat Cell Biol, 2016. **18**(8): p. 864-75.

135. Caiazzo, M., et al., *Defined three-dimensional microenvironments boost induction of pluripotency.* Nat Mater, 2016. **15**(3): p. 344-52.

136. Roy, B., et al., *Laterally confined growth of cells induces nuclear reprogramming in the absence of exogenous biochemical factors.* Proc Natl Acad Sci U S A, 2018. **115**(21): p. E4741-E4750.

137. Sia, J.R., et al., *Effect of biophysical cues on reprogramming to cardiomyocytes.* Biomaterials, 2016. **103**: p. 1-11.

138. Yoo, J., et al., *Nanogrooved substrate promotes direct lineage reprogramming of fibroblasts to functional induced dopaminergic neurons.* Biomaterials, 2015. **45**: p. 36-45.

139. Bazou, D., et al., *Flow-induced HDAC1 phosphorylation and nuclear export in angiogenic sprouting.* Sci Rep, 2016. **6**: p. 34046.

140. Peghaire, C., et al., *The transcription factor ERG regulates a low shear stress-induced anti-thrombotic pathway in the microvasculature.* Nat Commun, 2019. **10**(1): p. 5014.

141. Wang, J.W., et al., *Flow-enhanced priming of hESCs through H2B acetylation and chromatin decondensation.* Stem Cell Research & Therapy, 2019. **10**(1).

142. Chiu, J.J. and S. Chien, *Effects of disturbed flow on vascular endothelium: pathophysiological basis and clinical perspectives.* Physiol Rev, 2011. **91**(1): p. 327-87.

143. He, M., et al., *Atheroprotective Flow Upregulates ITPR3 (Inositol 1,4,5-Trisphosphate Receptor 3) in Vascular Endothelium via KLF4 (Kruppel-Like Factor 4)-Mediated Histone Modifications.* Arterioscler Thromb Vasc Biol, 2019. **39**(5): p. 902-914.

144. Maleszewska, M., et al., *The decrease in histone methyltransferase EZH2 in response to fluid shear stress alters endothelial gene expression and promotes quiescence.* Angiogenesis, 2016. **19**(1): p. 9-24.

145. Xu, S., et al., *Flow-dependent epigenetic regulation of IGFBP5 expression by H3K27me3 contributes to endothelial anti-inflammatory effects.* Theranostics, 2018. **8**(11): p. 3007-3021.

146. Heuslein, J.L., et al., *DNA Methyltransferase 1-Dependent DNA Hypermethylation Constrains Arteriogenesis by Augmenting Shear Stress Set Point.* J Am Heart Assoc, 2017. **6**(12).

147. Whitesides, G.M., *The origins and the future of microfluidics.* Nature, 2006. **442**(7101): p. 368-73.

148. Manz, A., N. Graber, and H.M. Widmer, *Miniaturized Total Chemical-Analysis Systems - a Novel Concept for Chemical Sensing.* Sensors and Actuators B-Chemical, 1990. **1**(1-6): p. 244-248.

149. Whitesides, G.M., et al., *Soft lithography in biology and biochemistry.* Annual Review of Biomedical Engineering, 2001. **3**: p. 335-373.

150. Harrison, D.J., et al., *Micromachining a miniaturized capillary electrophoresis-based chemical analysis system on a chip.* Science, 1993. **261**(5123): p. 895-7.

151. Jacobson, S.C., et al., *Open-Channel Electrochromatography on a Microchip.* Analytical Chemistry, 1994. **66**(14): p. 2369-2373.

152. Jacobson, S.C., A.W. Moore, and J.M. Ramsey, *Fused Quartz Substrates for Microchip Electrophoresis.* Analytical Chemistry, 1995. **67**(13): p. 2059-2063.

153. Matzke, C.M., et al. *Microfabricated silicon gas chromatographic microchannels: fabrication and performance*. in *Micromachining and Microfabrication Process Technology IV*. 1998. SPIE.

154. Moore, A.W., S.C. Jacobson, and J.M. Ramsey, *Microchip separations of neutral species via micellar electrokinetic capillary chromatography.* Analytical Chemistry, 1995. **67**(22): p. 4184-4189.

155. Scott, S.M. and Z. Ali, *Fabrication Methods for Microfluidic Devices: An Overview.* Micromachines (Basel), 2021. **12**(3).

156. Bhattacharya, S., et al., *Studies on surface wettability of poly(dimethyl) siloxane (PDMS) and glass under oxygen-plasma treatment and correlation with bond strength.* Journal of Microelectromechanical Systems, 2005. **14**(3): p. 590-597.

157. Haubert, K., T. Drier, and D. Beebe, *PDMS bonding by means of a portable, low-cost corona system.* Lab Chip, 2006. **6**(12): p. 1548-9.

158. Nielsen, A.V., et al., *3D Printed Microfluidics.* Annu Rev Anal Chem (Palo Alto Calif), 2020. **13**(1): p. 45-65.

159. Bhattacharjee, N., et al., *The upcoming 3D-printing revolution in microfluidics.* Lab Chip, 2016. **16**(10): p. 1720-42.

160. Tasoglu, S. and A. Folch, *3D printed microfluidic devices*. 2019: MDPI.

161. Au, A.K., W. Lee, and A. Folch, *Mail-order microfluidics: evaluation of stereolithography for the production of microfluidic devices.* Lab Chip, 2014. **14**(7): p. 1294-301.

162. Halldorsson, S., et al., *Advantages and challenges of microfluidic cell culture in polydimethylsiloxane devices.* Biosensors & Bioelectronics, 2015. **63**: p. 218-231.

163. Huang, Y., et al., *Evaluation of cancer stem cell migration using compartmentalizing microfluidic devices and live cell imaging.* J Vis Exp, 2011(58): p. e3297.

164. Shields, C.W.t., C.D. Reyes, and G.P. Lopez, *Microfluidic cell sorting: a review of the advances in the separation of cells from debulking to rare cell isolation.* Lab Chip, 2015. **15**(5): p. 1230-49.

165. Di Carlo, D., et al., *Continuous inertial focusing, ordering, and separation of particles in microchannels.* Proc Natl Acad Sci U S A, 2007. **104**(48): p. 18892-7.

166. Mohamed, H., J.N. Turner, and M. Caggana, *Biochip for separating fetal cells from maternal circulation.* J Chromatogr A, 2007. **1162**(2): p. 187-92.

167. Rosenbluth, M.J., W.A. Lam, and D.A. Fletcher, *Analyzing cell mechanics in hematologic diseases with microfluidic biophysical flow cytometry.* Lab Chip, 2008. **8**(7): p. 1062-70.

168. Lange, J.R., et al., *Microconstriction arrays for high-throughput quantitative measurements of cell mechanical properties.* Biophys J, 2015. **109**(1): p. 26-34.

169. Lange, J.R., W.H. Goldmann, and J.L. Alonso, *Influence of alphavbeta3 integrin on the mechanical properties and the morphology of M21 and K562 cells.* Biochem Biophys Res Commun, 2016. **478**(3): p. 1280-5.

170. Byun, S., et al., *Characterizing deformability and surface friction of cancer cells.* Proc Natl Acad Sci U S A, 2013. **110**(19): p. 7580-5.

171. Nyberg, K.D., et al., *Quantitative Deformability Cytometry: Rapid, Calibrated Measurements of Cell Mechanical Properties.* Biophys J, 2017. **113**(7): p. 1574-1584.

172. Gossett, D.R., et al., *Hydrodynamic stretching of single cells for large population mechanical phenotyping.* Proc Natl Acad Sci U S A, 2012. **109**(20): p. 7630-5.

173. Dudani, J.S., et al., *Pinched-flow hydrodynamic stretching of single-cells.* Lab Chip, 2013. **13**(18): p. 3728-34.

Figures

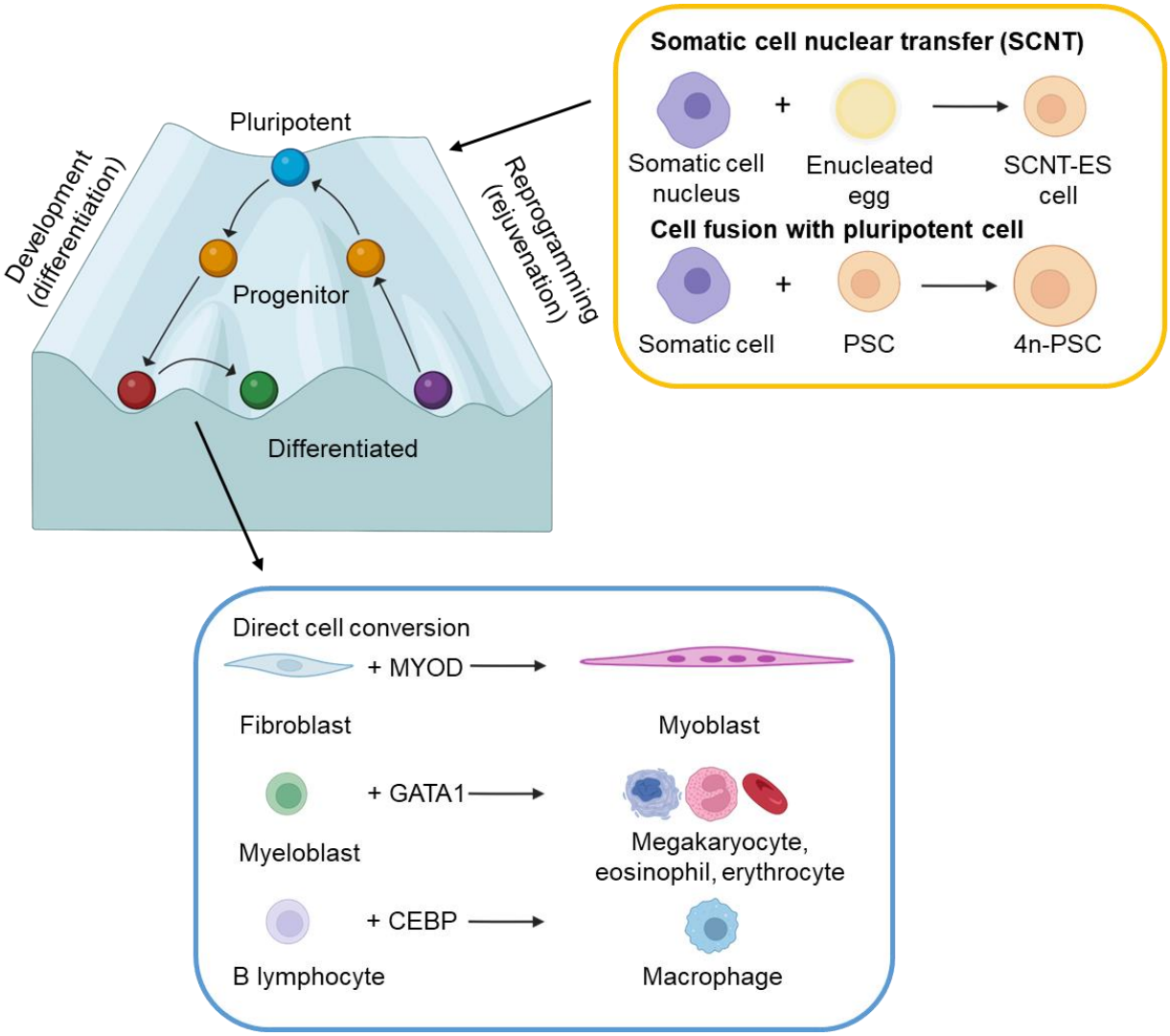

Fig. 1.1. Early studies on cell differentiation and reprogramming. Waddington's landscape demonstrating cell development and reprogramming process[2].

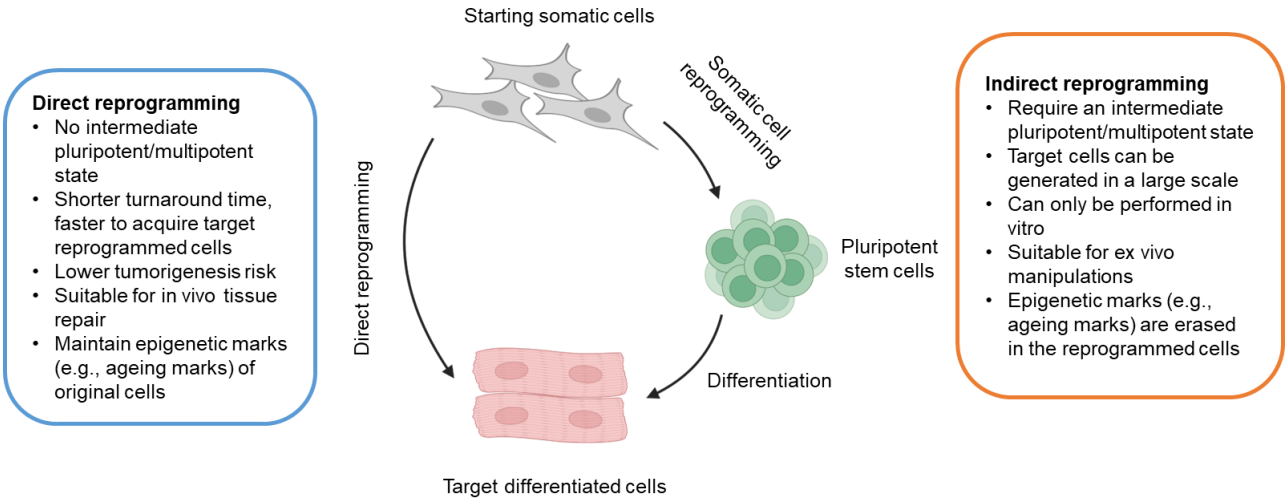

Fig. 1.2. Principles of indirect and direct reprogramming. Direct reprogramming changes cell fate without involving a pluripotent intermediate state[27].

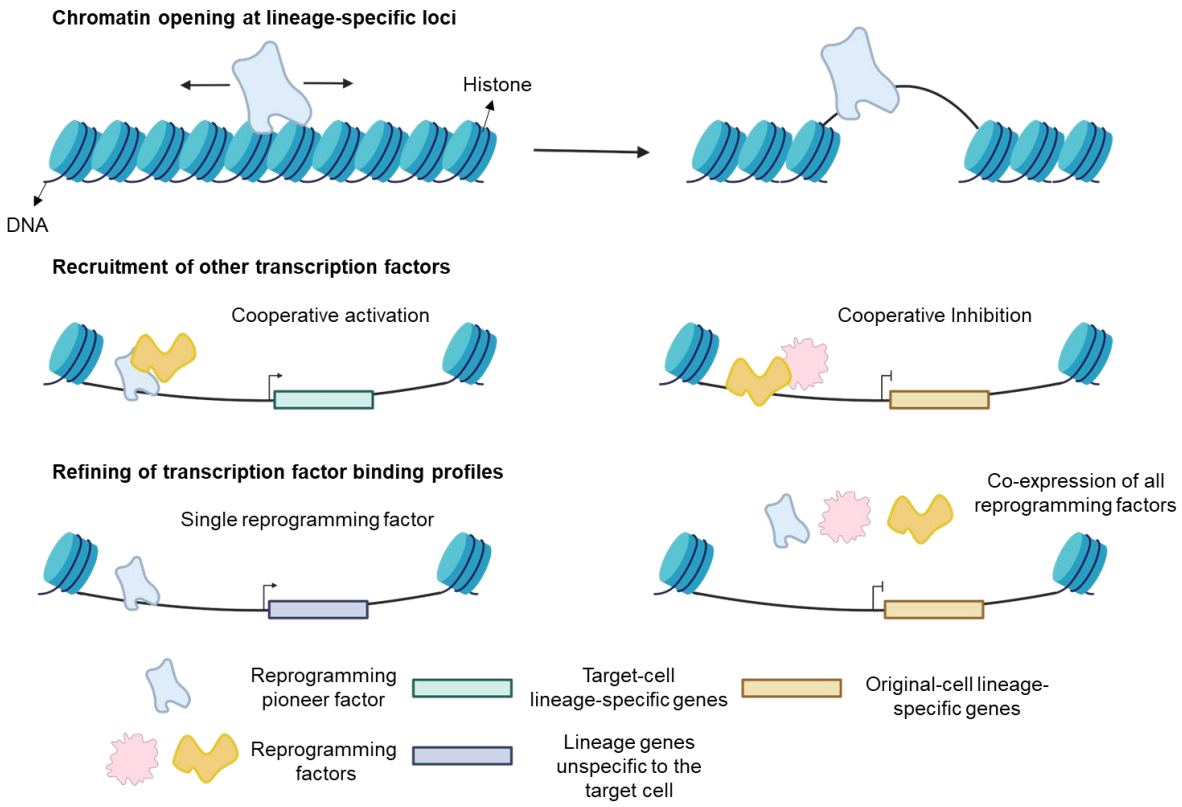

Fig. 1.3. Functions of reprogramming factors in cell reprogramming. Pioneer factors can access closed chromatin at the initial stages of cell reprogramming. Reprogramming factors work cooperatively to activate or inhibit gene expression. Reprogramming factors are able to refine the binding profile of other reprogramming factors[27].

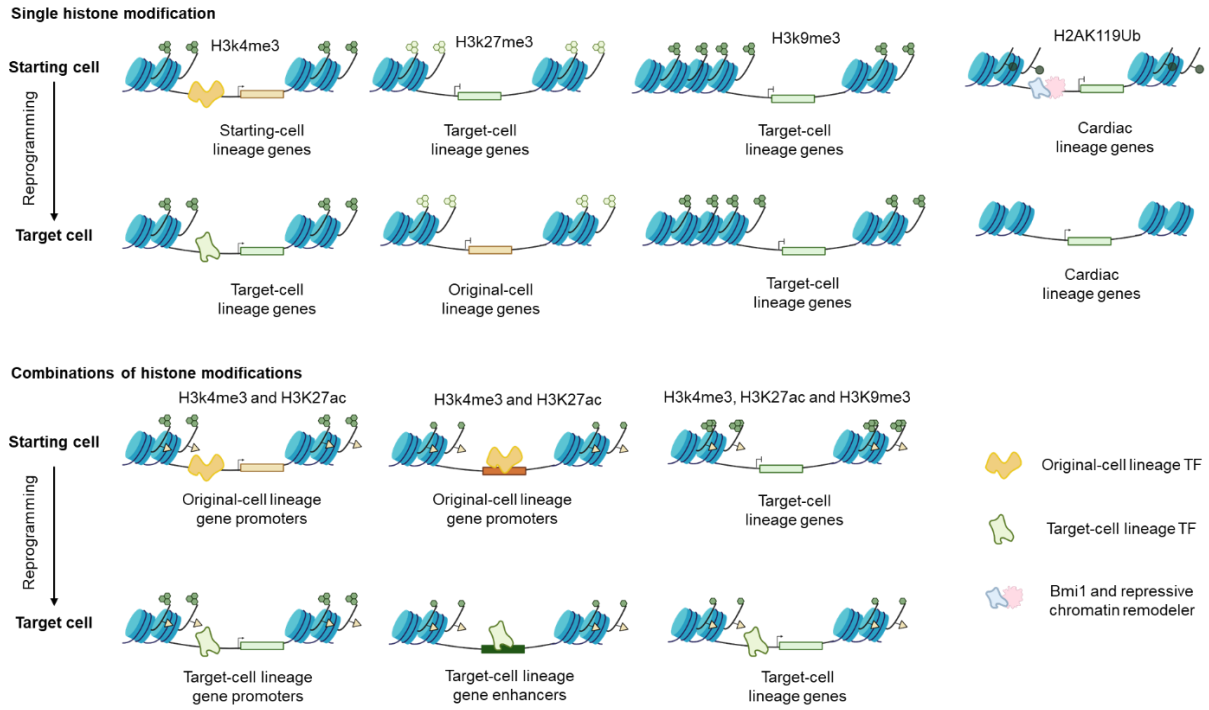

Fig. 1.4. Epigenetics modifications regulating gene expression during cell reprogramming. Different types and combinations of histone modifications have different effects on epigenetic regulation[27].

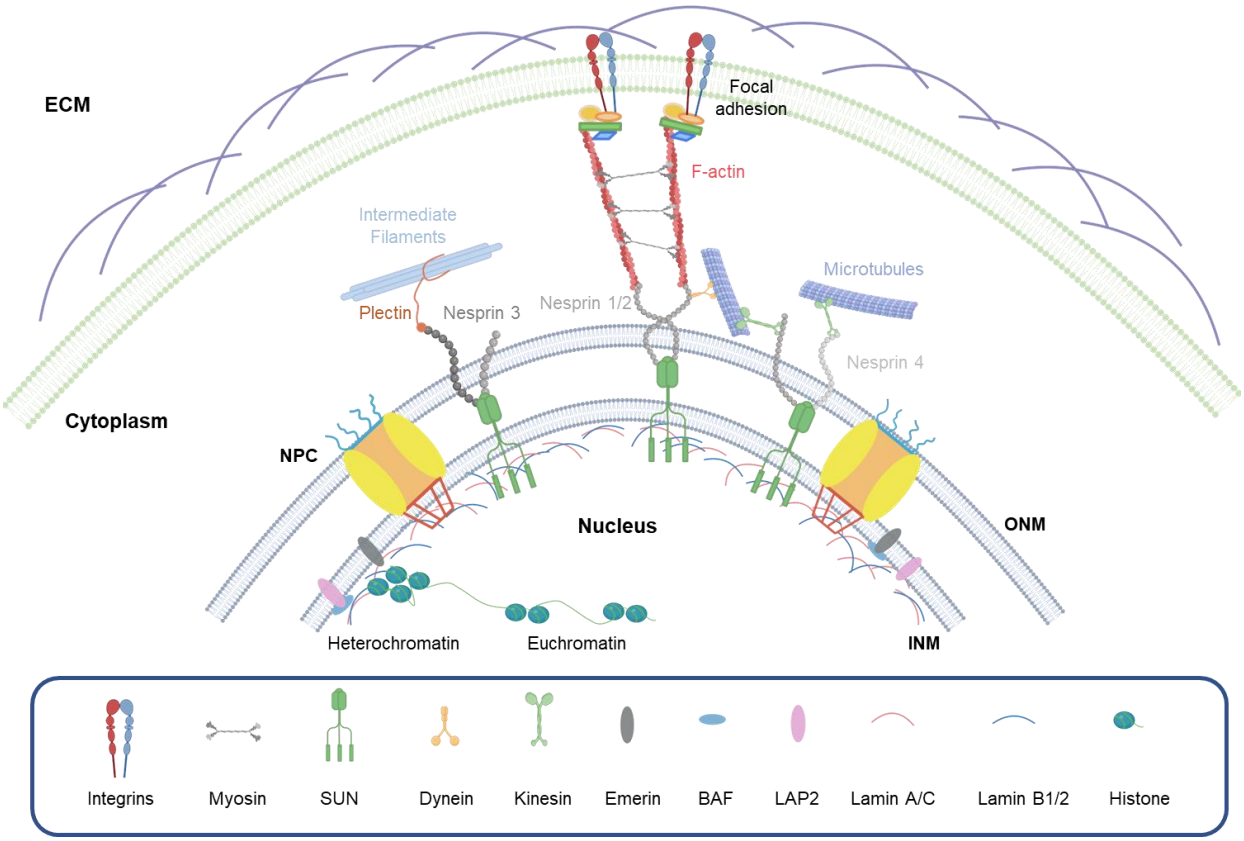

Fig. 1.5. Elements of the cytoskeleton and nucleus involved in mechanotransduction from ECM to nucleus. ONM: outer nuclear membrane, INM: inner nuclear membrane, NPC, nuclear pore complex; BAF, barrier-to-autointegration factor; LAP2, lamina-associated polypeptide 2[75].

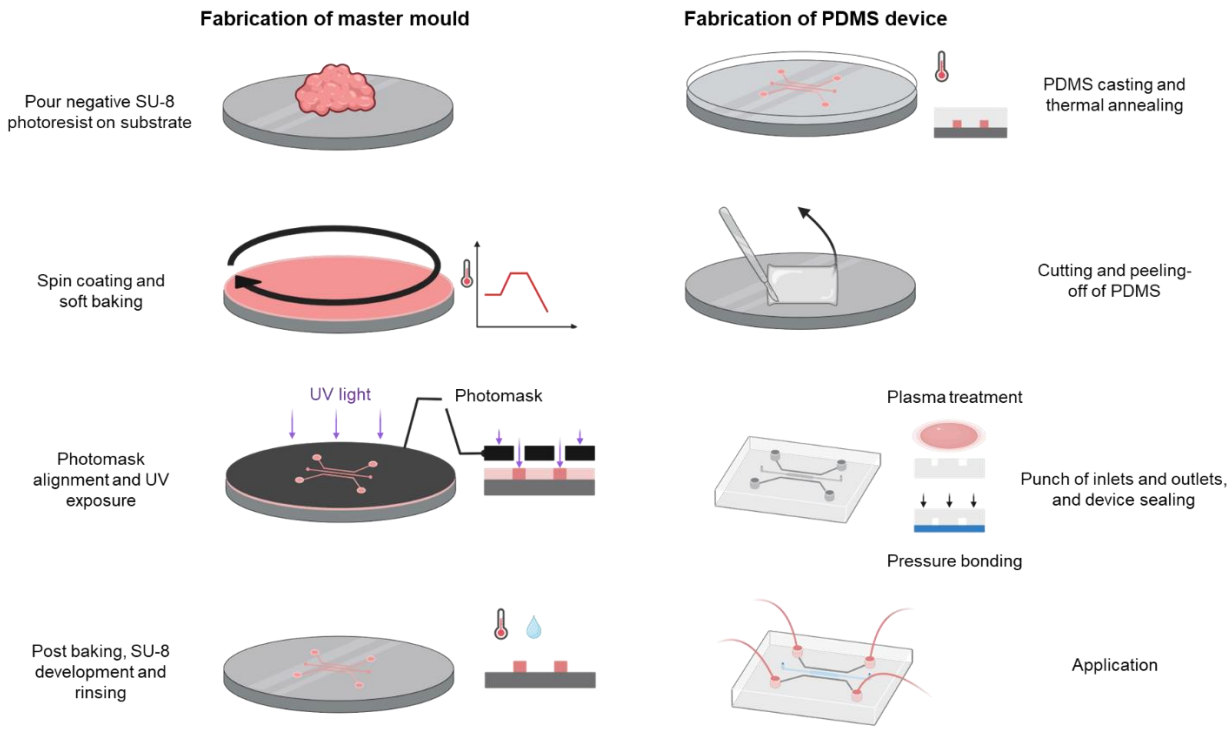

Fig. 1.6. Typical fabrication process of microfluidics device. A typical fabrication process of microfluidics device involves fabrication of a master mould using photolithography with SU-8 photoresist, and fabrication of the PDMS device from the mould using soft lithography[155].

Chapter II

Microfluidics device to promote cell reprogramming

As discussed in Chapter I, cell reprogramming has great potential in tissue regeneration, disease modelling and personalized medicine[1-3], but it is limited by relatively low conversion efficiency. A critical step in cell reprogramming is to overcome the epigenetic barrier of heterochromatin and turn on the endogenous genes for cell type conversion. Most previous studies have focused on the roles of transcriptional factors and biochemical factors in cell reprogramming, but the effects of biophysical factors are much less understood. Previous research has shown that mechanical forces could contribute to the modulation of the epigenetic state and a variety of cell functions through distinct mechanisms, with a great potential to promote cell reprogramming. Therefore, we developed microfluidics devices to deform suspended cells in a high-throughput manner to directly study how nuclear deformation could regulate the epigenetic state and cell reprogramming.

2.1 Microfluidics device induces nuclear deformation

Microfluidic devices have been used to study cell deformation, gene transfer and cancer cells[4-7], the cell viability must not been compromise while cells are being deformed by smaller microchannels. Therefore, we developed microfluidic devices with various sizes of parallel constriction microchannels to deform cells and optimized the microchannel dimensions (Fig. 2.1). Based on the size of mouse fibroblasts (19.7 ± 4.5 μm) and their nuclei (10.5 ± 1.2 μm; Fig. 2.2), we tested microchannels with the same height (15 μm) but different widths (3, 5, 7 and 9

μm). Cells passing through wide microfluidic channels (200 μm) did not show significant nuclear deformation and were used as a control in all studies.

After passing through the microchannels, cells were collected at the outlet of the microdevices and seeded onto fibronectin-coated wells. To determine if the cell membrane integrity was affected by the nuclear deformation, a fluorescently tagged antibody (Cy5-Ab) was added to the culture media of fibroblasts in suspension before and during the introduction of the fibroblasts into the microfluidic device. Cy5-Ab could be detected in 6% of cells passing through 7-μm-wide microchannels and it was not detected in the cells passing through 9-μm-wide or 200-μm-wide channels. However, Cy5-Ab could be detected in 31% and 76% of cells passing through 5-μm-wide and 3-μm-wide channels, respectively, suggesting a significant cell membrane disruption under these two conditions[5, 8]. In addition, Cy5-Ab was detected in 6.5% and 23% of nuclei in the cells passing through 5-μm-wide and 3-μm-wide channels, indicating that microchannels of less than 5 μm induced nuclear envelope rupture. Furthermore, by using fibroblasts expressing histone 2B (H2B) tagged with green fluorescent protein (H2B-GFP), significant nuclear blebbing or segregation was induced after squeezing through 3-μm-wide and 5-μm-wide channels, but not 7-μm-wide and 9-μm-wide channels (Fig. 2.3).

Previous studies have shown that cell death and DNA damage may be induce by the rupture of the cell membrane and nuclear envelope[9, 10]. To test if squeezing through microchannels will induce such damage on cells, live/dead cell staining was performed, and the results showed that 7-μm-wide and 9-μm-wide channels did not induce noticeable cell death. In contrast, 3-μm-wide and 5-μm-wide channels induced significant cell death (20–50%) DNA damage (Fig. 2.4). Based on these findings, 7-μm-wide microchannels were used for the rest of the studies. After optimization based on 7-μm-wide channel, a flow rate up to 20 μL/min would not cause cell

aggregation or affect cell viability. Therefore, a flow rate of 20 μL/min was used for the rest of the tests which resulted in a transit time of 6.8 milliseconds (ms) in average for a cell to pass through a 7-μm-wide microchannel, inducing a transient nuclear deformation. In addition, the cell nucleus was more elongated after squeezing, followed by a gradual recovery in 24hrs after squeezing (Fig. 2.5).

2.2 Nuclear deformation promotes iN reprogramming

In order to test if microchannel-induced nuclear deformation had any effect on cell reprogramming, a direct reprogramming model from fibroblasts into iN cells was employed. Adult mouse fibroblasts were transduced with doxycycline (Dox)-inducible lentiviral constructs containing the three reprogramming factors BRN2, ASCL1 and MYT1L (BAM) as depicted in the timeline for the reprogramming experimental procedure. Two days later, Dox was added (designated as day 0) to induce the expression of BAM transgenes and proteins within a few hours, followed by squeezing the cells through the microchannels. The cells were then collected and seeded onto fibronectin-coated glass coverslips and cultured in serum-free N2B27 medium. Seven days after induced mechanical deformation, cells were fixed and stained for Tuj1 (for neuron-specific class III beta-tubulin, Tubb3) to determine the reprogramming efficiency. The reprogramming efficiency of cells going through 200-μm-wide channels (as the control group) was not significantly different from the cells under static culture conditions, while the reprogramming efficiency of cells squeezed through 7-μm-wide increased significantly (approximately eightfold) compared to the control group. Microchannels smaller than 7 μm (i.e. 5 μm and 3 μm) compromised reprogramming efficiency due to the decreased cell viability. 9-μm-wide microchannels might not induce sufficient nuclear deformation and resulted in a lower

reprogramming efficiency compared to 7-μm-wide microchannels. Moreover, the maturation of reprogrammed iN was characterized with the mature neuronal markers microtubule associated protein 2 (MAP2) and synapsin at four weeks after squeezing experiments (Fig. 2.6).

2.3 Nuclear deformation induces epigenetic changes

It has been demonstrated that nuclear deformation could result in a significant increase in reprogramming efficiency, to better understand the underlying mechanism, the potential involvement of epigenetic changes which contribute to control of the on/off state of phenotypic genes were investigated. First, a fluorescence resonance energy transfer (FRET) biosensor targeted at the nucleosome to monitor the levels of a heterochromatin mark H3K9me3 was utilized[11], and the results showed that the H3K9me3 FRET signal decreased significantly in fibroblasts while passing through 7-μm-wide microchannels. To observe the temporal change in the same cells, the pressure and flow rate was lowered to slow down the squeezing process. Cells passing through 200-μm-wide channels did not show significant change in H3K9me3 FRET signal, while those passing through 7-μm-wide microchannels showed a decreased H3K9me3 FRET signal within 1 minute (Fig. 2.7).

To determine whether the epigenetic changes persisted after squeezing and if this squeezing process could induce changes in other epigenetic marks, immunostaining analysis of multiple heterochromatin and euchromatin marks at multiple time points within the first 24 hours after the squeezing experiments was performed. Consistent with FRET results, a significant decrease in H3K9me3 at 3 hours and 12 hours after squeezing was observed, which went back to the same level as the cells in the control group after 24 hours. The global decrease in H3K9me3 after

squeezing was confirmed by western blotting analysis (Fig. 2.8). These results indicated that nuclear deformation could result in a transient reduction of heterochromatin. Additionally, the acetylated histone marks including AcH3 and H3K9ac, and other histone methylation marks including H3K4me1, H4K20me3 and H3K27me3, were examined, while the results did not show significant global changes in response to forced nuclear deformation (Fig. 2.9).

Despite histone modifications, it has been demonstrated that DNA methylation influences chromatin organization, which is critical for cell reprogramming[12]. To study if nuclear deformation could affect DNA methylation, we analyzed DNA condensation and the level of 5-methylcytosine (5-mC), a DNA methylation marker, in fibroblasts after squeezing with immunostaining analysis and enzyme-linked immunoassay (ELISA). Both of these results showed that there was a significant decrease in DNA methylation for at least 12 hours after squeezing, which indicated that nuclear deformation caused chromatin modifications in both H3K9me3 and 5-mC (Fig. 2.10). These results suggested that the suppression of H3K9me3 and DNA methylation might be the major mediators of the increase in iN reprogramming efficiency induced by the squeezing.

2.4 Scale-up of the mechanopriming process

To determine whether the nuclear deformation by squeezing cells through microfluidics devices could enhance the reprogramming of different cell types, similar experiments were performed by using macrophages transduced with BAM (squeezed with 5-μm-wide channel) and fibroblasts transduced with OSKM factors (squeezed with 7-μm-wide channel). Interestingly, we found that both iN reprogramming from macrophages and iPSCs reprogramming from fibroblasts were

significantly enhanced after squeezing, suggesting that this mechanical squeezing can be utilized as a general approach to prime the epigenetic state of cells to promote cell reprogramming (Fig. 2.11).

To scale up the mechano-preconditioning of cells for reprogramming, a higher-throughput microfluidic device (HMD) was developed, which contained ten times more microchannels (400 microchannels) than the original microfluidic device (OMD) with 36 microchannels, within a similar area. The design was validated by simulation with COMSOL Multiphysics®, showing a uniformly distributed velocity profile in all the microchannels. HMD contributed to a much higher processing rate of cell squeezing, which was five times higher than OMD. In addition, this HMD significantly increased the yield of cell collection, while also maintaining high cell viability and significantly increased iN efficiency (Fig. 2.12).

2.5 Conclusion

Here we demonstrated that the nuclear deformation, induced by squeezing cells through microchannels, has a mechanopriming effect to help overcome the epigenetic barrier during cell reprogramming[13], by downregulating the H3K9me3 and DNA methylation level. Our data also suggest that transient biophysical modulation of the epigenetic state is universal and independent of cell type and reprogramming factors. This work provides the potential to translate mechanobiology findings into cell engineering applications. Such scalable microfluidic devices provide a well-controlled microenvironment, which can be used to engineer a variety of cells in a high throughput manner, such as fibroblasts, stem cells and immune cells, and to facilitate the conversion of cell types from one to another.

2.6 Methods

All experiments were performed in accordance with relevant guidelines and ethical regulations approved by the University of California, Los Angeles (UCLA), Institutional Biosafety Committee (BUA-2016-222).

Cell isolation, culture and reprogramming

Mice utilized in these studies were housed under specific pathogen-free conditions and 12-hour light/12-hour-dark cycles with a control of temperature (20–26 °C) and humidity (30–70%). All experiments, including breeding, maintenance and euthanasia of animals, were performed in accordance with relevant guidelines and ethical regulations approved by the UCLA Institutional Animal Care and Use Committee (protocol nos ARC- 2016-036 and ARC-2016-101).

Fibroblasts were isolated from ear tissues of adult (1 month old, male and female) C57BL/6 mice (Jackson Laboratory, 002052), and R26 M2rtTA;Col1a1-tetO-H2B-GFP compound mutant mice (Jackson Laboratory, 016836), and expanded in fibroblast medium: DMEM medium (Gibco, 11965), 10% foetal bovine serum (FBS; Gibco, 26140079) and 1% penicillin/streptomycin (Gibco, 15140122). For all experiments, passage-2 cells were used and synchronized upon reaching 80% confluency using DMEM with 1% FBS for 24 hours before the transduction with viruses containing BAM constructs. The following day (day 0), the medium was changed to mouse embryonic fibroblast (MEF) medium containing Dox (2 ng ml^{-1}, Sigma) to initiate the expression of the transgenes and thus, reprogramming. After 6 hours, transduced fibroblasts were passaged and subjected to microfluidic deformation using microchannels of various widths. Cells were then seeded onto glass slides coated with 0.1 mg ml^{-1} fibronectin (Thermo Fisher, 33016015) overnight at a density of 3,000 cells cm^{-2}. Twenty-four hours later (day 1), cells were

cultured in N2B27 medium: DMEM/F12 (Gibco, 11320033), N-2 supplement (Gibco, 17502048), B-27 supplement (Gibco, 17504044), 1% penicillin/streptomycin and Dox (2 ng ml^{-1}, Sigma) and half medium changes were performed every two days. On day 7 after microfluidic deformation, cells were fixed and stained for Tuj1 to determine the reprogramming efficiency. The iN cells were identified based on positive Tuj1 staining and a neuronal morphology. The reprogramming efficiency was determined as the percentage of iN cells on day 7 relative to the number of the cells initially seeded. For long-term studies where maturation and functionality of the iN cells were examined, cells were kept in culture for five weeks. Reprogramming of iPSC from wild type fibroblasts was performed as described previously[14].

Macrophages for reprogramming experiments were derived from differentiated monocytes. Monocytes were isolated from the bone marrow of adult C57BL/6 mice and expanded in monocyte medium: RPMI 1640 (Gibco, 11875093), 10% FBS (Gibco, 26140079) and 1% penicillin/streptomycin (Gibco, 15140122). The next day, macrophage-colony stimulating factor (M-CSF; 50 ng ml^{-1}, Thermo Fisher, PMC2044) was added to the medium and cells were cultured for an additional two days. Cells were then washed three times with phosphate buffered saline (PBS) before transduction with viruses containing BAM constructs.

Microfabrication of the microfluidic device

The moulds of designed microfluidic devices for cell squeezing were fabricated via photolithography. A 15-μm-thick layer of SU-8 2015 (Microchem Corporation, 3,300 r.p.m.) was spun-coated onto a four-inch silicon wafer, followed by a standard photolithography process according to the manufacturer's instruction. A base and curing agent of polydimethylsiloxane (PDMS; Sylgard 184, Dow Corning) was mixed in a 10:1 weight ratio and degassed in a vacuum chamber for one hour to remove air bubbles before being poured onto the mould. After curing at

65 °C for 4 hours, the PDMS mould was punched to make inlets and outlets for tubing connections. The PDMS mould and precleaned glass were bonded after treatment with oxygen plasma for 30 seconds. The bonded chips were baked at 65 °C for 10 minutes to enhance the bonding.

Lentiviral preparation and transduction

Dox-inducible lentiviral vectors for Tet-O-FUW-Brn2, Tet-O-FUW-Ascl1, Tet-O-FUW-Myt1l and FUW-rtTA plasmids were used to transduce fibroblasts for ectopic expression of BRN2, ASCL1, MYT1L, GFP and reverse tetracycline transactivator (rtTA). The STEMCCA lentiviral vector was used for the ectopic expression of OSKM[14]. Lentivirus was produced by using established calcium phosphate transfection methods, and Lenti-X Concentrator (Clontech, 631232) was utilized to concentrate viral particles according to the manufacturer's protocol. Stable virus was aliquoted and stored at −80 °C. Fibroblasts were plated and synchronized for 24 hours before viral transduction in the presence of polybrene (8 μg ml^{-1}, Sigma, H9268). Cells were incubated with the virus for 24 hours before performing microfluidic deformation experiments.

Cell viability assays

After cells passed through the microdevice, 10×10^3 fibroblasts were plated and allowed to attach for 3 hours in a 96-well plate. Live and dead assays were performed using the LIVE/DEAD Cell Imaging Kit (Invitrogen, R37601) according to the manufacturer's protocol. Cells were incubated with an equal volume of ×2 working solution for 15 minutes at room temperature. Epifluorescence images were collected using a Zeiss Axio Observer Z1 inverted fluorescence microscope and analyzed using ImageJ.

DNA damage assays

After cells passed through the microdevice, 5×10^3 fibroblasts were plated and allowed to attach for 3 hours in a 96-well plate. DNA damage assays were performed using the HCS DNA Damage Kit (Invitrogen, H10292) according to the manufacturer's protocol. Cells were fixed with 4% paraformaldehyde solution for 15 minutes at room temperature and permeabilized by 0.25% Triton X-100 in PBS for another 15 minutes at room temperature. Cells were washed three times with PBS and incubated in 1% bovine serum albumin (BSA) solution for 1 hour, followed by phospho-H2AX (pH2AX) antibody (1:1,000) for 1 hour at room temperature and then Alexa Fluor 555 goat anti-mouse IgG (H+L) secondary (1:5,000) with Hoechst 33342 (1:6,000) for another 1 hour at room temperature after removing the antibody. Epifluorescence images were collected using a Zeiss Axio Observer Z1 inverted fluorescence microscope and analysed using ImageJ. Results were normalized to control samples (that is, cell passing through channels of >200 μm), and cells treated with 200 nM lipopolysaccharide served as a positive control.

Immunofluorescence staining and microscopy

Samples collected for immunofluorescence staining at the indicated time points were washed once with PBS and fixed in 4% paraformaldehyde for 15 minutes. Samples were washed three times with PBS for 5 minutes each and permeabilized using 0.5% Triton X-100 for 10 minutes. After three subsequent PBS washes, samples were blocked with 5% normal donkey serum (Jackson Immunoresearch, 017000121) in PBS for 1 hour. Samples were incubated with primary antibodies (Table 2.1) in antibody dilution buffer (1% normal donkey serum + 0.1% Triton X-100 in PBS) for either 1 hour or overnight at 4 °C followed by three PBS washes and a 1 hour incubation with donkey anti-mouse IgG (H+L) highly cross-adsorbed secondary antibody, Alexa

Fluor 488 (Thermo Fisher, A-21202); donkey anti-mouse IgG (H+L) highly cross-adsorbed secondary antibody, Alexa Fluor 546 (Thermo Fisher, A-10036); donkey anti-rabbit IgG (H+L) highly cross-adsorbed secondary antibody, Alexa Fluor 488 (Thermo Fisher, A-21206); and/or donkey anti-rabbit IgG (H+L) highly cross-adsorbed secondary antibody, Alexa Fluor 546 (Thermo Fisher, A-10040). Nuclei were stained with 4′,6-diamidino-2-phenylindole (DAPI; Thermo Fisher, D3571) in PBS for 10 minutes. Epifluorescence images were collected using a Zeiss Axio Observer Z1 inverted fluorescence microscope and analysed using ImageJ. Confocal images were collected using a Leica SP8-STED/ FLIM/FCS Confocal and analysed using ImageJ.

For DNA methylation staining, samples were fixed with ice-cold 70% ethanol for 5 minutes followed by three PBS washes. Samples were then treated with 1.5 M HCl for 30 minutes and washed thrice with PBS. The immunostaining procedure proceeded from the donkey serum blocking step as aforementioned.

Average histone marker intensities per nuclei were quantified using an ImageJ macro. Gaussian blur, thresholding, watershed and analyse particle functions were applied to the DAPI channel to create individual selections for each nucleus. This mask was applied to the corresponding stain image to measure the average fluorescence intensity within each nucleus.

DNA methylation assay

After cells passed through the device, cells were collected, and 10×10^5 cells were plated in 60 mm dishes. At different time points, cells were trypsinized and DNA was extracted by Invitrogen PureLink Genomic DNA mini kit (Invitrogen, K1820-01). The 5-mC level was analysed by the MethylFlash Global DNA Methylation (5-mC) ELISA Easy Kit (Epigentek, P-1030) according

to the manufacturer's instructions. Briefly, 100 ng of sample DNA was bonded into the assay wells and incubated with a 5-mC detection complex solution for 60 minutes. Then colour developer solution was added into assay wells, and the absorbance at 450 nm was measured by using a plate reader (Infinite 200Pro, 30050303).

FRET biosensor

Lentiviruses of H3K9me3 were produced from Lenti-X 293T cells (Clontech Laboratories, 632180) cotransfected with a pSin containing biosensor and the viral packaging plasmids pCMV-△8.9 and pCMV-VSVG using the ProFection Mammalian Transfection System (Promega, catalog no. E1200). Viral supernatant was collected 48 hours after transfection, filtered with 0.45 μm filter (Sigma-Millipore). Primary fibroblasts were transduced with the virus, and the cells expressing the biosensor were sorted using flow cytometry (Sony, SH800). Images of the FRET experiment were taken with a Nikon Eclipse Ti inverted microscope equipped with a cooled charge-coupled device (CCD) camera, a 420DF20 excitation filter, a 450DRLP dichroic mirror and two emission filters controlled by a filter changer (480DF30 for ECFP and 535DF35 for FRET) as described previously[11, 15]. The images were acquired, and the enhanced cyan fluorescent protein (ECFP)/ FRET ratio was calculated and visualized by MetaFluor 7.8 (Molecular Devices).

Western blotting

Equal amounts of total protein (50 μg) from each sample were separated in a 10% SDS-PAGE gel and transferred to a polyvinylidene fluoride membrane at 120 V for 2 hours at room temperature. The blot was blocked with 5% nonfat dry milk suspended in ×1 TBS (25 mM Tris, 137 mM NaCl and 2.7 mM KCl) for 1 hour. Membranes were incubated sequentially with

primary antibodies (Table 2.1) and secondary antibodies (anti-mouse IgG horseradish peroxidase (HRP)-linked antibody (Cell Signaling, 7076S) and anti-mouse IgG HRP-linked antibody (Cell Signaling, 7074S)). Bands were scanned using a densitometer (Bio-Rad) and quantified using the Quantity One v.4.6.3 software (Bio-Rad).

Statistics and reproducibility

All data are presented as mean ± 1 s.d., where sample size (n) is ≥3. Comparisons among values for groups greater than two were performed by using a one-way analysis of variance (ANOVA) followed by a Tukey's post-hoc test. For two group analysis, a two-tailed, unpaired Student's t-test was used to analyse differences. For all cases, P values less than 0.05 were considered statistically significant. Origin 2018 software was used for all statistical evaluations. At least three independent experiments were performed to confirm findings.

References

1. Aydin, B. and E.O. Mazzoni, Cell Reprogramming: The Many Roads to Success. Annu Rev Cell Dev Biol, 2019. 35: p. 433-452.

2. Karagiannis, P., et al., Induced Pluripotent Stem Cells and Their Use in Human Models of Disease and Development. Physiological Reviews, 2019. 99(1): p. 79-114.

3. Wang, H., et al., Direct cell reprogramming: approaches, mechanisms and progress. Nat Rev Mol Cell Biol, 2021. 22(6): p. 410-424.

4. Ding, X., et al., High-throughput Nuclear Delivery and Rapid Expression of DNA via Mechanical and Electrical Cell-Membrane Disruption. Nat Biomed Eng, 2017. 1.

5. Denais, C.M., et al., Nuclear envelope rupture and repair during cancer cell migration. Science, 2016. 352(6283): p. 353-8.

6. Paul, C.D., P. Mistriotis, and K. Konstantopoulos, Cancer cell motility: lessons from migration in confined spaces. Nat Rev Cancer, 2017. 17(2): p. 131-140.

7. Gossett, D.R., et al., Hydrodynamic stretching of single cells for large population mechanical phenotyping. Proc Natl Acad Sci U S A, 2012. 109(20): p. 7630-5.

8. Naim, B., et al., Passive and facilitated transport in nuclear pore complexes is largely uncoupled. J Biol Chem, 2007. 282(6): p. 3881-8.

9. Raab, M., et al., ESCRT III repairs nuclear envelope ruptures during cell migration to limit DNA damage and cell death. Science, 2016. 352(6283): p. 359-62.

10. Irianto, J., et al., DNA Damage Follows Repair Factor Depletion and Portends Genome Variation in Cancer Cells after Pore Migration. Curr Biol, 2017. 27(2): p. 210-223.

11. Peng, Q., et al., Coordinated histone modifications and chromatin reorganization in a single cell revealed by FRET biosensors. Proc Natl Acad Sci U S A, 2018. 115(50): p. E11681-E11690.

12. De Carvalho, D.D., J.S. You, and P.A. Jones, DNA methylation and cellular reprogramming. Trends Cell Biol, 2010. 20(10): p. 609-17.

13. Vierbuchen, T., et al., Direct conversion of fibroblasts to functional neurons by defined factors. Nature, 2010. 463(7284): p. 1035-41.

14. Downing, T.L., et al., Biophysical regulation of epigenetic state and cell reprogramming. Nat Mater, 2013. 12(12): p. 1154-62.

15. Liu, L., et al., Integration of FRET and sequencing to engineer kinase biosensors from mammalian cell libraries. Nat Commun, 2021. 12(1): p. 5031.

Figures

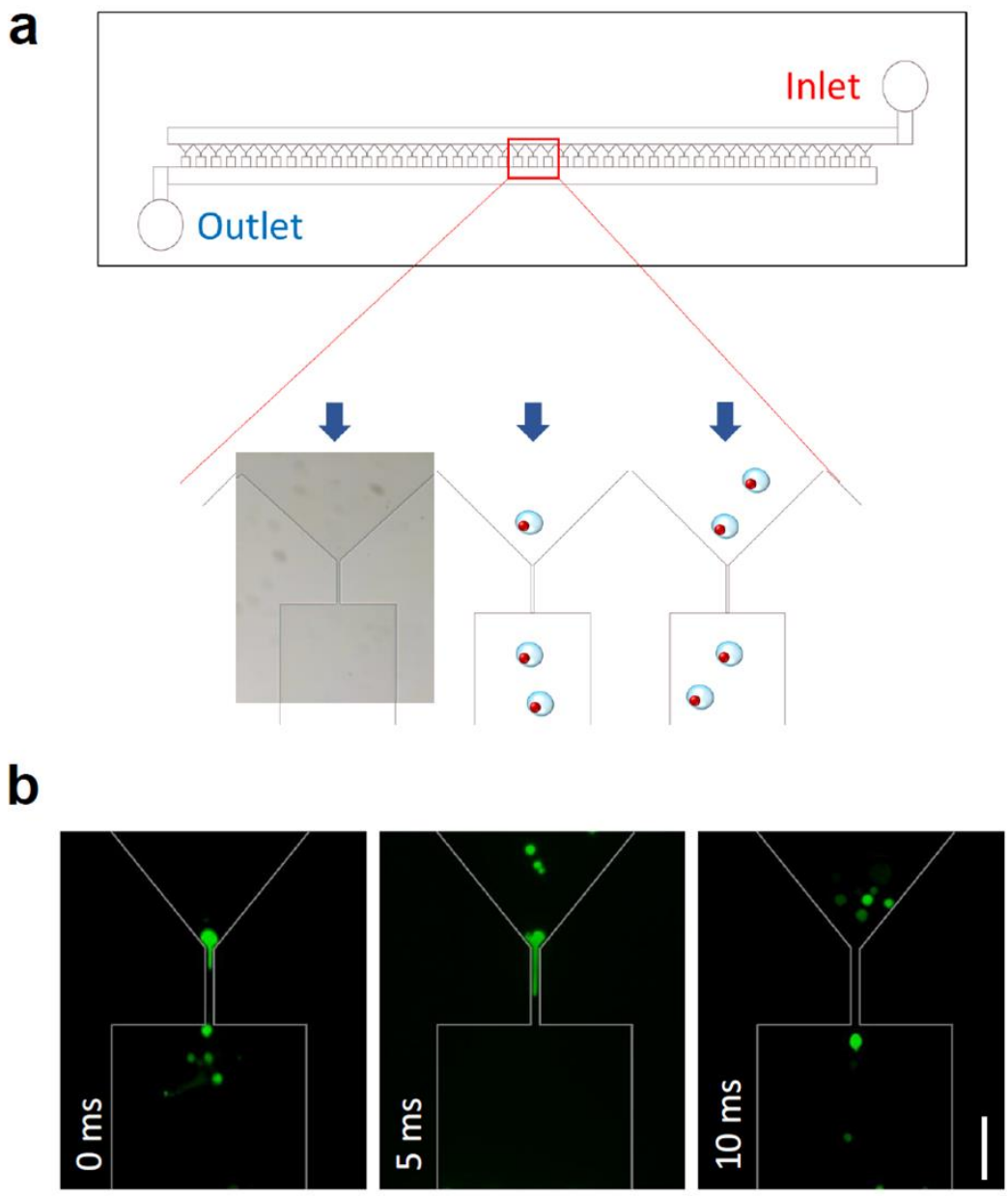

Fig. 2.1. A microdevice with parallel microchannels to force transient cell deformation. (a) Schematic illustrating the design of a microdevice with multiple microchannels to deform cells in parallel. (b) Mouse fibroblasts were labeled with Cell Tracker Green, and live cell imaging was performed to monitor cells passing through the microchannels Scale bar, 50 μm.

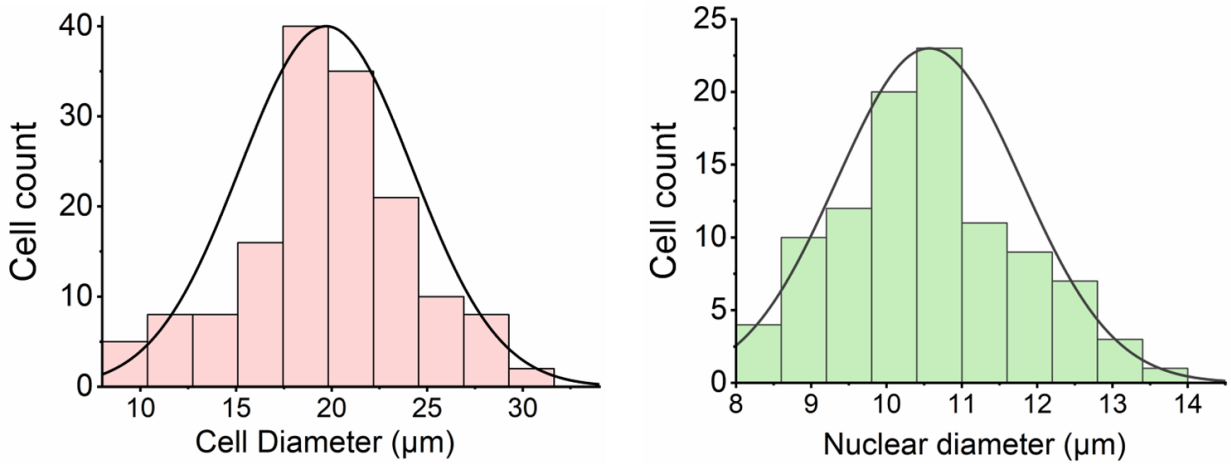

Fig. 2.2. Mouse fibroblast size. Quantification of cell diameter based on TC20 Cell Counter (Bio-Rad; n = 100) and quantification of nuclear diameter based on Hoechst staining (n = 100).

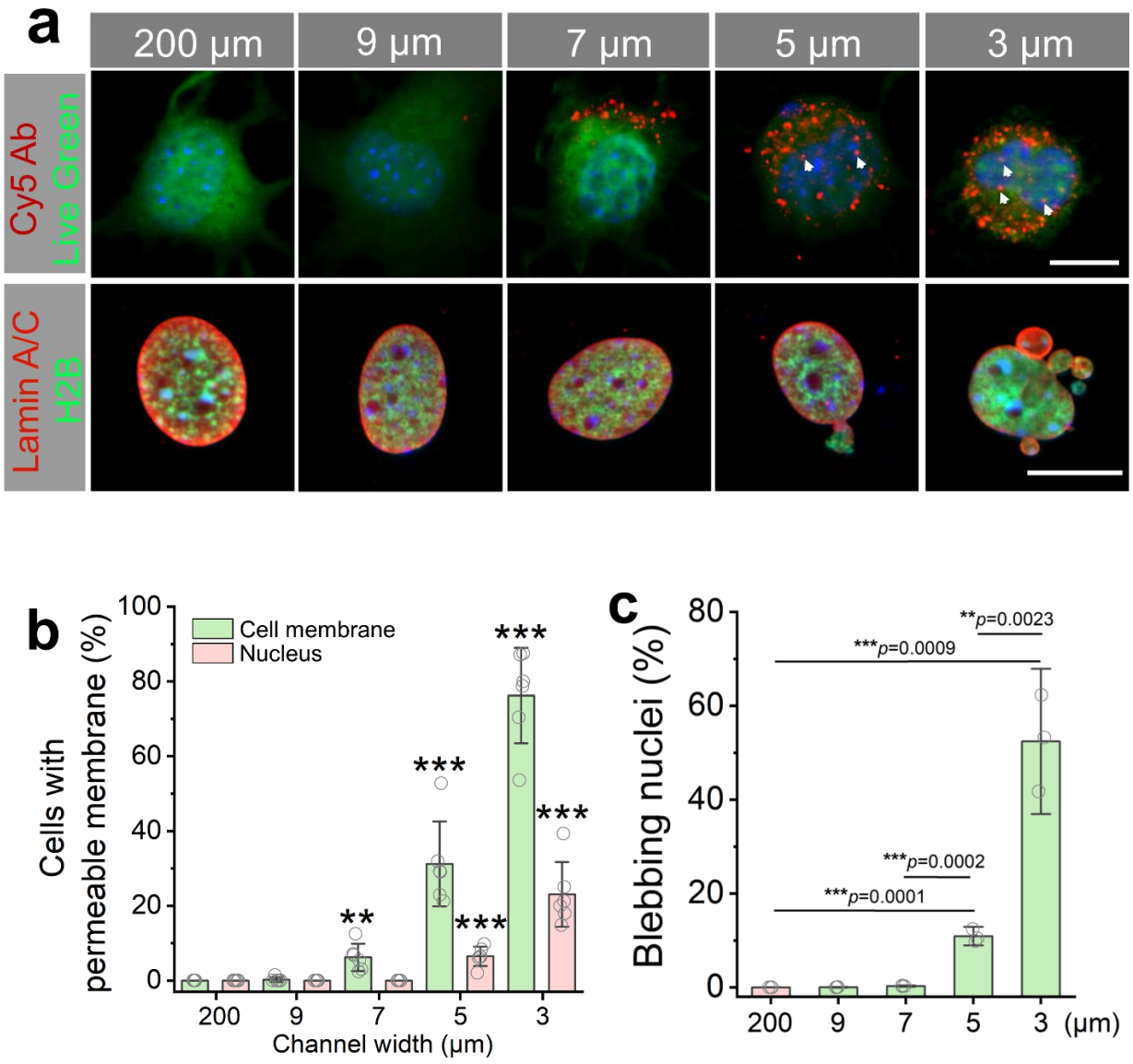

Fig. 2.3. Membrane integrity after squeezing. (a) Immunofluorescent images of cells that were deformed by using microdevices with different microchannel widths. The permeability or non-specific transport of the cell membrane and nuclear envelope was examined 3 hours after cells passed through the microchannel by using Cy5-Ab (top). Live green dye was used to label live cells. White arrows indicate Cy5-Ab in the nuclei. Scale bar, 10 μm. Immunofluorescent images (bottom) of H2B-GFP fibroblasts that were deformed by using microdevices with different

microchannel widths, seeded onto fibronectin-coated glass slides for 3 hours and stained with lamin A/C. Scale bar, 10 μm. (b) The percentage of cells with extracellular Cy5-Ab penetrating the cell membrane (green) and nuclear envelope (red) was quantified in live cells (n = 6). (c) The percentage of nuclei with blebbing was quantified based on DAPI staining Each sample includes at least 5,000 cells (n=3). All squeezing groups were compared with the 200 μm group. The data represents the mean ± standard deviation (SD).

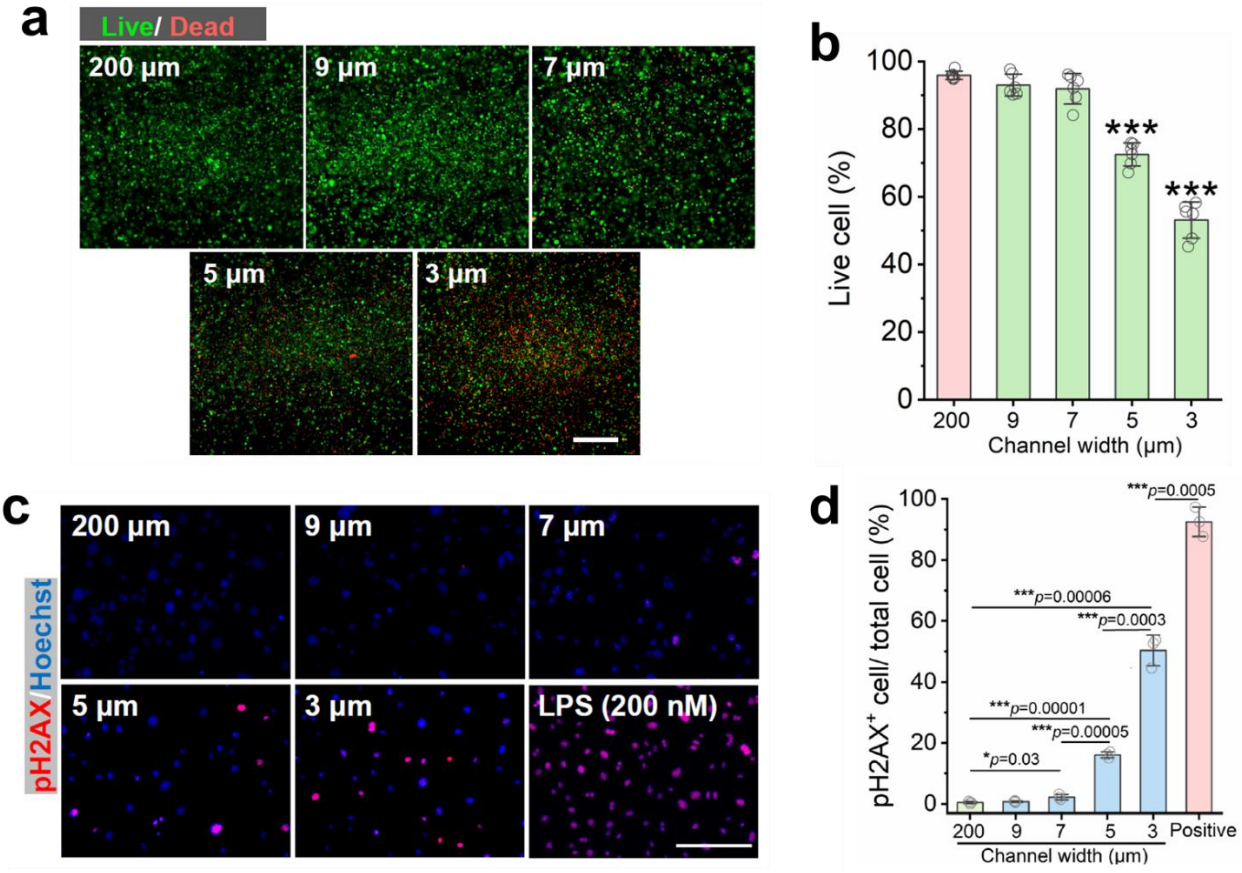

Fig. 2.4. Cell viability after squeezing. (a) Immunofluorescent images show the viability of mouse fibroblasts at 3 hours after passing through microchannels of various widths as determined by the LIVE/DEAD assay. Scale bar, 1 mm. (b) The percentage of live cells after BAM-transduced fibroblasts passed through microchannels of various channel widths (n = 6). (c) Immunofluorescent images show DNA damage in fibroblasts at 3 hours after passing through microchannels of various widths as determined by the HCS DNA damage assay, where lipopolysaccharide (LPS) at 200 nM was used as a positive control. Scale bar, 100 μm. (d) The percentage of $pH2Ax^{+}$ cells was quantified based on immunofluorescent images (n=3). All squeezing groups were compared with the 200-μm group. The data represents the mean ± SD.

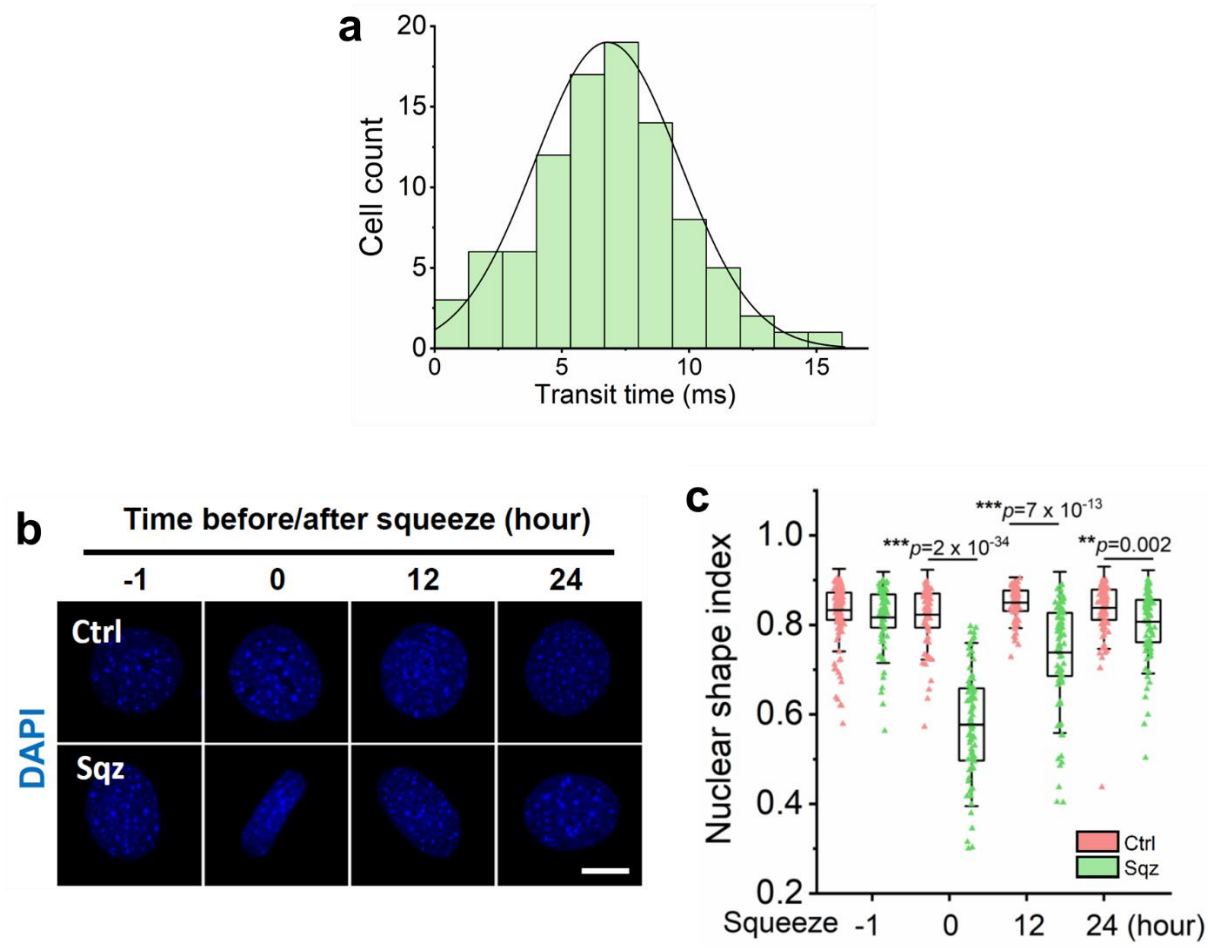

Fig. 2.5. Nuclear shape change induced by squeezing. (a) Quantification of transit time in milliseconds as cells passed through the microchannels (n = 94). (b) Immunofluorescent images of nuclei before and after cells were squeezed through the microchannel. Control (Ctrl) cells passing through 200 μm channels; Squeezed (Sqz) cells passing through 7 μm microchannels. Scale bar, 10 μm. (c) Quantification of nuclear shape index of squeezed cells at the indicated time points (n=80). Nuclear shape index is defined as $4\pi \times A/C^2$ where A is the projected area of the nucleus and C is the perimeter of the nucleus.

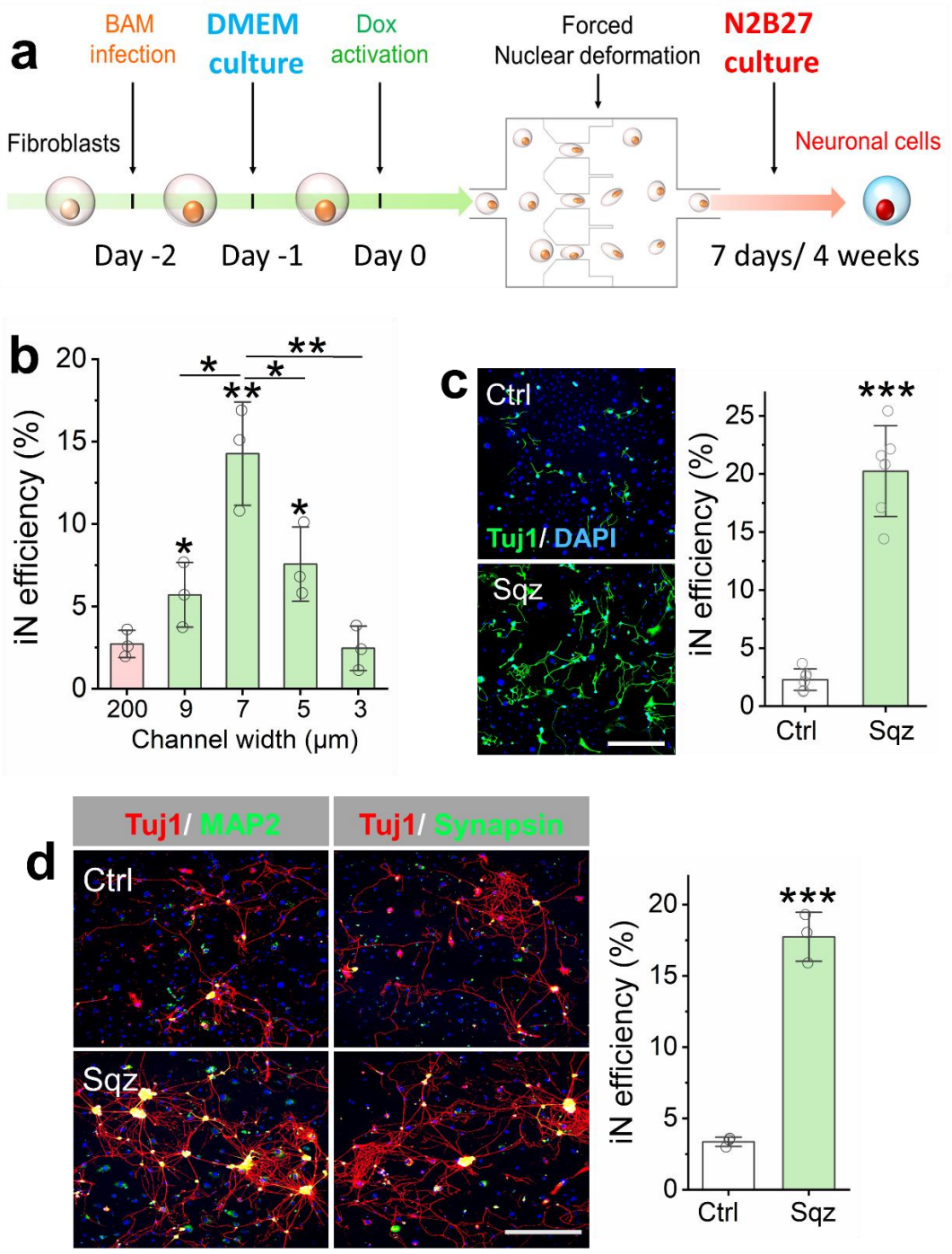

Fig. 2.6. Enhanced iN reprogramming efficiency after squeezing. (a) Experimental timeline for nuclear-deformation-induced iN reprogramming. (b) Effect of microchannel width on iN reprogramming efficiency on day 7 (n = 3), while the iN efficiency was determined by normalizing the number of Tuj1$^+$ cells to the number of cells initially seeded. (c) Reprogramming

efficiency of BAM-transduced fibroblasts of squeezed (7μm-wide-channel) and control groups on day 7 (n = 6). Scale bar, 200 μm. (d) Representative images of $Tuj1^+$ cells expressing MAP2 and synapsin at four weeks after squeezing experiments. Scale bar, 200 μm. Reprogramming efficiency of BAM-transduced fibroblasts at four weeks after nuclear deformation was determined by $synapsin^+$ staining (n = 3).

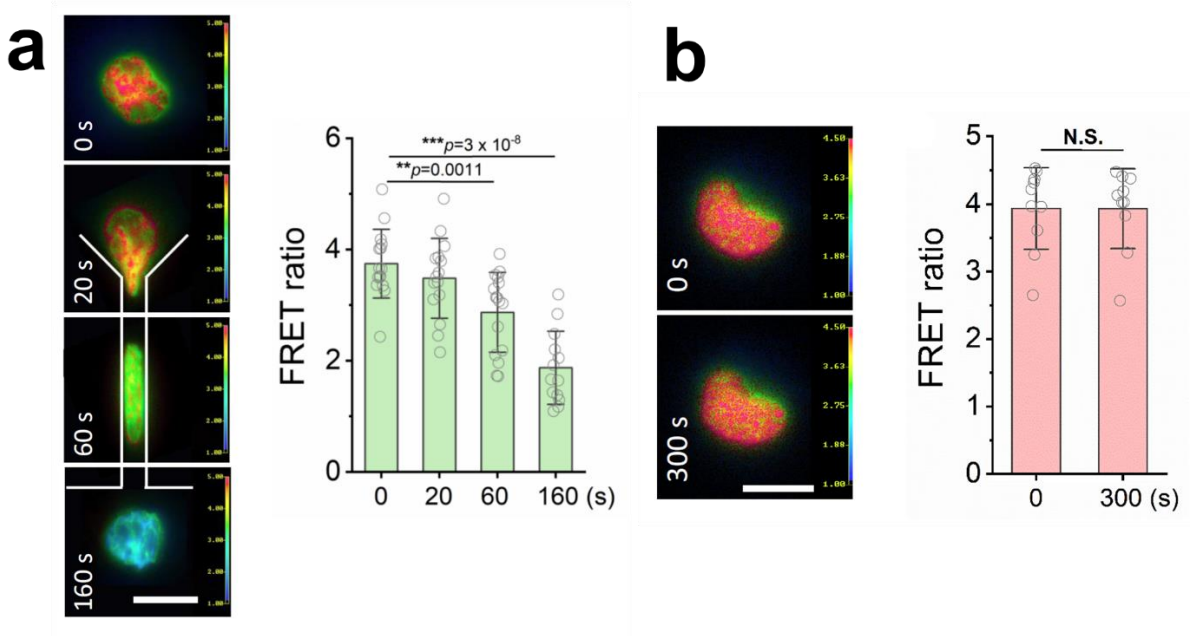

Fig. 2.7. Real-time monitoring of H3K9me3 level when cells were passing through the microchannel. (a) Live cell imaging was performed to monitor FRET signal changes in H3K9me3 during cell squeezed through a 7-μm-wide microchannel. Images were captured at 0, 20, 60 and 160 seconds as H3K9me3 FRET sensor transduced fibroblasts passed through the microchannel. Red color indicates higher level of H3K9me 3 and green indicates lower FRET signal Scale bar, 10 μm. H3K9me3 FRET signal was quantified at different time points, compared to that at 0 seconds. (b) The same experiment was performed with a 200-μm-wide channel. The quantification of FRET signal showed no significant change after 300 seconds.

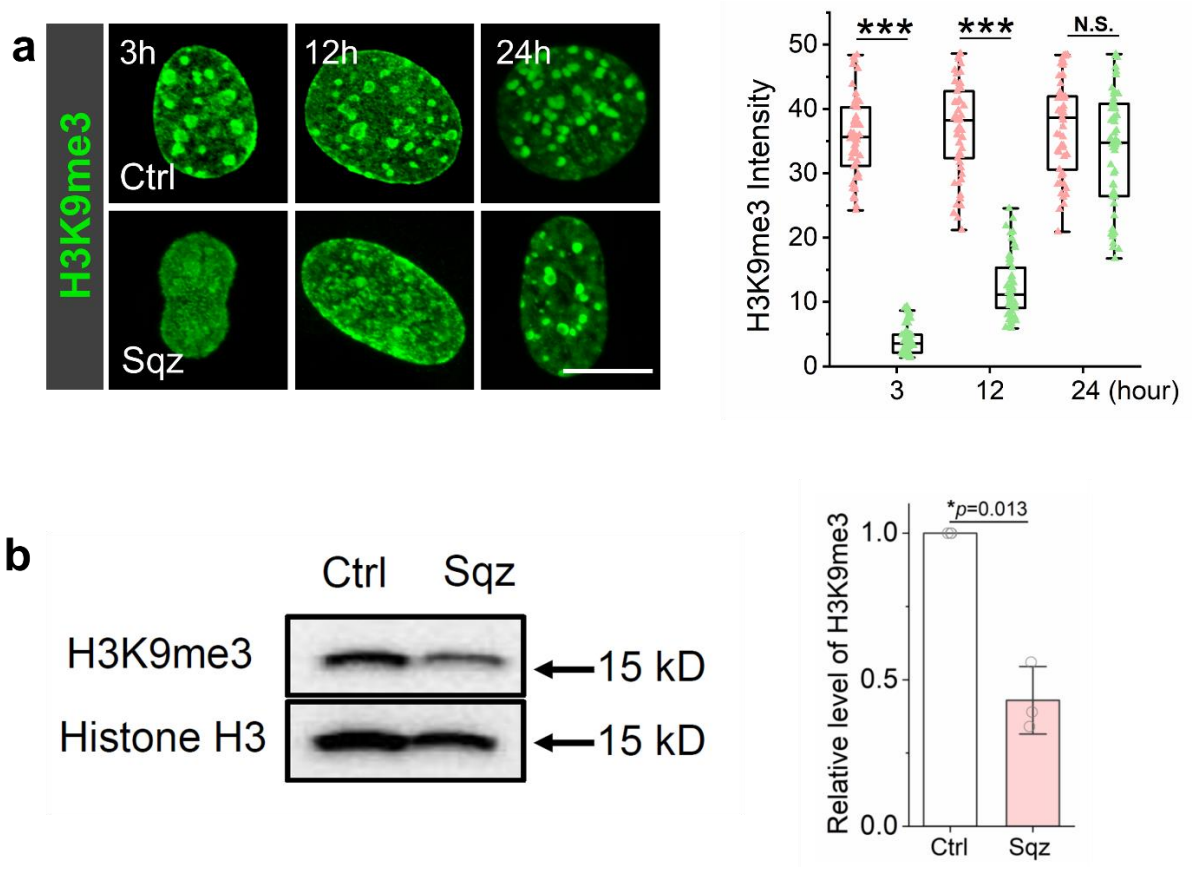

Fig. 2.8. Transient decrease of H3K9me3 level induced by nuclear deformation. (a) Immunostaining of H3K9me3 in the nucleus at the indicated time points after squeezing. Scale bar, 10 μm. H3K9me3 intensity in control and squeezed cells at the indicated time points was quantified (n = 53). (b) Total histone extracts were isolated from BAM transduced fibroblasts using the Histone Extraction Kit (Abcam, ab221031, USA) at 3 hours after squeezing experiments. The levels of H3K9me3 and histone H3 were examined and quantified using western blotting.

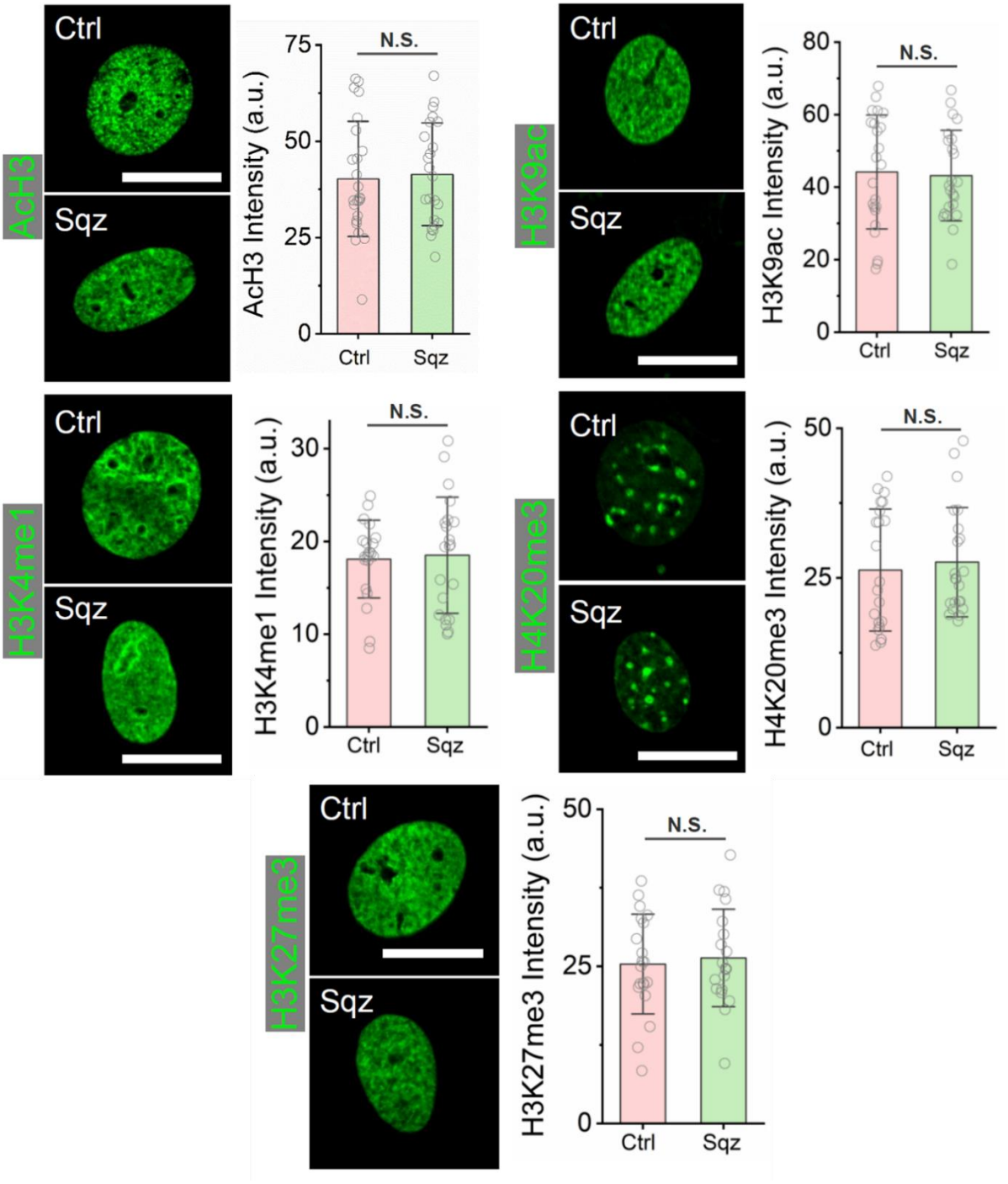

Fig. 2.9. Effect of forced nuclear deformation on histone marks. Representative immunofluorescent images show the level and distribution of various histone marks in BAM transduced fibroblasts 3 hours after squeezing. Quantification of histone mark intensity was based on immunofluorescent images, a.u.: arbitrary unit (n= 30 cells).

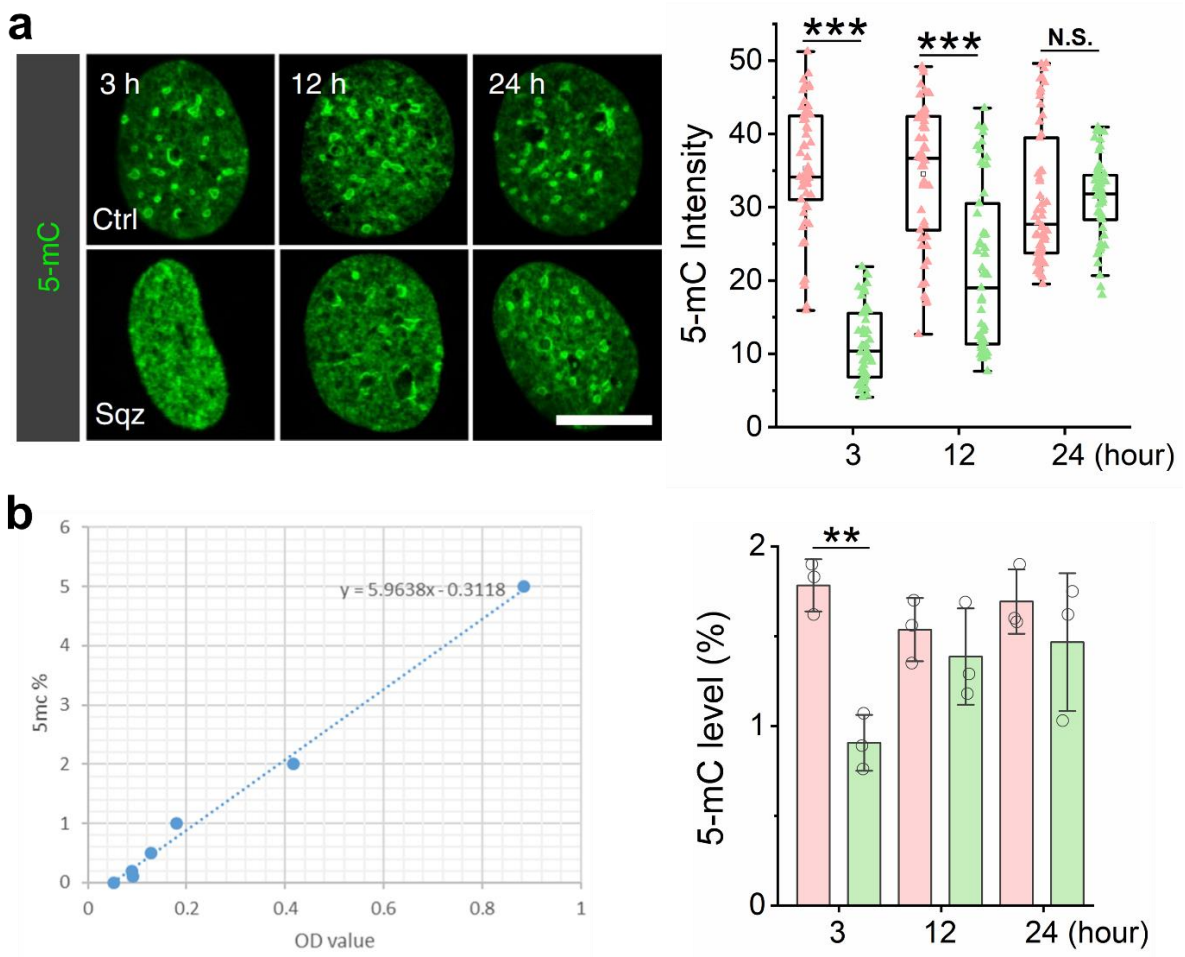

Fig. 2.10. Transient decrease of 5-mC level induced by nuclear deformation. (a) Representative images and quantification of 5-mC staining in control and squeezed cells at various time points. Scale bar, 10 μm. (b) Quantification of 5-mC level by MethylFlash Global DNA Methylation (5-mC) ELISA Easy Kit in control and squeezed cells at the indicated time points.

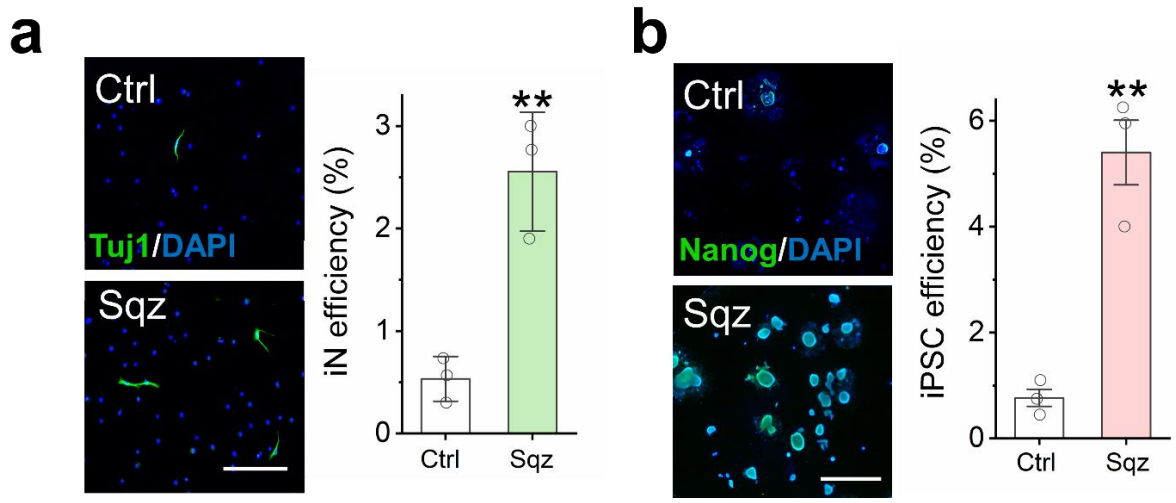

Fig. 2.11. Compatibility with various reprogramming models. (a) Immunofluorescent images showing Tuj1$^+$ iN cells reprogrammed from BAM-transduced mouse macrophages that were squeezed through 5-μm-wide microchannels compared to control group. Scale bar, 200 μm. Reprogramming efficiency of BAM-transduced macrophages after squeezing (n = 3). (b) Immunofluorescent images showing Nanog$^+$ colonies reprogrammed from OSKM-transduced mouse fibroblasts that were squeezed by 7-μm-wide microchannels compared to control group. Scale bar, 1 mm. Reprogramming efficiency of OSKM-transduced mouse fibroblasts into iPSCs after squeezing as determined by normalizing the number of Nanog$^+$ colonies to the number of cells initially seeded (n = 3).

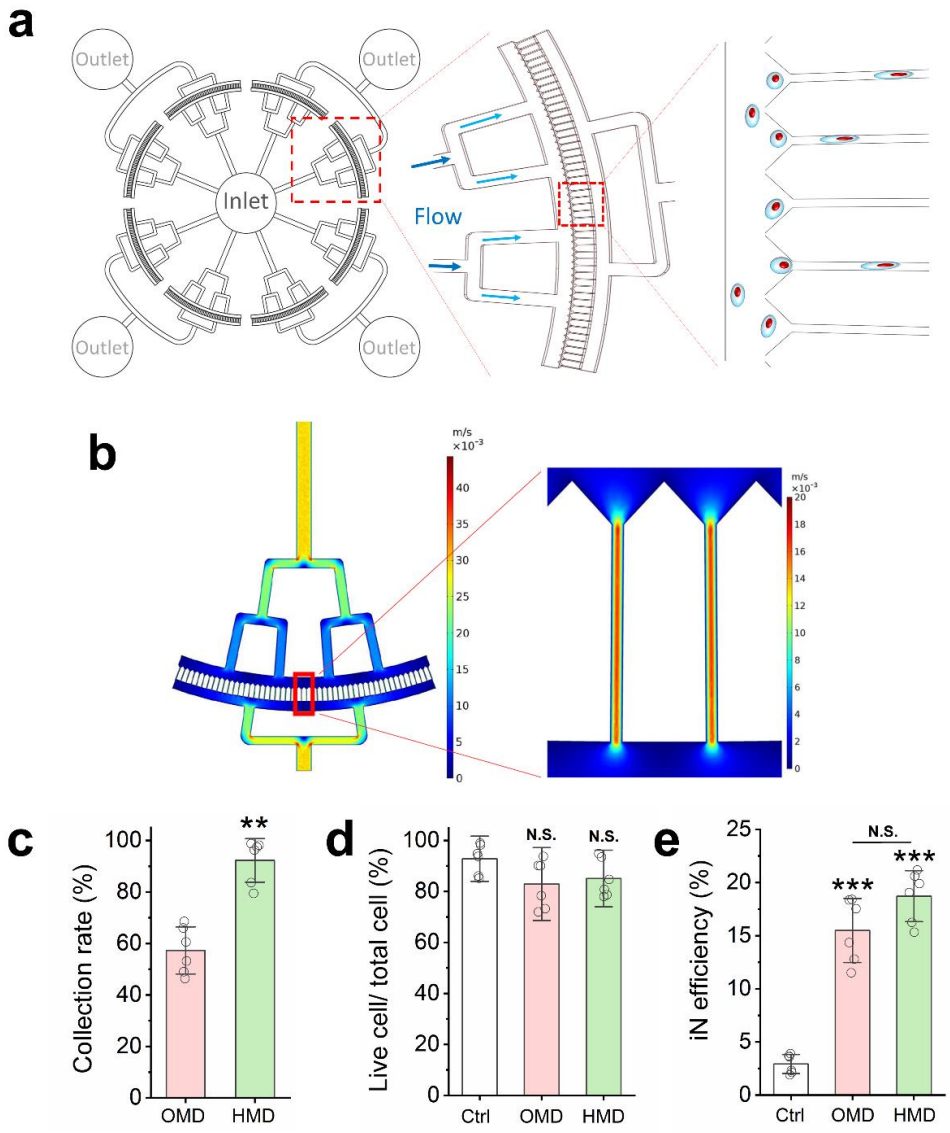

Fig. 2.12. Development of the high-throughput microfluidic device. (a) Schematic illustration of the design of the high-throughput device. (b) Simulation of flow velocity magnitude in the high throughput microfluidic device. (c) Quantification of the percentage of cells that were collected after passing through OMD or HMD (n = 6). (d) The percentage of live BAM-transduced fibroblasts after squeezing through OMD or HMD, compared to control group (n = 6). (e) iN reprogramming efficiency of BAM-transduced fibroblasts squeezed through OMD or HMD, compared to control group, on day 7 (n = 6).

Tables

Antibody	Vendor	Catalog #	Dilution
Tuj1	Biolegend	801202	1:1000 (IF)
H3K4me1	Abcam	ab32356	1:300 (IF)
H3K9me3	Abcam	ab8898	1:500 (IF)/ 1:1000 (WB)
H4K20me3	Abcam	ab4729	1:300 (IF)
H3K27me3	Abcam	ab192985	1:300 (IF)/ 1:1000 (WB)
AcH3	Millipore	06-599	1:300 (IF)/ 1:1000 (WB)
H3K9ac	Abcam	ab4441	1:300 (IF)
5-mC	Cell signaling	28692S	1:500 (IF)
Synapsin	Abcam	ab64581	1:100 (IF)
MAP-2	Sigma	M9942	1:200 (IF)
LaminA/C	Santa Cruz	sc-376248	1:50 (IF)
Histone H3	Abcam	ab1791	1:2000 (WB)
Nanog	Abcam	ab214549	1:300 (IF)

Table 2.1. Antibodies used for immunocytochemistry and Western blotting analysis.

Chapter III

Optimization of microfluidics device for cell squeezing

As discussed in chapter III, a constriction-based microfluidic device was developed to induce transient nuclear deformation by mechanically squeezing cells through microchannels (Fig. 3.1a), therefore enhancing the cell reprogramming efficiency by downregulating the level of H3K9me3 and DNA methylation. The results have shown that the increase in cell reprogramming efficiency was dependent on the size of the cells and geometry of the microchannel, as a 7-μm-wide channel and a 5-μm-wide channel was picked for cell reprogramming experiments with fibroblasts and macrophages respectively[1]. However, it remains unknown if these conditions are optimal for cell squeezing experiments or if there are other microchannels with different geometries which could further enhance the reprogramming efficiency. Since there are infinite possible designs of microchannels and it is costly and time-consuming for the microfabrication of microfluidics devices with various geometries, it is challenging to find the optimal condition with conventional enumeration method. To overcome this barrier, an artificial intelligence enabled parabolic response surface (PRS) is employed to optimize the microfluidics device geometric design with minimal requirement of experimental conditions. A general guideline for microfluidics device geometric design for cell reprogramming is proposed based on the optimization results. In addition, the effect of mechanical stimulation on cell reprogramming by defined hydrodynamic stretching with a different microfluidics system is compared to the constriction-based microfluidics device, which enables a defined deformation.

3.1 Response surface methodology and screening of dimension factors

Considering a system can be modeled as a response y dependent on multiple factors **x** = (x_1, x_2, … , x_k), with a relationship of

$$y = f(x_1, x_2, \dots, x_k) + \varepsilon$$

where the function f is unknown and ε is the error term which is not captured by f[2]. Response surface methodology[3] (RSM) is an attractive technique to estimate this function f, which involves experimentation, modeling, data analysis and optimization. The main idea of RSM is utilizing a series of strategically designed experiments to yield an optimal response. Generally, RSM involves identifying significant factors, searching for the optimum region. and employing a more complicated model to approximate the function f, a second-order polynomial model is typically used due to its easy estimation and application. A second-order polynomial model with factor **x** looks like

$$y = \beta_0 + \sum_{i=1}^{k} \beta_i x_i + \sum_{i=1}^{k} \beta_{ii} x_i^2 + \sum_{i=1<j\leq k} \beta_{ij}\, x_i x_j + \varepsilon$$

where β_0, β_i, β_{ii}, and β_{ij} are the intercept, linear, quadratic, and bilinear terms respectively, and ε is the error term. After solving this equation, a smooth PRS can be plotted to represent the system response dependent on factor **x**. This method is widely used in drug screening, to identify synergistic drug combinations to address various medical problems including treatment of cancer and infectious diseases, and suppression of rejection in liver transplantation[4-15]. RSM is also employed in the optimization of microfluidics-based applications, such as double emulsion droplet generation[16], therefore we want to investigate if this methodology could be employed to

optimize the geometric design of the microfluidics device, which is the critical of squeezing-induced nuclear deformation based on the previous results.

To optimize the microfluidics design, the same iN reprogramming model from mouse fibroblasts was employed. The resulted iN reprogramming efficiency after squeezing through the microchannels was used as the outcome (y), and the width of the microchannel was used as one of the factors (x_1) as the previous results have shown that the iN efficiency is dependent on the channel width. The channel height was chosen as the other factor (x_2) because it defined the microchannel geometry, together with the channel width. After determining the two significant factors used for this optimization, a factorial experimental design was used to uniformly covered the possible range of the two factors based on the previous results, which were channel width of 3 μm, 5 μm, 7 μm, 9 μm and channel height of 10 μm, 13 μm, 17 μm, 21 μm, respectively, resulting in 16 different combinations. The microfluidics devices of each condition were fabricated with standard photolithography and soft lithography techniques, for the following experiments.

3.2 Design screening based on cell viability

To have a direct view of the nuclear deformation, 3D imaging of living H2B-GFP mouse fibroblast was performed while the cell was passing through the microchannel (Fig. 3.1b). Based on the imaging results, the cell nucleus was compressed in two directions, along channel width and channel height, and elongated in the third direction, along channel length. Therefore, this nuclear deformation process could be modeled as a biaxial compression (Fig. 3.1c), and the

compression force was dependent on the geometric design of the cross-section of the microchannel.

Before performing the cell reprogramming experiments, the 16 designs of microfluidics devices were first screened based on the viability of cells after passing through the microchannels. Mouse fibroblasts were introduced to each individual microfluidics devices for squeezing, and were collected and cultured in 96-well plate for an hour, followed by a live-dead staining to test the cell viability after squeezing. The results showed that there was a significant cell death in mouse fibroblasts passing through the microchannels with geometry of 3 μm × 10 μm, 3 μm × 13 μm, 3 μm × 17 μm, 3 μm × 21 μm, 5 μm × 10 μm, and 5 μm × 13 μm (width × height), while the viability of cells passing through the other conditions stayed at a similarly high level compared to the control group, which was not squeezed (Fig. 3.2). Therefore, only the 10 of 16 channel designs, which didn't cause significant cell death, were used for the rest of cell reprogramming experiments, and these results indicated a threshold on the geometric design of the microchannel, which represents the degree of deformation, to keep majority of the cells alive after squeezing, which was set to be 70 μm^2 in cross-sectional area, for mouse fibroblasts. Additionally, it was found that with the similar cross-sectional area, the microchannel with a smaller width (3 × 21) induced a significantly higher ratio of cell death, compared to the microchannel with a larger width (5 × 13), indicating the deformation along one single axis was also critical in cell viability after squeezing. The results suggested that microchannels with a dimension smaller than 5 μm in one direction would induce a significant cell death.

3.3. Optimization of the geometric design

After screening based on the cell viability results, microchannel with 10 different geometries, 5 μm × 17 μm, 5 μm × 21 μm, 7 μm × 10 μm, 7 μm × 13 μm, 7 μm × 17 μm, and 7 μm × 21 μm, 9 μm × 10 μm, 9 μm × 13 μm, 9 μm × 17 μm, and 9 μm × 21 μm, were used to optimize the microfluidics device design. BAM-transduced mouse fibroblast squeezed through each different microchannel 6 hours after administration of Dox. The cells were then collected and seeded onto fibronectin-coated glass coverslips and cultured in serum-free N2B27 medium. Seven days later, cells were fixed and stained with Tuj1, the iN reprogramming efficiency was determined by the number of $Tuj1^+$ cells divided by the number of initially seeded cells. The results indicated a highest reprogramming efficiency with the microchannel geometry of 7 μm × 13 μm, and a parabolic profile of reprogramming efficiency was observed when microchannels had different heights with a same width (Fig. 3.3).

Additionally, a significant difference on the iN reprogramming efficiency was observed between channels with similar cross-sectional area but different width/height ratio (7 μm × 13 μm and 5 μm × 17 μm), or similar width/height ratio but different cross-sectional area (7 μm × 13 μm and 9 μm × 17 μm). Two dimensionless numbers were defined to better describe the geometry of the microchannel and generalize the optimization (Fig. 3.4), nuclear ratio (NR) was defined as the ratio of the cross-sectional area of the microchannel and the cross-sectional area of cell nucleus, while aspect ratio (AR) was defined as the ratio of the microchannel width and the microchannel height. By having these two dimensionless numbers, the overall degree of nuclear deformation can be described with NR and the bias of the nuclear deformation along two axes within the microchannel could be described with AR. The NR and AR of each geometry was calculated based on the average measured nuclear diameter (~ 11μm) of mouse fibroblasts (Table 3.1).

Based on the reprogramming results, a second-order regression was performed using MATLAB to generate the PRS (Fig. 3.5). The results predicted an optimal geometry of microchannel with NR ~ 0.98 and AR ~ 0.57 to achieve the highest reprogramming efficiency. This predicted geometry was very close to the geometry of 7 μm × 13 μm, suggesting that the nuclear deformation induced by a microchannel with a similar cross-sectional area compared to cell nucleus (NR = 1), but with an aspect ratio of 0.5 (AR = 0.5) which guided a specified nuclear deformation profile within the microchannel, could enhanced iN reprogramming most efficiently.

3.4. Validation on epigenetics changes and macrophage reprogramming

Previous results have shown that the enhancement in reprogramming efficiency after nuclear deformation was attributed to the downregulation on the methylation level of histone (H3K9me3) and DNA (5-mC), to investigate whether the methylation level remained the key factor in the variation of reprogramming efficiency with different channel geometries, mouse fibroblasts were squeezed through each individual condition and seeded on coverslips for three hours, followed by fixation and immunostaining of H3K9me3 (Fig. 3.6) and 5-mC (Fig. 3.7) markers respectively. The quantification of H3K9me3 showed an inverse-relationship according to the iN reprogramming results (a lower H3K9me3 level corresponded to a higher reprogramming efficiency), while only the cells squeezed through the microchannel with a geometry of 7 μm × 13 μm showed a significant decrease in DNA methylation level, which might contribute to the highest efficiency of this geometry. These findings indicated that the epigenetic changes after mechanical squeezing were dependent on the geometry of the microchannel. It also suggested that the histone and DNA methylation level were the key barriers

to cell reprogramming, and a dual-decrease in both H3K9me3 and 5-mC levels was required to achieve the highest reprogramming efficiency.

To investigate whether the design rule (NR = 1, AR = 0.5) could be applied to other cell types, mouse macrophages, instead of mouse fibroblasts, were used for iN reprogramming. Based on the measured nuclear diameter of mouse macrophages (average ~ 8 μm, Fig. 3.8), four geometries, 3 μm × 10 μm, 5 μm × 10 μm, 7 μm × 10 μm, 5 μm × 13 μm were selected for macrophage reprogramming experiments, and 5 μm × 10 μm, with NR ~ 1 and AR = 0.5, was predicted to be the optimal design. The experimental process was similar to iN reprogramming with fibroblasts, and the results showed an increase of the reprogramming efficiency after squeezing through microchannels, and 5 μm × 10 μm microchannel induced a biggest enhancement (Fig. 3.9), consistent with the prediction.

These findings suggested a general guideline for designing the microfluidics devices for enhancing cell reprogramming based on nuclear deformation. The optimal geometry of the microchannel was predicted to have NR = 1 and AR = 0.5, based on the nuclear size of the starting cells.

3.5 Cell deformation via hydrodynamic stretching

The previous nuclear deformation was induced by a constriction-based microfluidics devices, which had a defined geometry of microchannel, resulting in a determined degree of nuclear deformation. To study if a defined pressure, instead of defined deformation, would contribute similarly to cell reprogramming, a hydrodynamic stretching-based device was used to induce cell deformation. It was shown that this device could deform cells at high strain rate by

hydrodynamic stretching with a defined pressure dependent on flow rate, and a processing rate of approximately 2,000 cells per second[17].

This microfluidics device has two branches, and inertial focusing was employed to deliver cells uniformly to an extensional flow region where the cellular deformation occurred (Fig. 3.10). A uniform force was exerted on cells within the extensional flow region, which can be estimated with equation

$$F_D = 0.5\rho U^2 C_D A_P$$

Where ρ is the density of the fluid, U is the fluid velocity, C_D is the drag coefficient on the cell, and A_P is the cross-sectional area of the cell.

This force could be tuned by adjusting the flow rate, to achieve different strain on cellular deformation. The iN reprogramming model with mouse fibroblasts was employed to investigate the effect of hydrodynamic stretching-induced cellular deformation. Before starting the reprogramming experiment, the cell viability after hydrodynamic stretching was evaluated with different flow rates. The flow rates used for viability study started from 800 μL/min, because the flow rate below 800 μL/min could not trigger a noticeable cellular deformation, with an increment of 100 μL/min. The results showed that a noticeable cell death was observed after hydrodynamic stretching, and it became more significant starting with a flow rate of 1,100 μL/min (Fig. 3.11). Therefore, four different flow rates, 800 μL/min, 900 μL/min, 1,000 μL/min and 1,100 μL/min were selected for cell reprogramming experiments. Based on Tuj1 staining, a modest increase (about twofold) in iN reprogramming efficiency was observed with all four flow rates (Fig. 3.12). To investigate whether this increase was triggered by the modulation of the methylation level of histone and DNA, H3K9me3 and 5-mC staining was performed and

quantified. Interestingly, the results showed that there was no significant change on H3K9me3 and 5-mC level after hydrodynamic stretching (Fig. 3.13).

Compared to the constriction-based nuclear deformation, the cellular deformation induced by hydrodynamic stretching could only trigger a much lower enhancement on iN reprogramming, accompanied with no significant decrease on the global level of H3K9me3 and 5-mC. This might be attributed to the difference in the working mechanism of these two microfluidics systems. In constriction-based microfluidics device, the cells had a physical contact with the sidewall when squeezing through the microchannels with a dimension smaller than the nuclear diameter, this squeezing process will force the cell nucleus to deform to a defined degree, and the optimal condition (7 μm × 13 μm microchannel) could be modeled as a biaxial compression on cell nucleus. However, in hydrodynamic stretching-based microfluidics device, instead of defined deformation degree, a defined hydrodynamic pressure was applied on the cell body, and it could be modeled as a uniaxial compression instead. Additionally, the deformation timescale was different in these two microfluidics systems. In constriction-based microfluidics device, it took milliseconds for cells to passing through the microchannel while the cells were only exposed to the hydrodynamic pressure for microseconds in hydrodynamic stretching-based microfluidics device. Cell nucleus might need a significant time to respond to the external mechanical stimulation, this 1,000-fold difference on the deformation period might contribute to the difference in these two microfluidics systems.

3.6 Conclusion

We first demonstrated that the PRS methodology could be employed to optimize the geometric design of microfluidics device for nuclear deformation. This optimization process could help maximize the cell reprogramming efficiency while requiring minimal number of trials with different designs. The optimization results based on iN reprogramming model with mouse fibroblasts suggested an optimal design rule of microchannel geometry, with NR = 1 and AR =0.5, based on the cell nucleus size, which was validated with macrophage reprogramming. This rule provided a general guideline when designing the microfluidics device for different cells and could expand the applications of this constriction-based microfluidics device to various cell reprogramming models with different cell types, which could be further expanded in disease modeling, drug screening and cell therapy. In addition, this design rule could contribute to personalized medicine by designing the microfluidics device based on the nucleus size of the cells collected from the patient. Moreover, the comparison between constriction-based microfluidics system and hydrodynamic stretching-based microfluidics system suggested that a defined nuclear deformation induced by biaxial compression based on physical contact might be more effective on enhancing cell reprogramming, compared to a uniaxial compression on cell body induced by a defined hydrodynamic pressure, also a minimum duration of deformation might be required for cell nucleus to respond to the external mechanical stimulus. Further investigation is required to have a better understanding of the underlying mechanisms.

Methods

For other methods, refer to the methods section in Chapter II.

Hydrodynamic stretching device operation

Cells were prepared in suspension in Dulbecco's Modified Eagle Medium (DMEM) with a density between 200,000 and 500,000 cells/mL, and loaded into 10 mL plastic syringes. The syringe was loaded onto a PHD 2000 syringe pump (Harvard Apparatus) and set to inject at a flow rate between 800 μL/min to 1,100 μL/min. After the injection was initiated, imaging was delayed a further 20 s to account for fluidic capacitance. Cells migrated across fluid streamlines to the center of the channel due to inertial lift forces. At the junction, an extensional flow was generated. The cell could be stretched when it reached the center of the extensional flow. Cells in flow were monitored with a 10× objective (Nikon Japan 10x/0.30) on a Nikon Eclipse Ti inverted microscope. A digital high-speed video camera, Phantom v7.3 (Vision Research, Inc.), was connected to the microscope via a c-mount for image capture. Camera settings were controlled with Phantom Camera Control (Vision Research, Inc.). The frame rate of the camera was set as 110,000 frames per second.

3D live imaging

In 3D cell image acquisition, we used an epi-fluorescence microscope (IX83, Olympus) as the front-end optics and excited the sample with a pulsed laser source (SuperK FIANIUM, FIU-15, NKT Photonics). The emitted fluorescence was collected by a microscope objective lens (UPLXAPO60XO, Olympus), and an intermediate fluorescence image was formed at the side image port of the microscope. The detection optics was based on light-field tomography[18, 19]. We used customized plano-convex cylindrical lenslets (diameter of 2 mm and a focal length of 4 mm) to obtain projections among different views. The cylindrical lenslets were rotated to different angles that were approximately uniform in the range of [0°, 180°]. We used a camera (CS2100M-USB, Thorlabs) located at the focal plane of the lenslets to acquire the projection

data at the lenslet rotation angles and constructed the sinogram. In 3D cell image reconstruction, we solved the optimization problem using the iterative method[19], computationally refocused the image to different depths, and reconstructed the 3D cell image. In 3D cell image rendering, the volumetric image was normalized and soft-thresholded to improve visibility.

References

1. Song, Y., et al., Transient nuclear deformation primes epigenetic state and promotes cell reprogramming. Nat Mater, 2022. 21(10): p. 1191-1199.

2. Fan, J. and J. Pan, Contemporary Experimental Design, Multivariate Analysis and Data Mining. 2020: Springer.

3. Box, G.E.P. and K.B. Wilson, On the Experimental Attainment of Optimum Conditions. Journal of the Royal Statistical Society Series B-Statistical Methodology, 1951. 13(1): p. 1-45.

4. Ding, X., et al., Cascade search for HSV-1 combinatorial drugs with high antiviral efficacy and low toxicity. Int J Nanomedicine, 2012. 7: p. 2281-92.

5. Weiss, A., et al., A streamlined search technology for identification of synergistic drug combinations. Sci Rep, 2015. 5: p. 14508.

6. Wang, H., et al., Mechanism-independent optimization of combinatorial nanodiamond and unmodified drug delivery using a phenotypically driven platform technology. ACS Nano, 2015. 9(3): p. 3332-44.

7. Nowak-Sliwinska, P., et al., Optimization of drug combinations using Feedback System Control. Nat Protoc, 2016. 11(2): p. 302-15.

8. Mohd Abdul Rashid, M.B., et al., Identification and Optimization of Combinatorial Glucose Metabolism Inhibitors in Hepatocellular Carcinomas. J Lab Autom, 2015. 20(4): p. 423-37.

9. Weiss, A., et al., Rapid optimization of drug combinations for the optimal angiostatic treatment of cancer. Angiogenesis, 2015. 18(3): p. 233-44.

10. Chen, Y.T., et al., A UV-sensitive hydrogel based combinatory drug delivery chip (UV gel-Drug Chip) for cancer cocktail drug screening. Rsc Advances, 2016. 6(50): p. 44425-44434.

11. Liu, Q., et al., Preclinical optimization of a broad-spectrum anti-bladder cancer tri-drug regimen via the Feedback System Control (FSC) platform. Sci Rep, 2015. 5: p. 11464.

12. Rashid, M., et al., Optimizing drug combinations against multiple myeloma using a quadratic phenotypic optimization platform (QPOP). Sci Transl Med, 2018. 10(453).

13. Lee, D.K., et al., Optimizing Combination Therapy for Acute Lymphoblastic Leukemia Using a Phenotypic Personalized Medicine Digital Health Platform: Retrospective Optimization Individualizes Patient Regimens to Maximize Efficacy and Safety. SLAS Technol, 2017. 22(3): p. 276-288.

14. Ding, X., et al., Effective drug combination for Caenorhabditis elegans nematodes discovered by output-driven feedback system control technique. Sci Adv, 2017. 3(10): p. eaao1254.

15. Zarrinpar, A., et al., Individualizing liver transplant immunosuppression using a phenotypic personalized medicine platform. Sci Transl Med, 2016. 8(333): p. 333ra49.

16. Sattari, A., et al., Numerical study of double emulsion droplet generation in a dual-coaxial microfluidic device using response surface methodology. Chemical Engineering and Processing-Process Intensification, 2021. 162.

17. Gossett, D.R., et al., Hydrodynamic stretching of single cells for large population mechanical phenotyping. Proc Natl Acad Sci U S A, 2012. 109(20): p. 7630-5.

18. Feng, X. and L. Gao, Ultrafast light field tomography for snapshot transient and non-line-of-sight imaging. Nat Commun, 2021. 12(1): p. 2179.

19. Feng, X., Y. Ma, and L. Gao, Compact light field photography towards versatile three-dimensional vision. Nat Commun, 2022. 13(1): p. 3333.

Figures

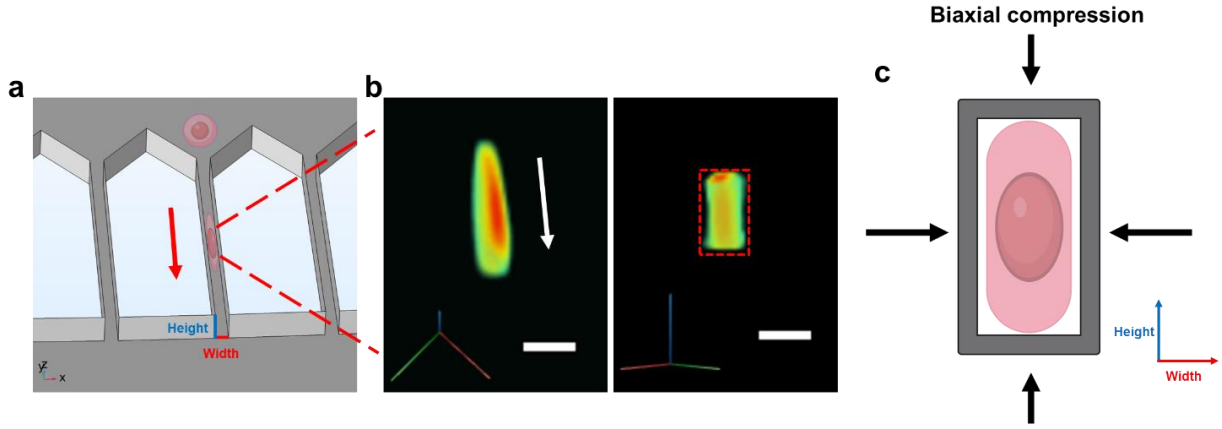

Fig. 3.1. Nuclear deformation within the microchannel. (a) A schematic view of cell being squeezed through the microchannel. The red arrow indicates the moving direction of the cell. (b) 3D imaging of deformed cell nucleus from different angles while H2B-GFP fibroblast was passing through the microchannel (7 μm × 13 μm). Red color indicates a stronger fluorescence signal of H2B and green indicates a lower fluorescence signal. The white arrow indicates the moving direction of the cell. The red dashed rectangular box indicates the cross-section of the microchannel. Scale bar, 10 μm. (c) Biaxial compression model describing the squeezing process.

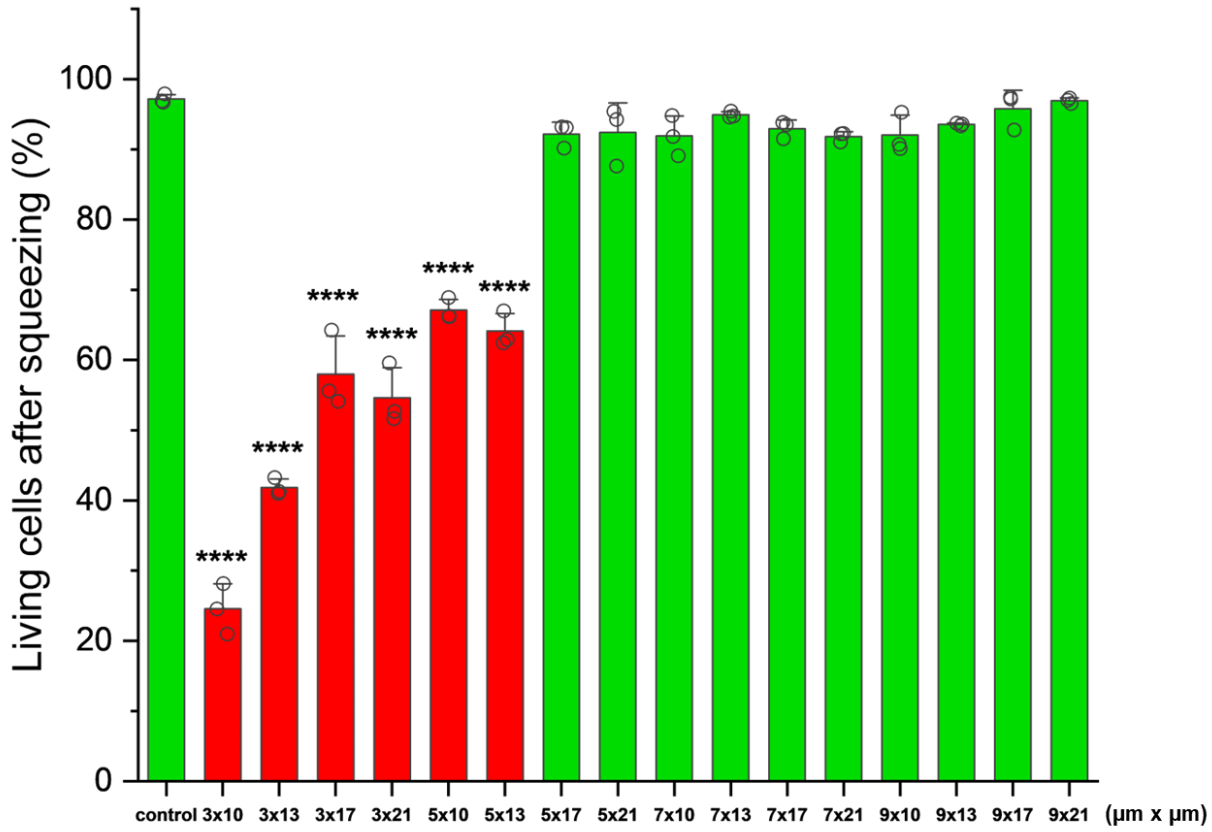

Fig. 3.2. Cell viability after squeezing. The percentage of live cells (determined by LIVE/DEAD staining) one hour after fibroblasts were deformed through microchannels with various channel widths (n = 3). Statistical significance was determined by a one-way ANOVA and Tukey's multiple comparison test.

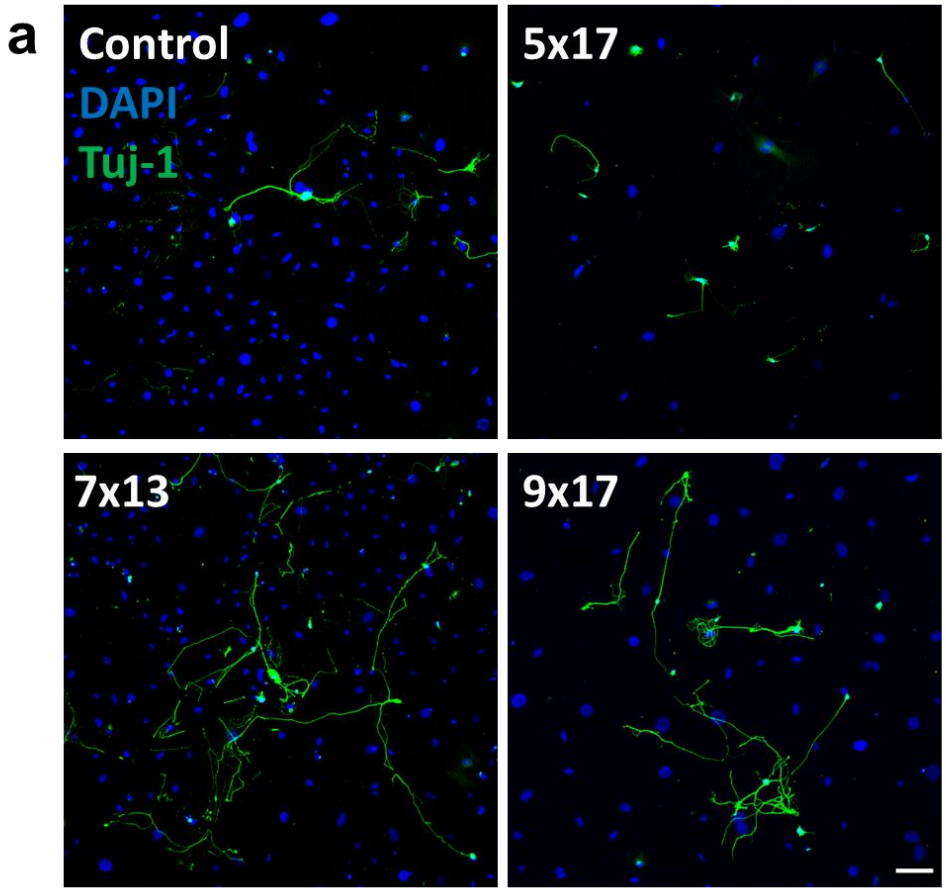
a
Control
DAPI
Tuj-1
5x17
7x13
9x17

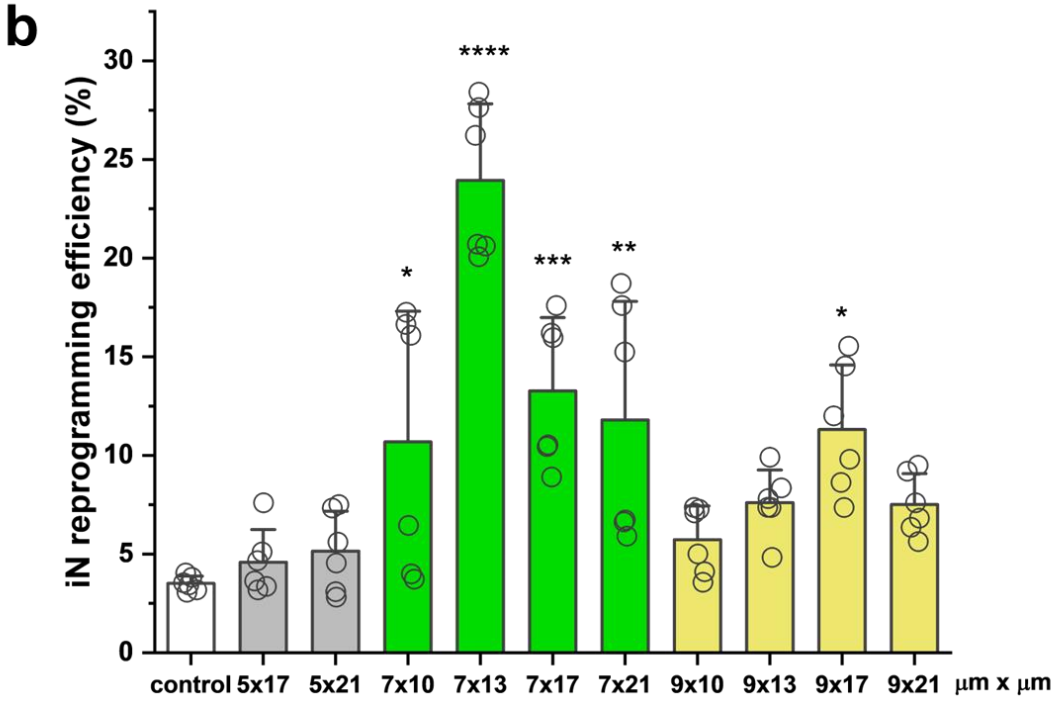
b
iN reprogramming efficiency (%)
0
5
10
15
20
25
30
****
*
***
**
*
control
5x17
5x21
7x10
7x13
7x17
7x21
9x10
9x13
9x17
9x21
μm x μm

Fig. 3.3. iN reprogramming results after squeezing. (a) Representative immunostaining images of $Tuj1^+$ cells (reprogrammed from fibroblast) on day 14 after nuclear deformation with selected geometries. Scale bar, 100 μm. (b) Effect of microchannel geometry on iN reprogramming efficiency on day 7 based on Tuj1 staining (n = 6).

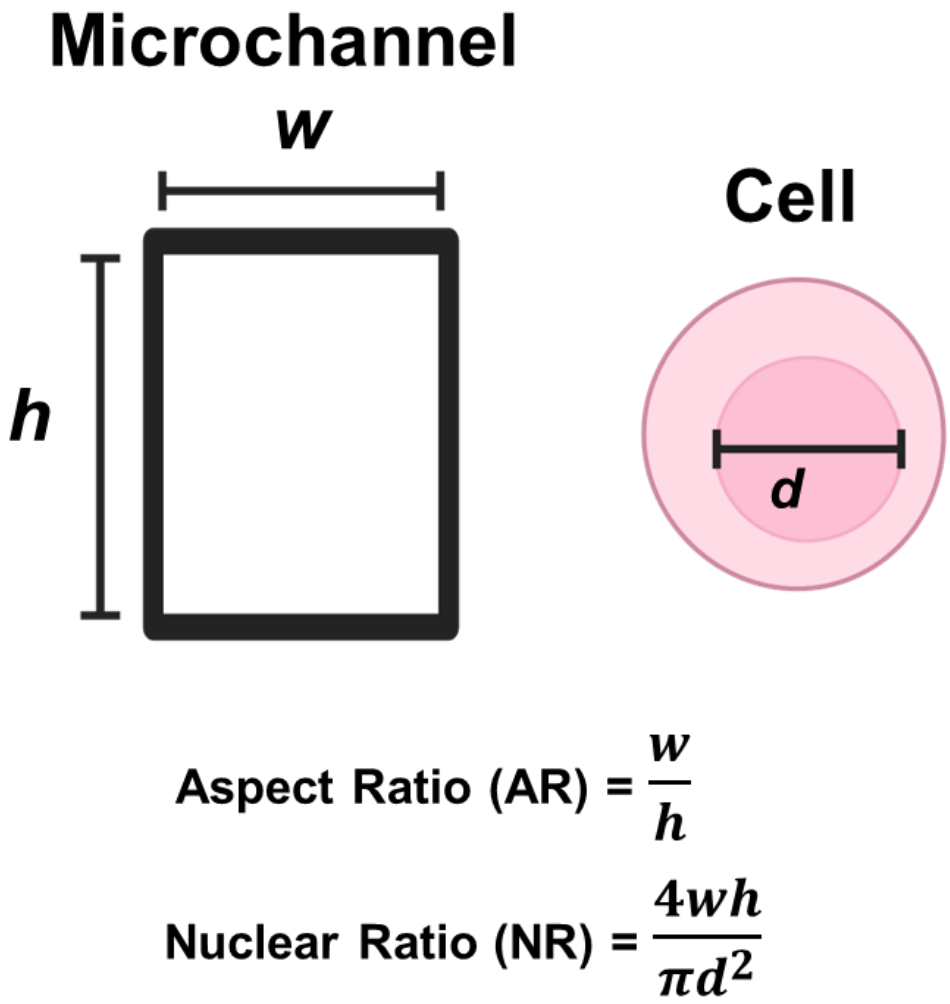

Fig. 3.4. Definition of aspect ratio and nuclear ratio. Aspect ratio is defined as channel width divided by channel height, and nuclear ratio is defined as cross-sectional area of the microchannel divided by the cross-sectional area of cell nucleus.

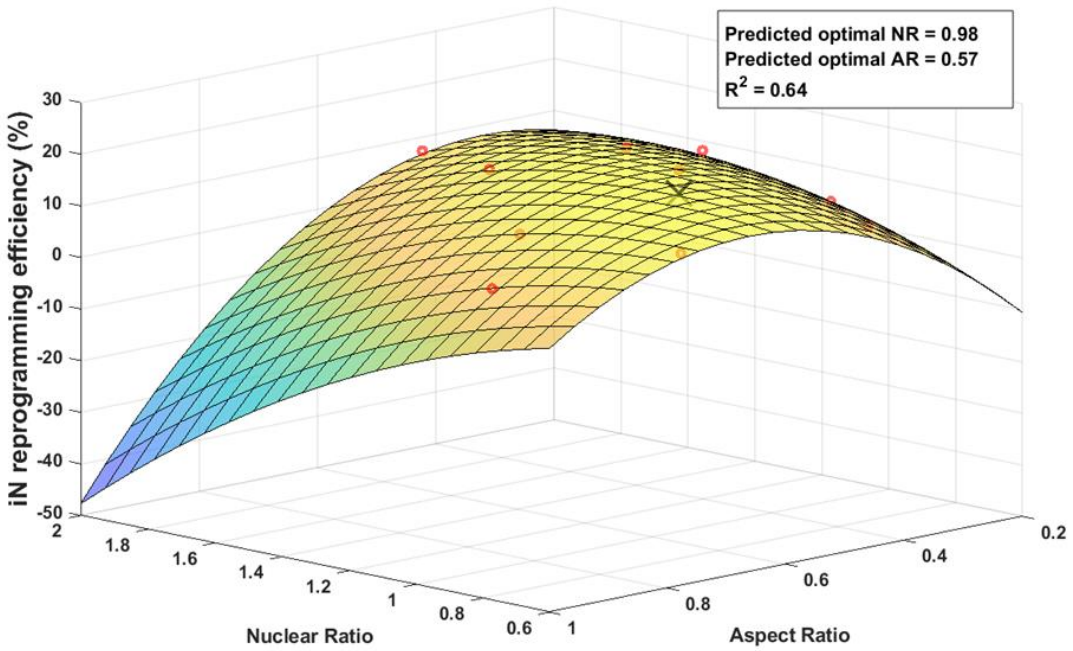

Fig. 3.5. Optimization results. PRS generated based on the iN reprogramming efficiency on day 7. Red circles represent the raw data, and the black cross represents the predicted optimal condition. R2 = 0.64.

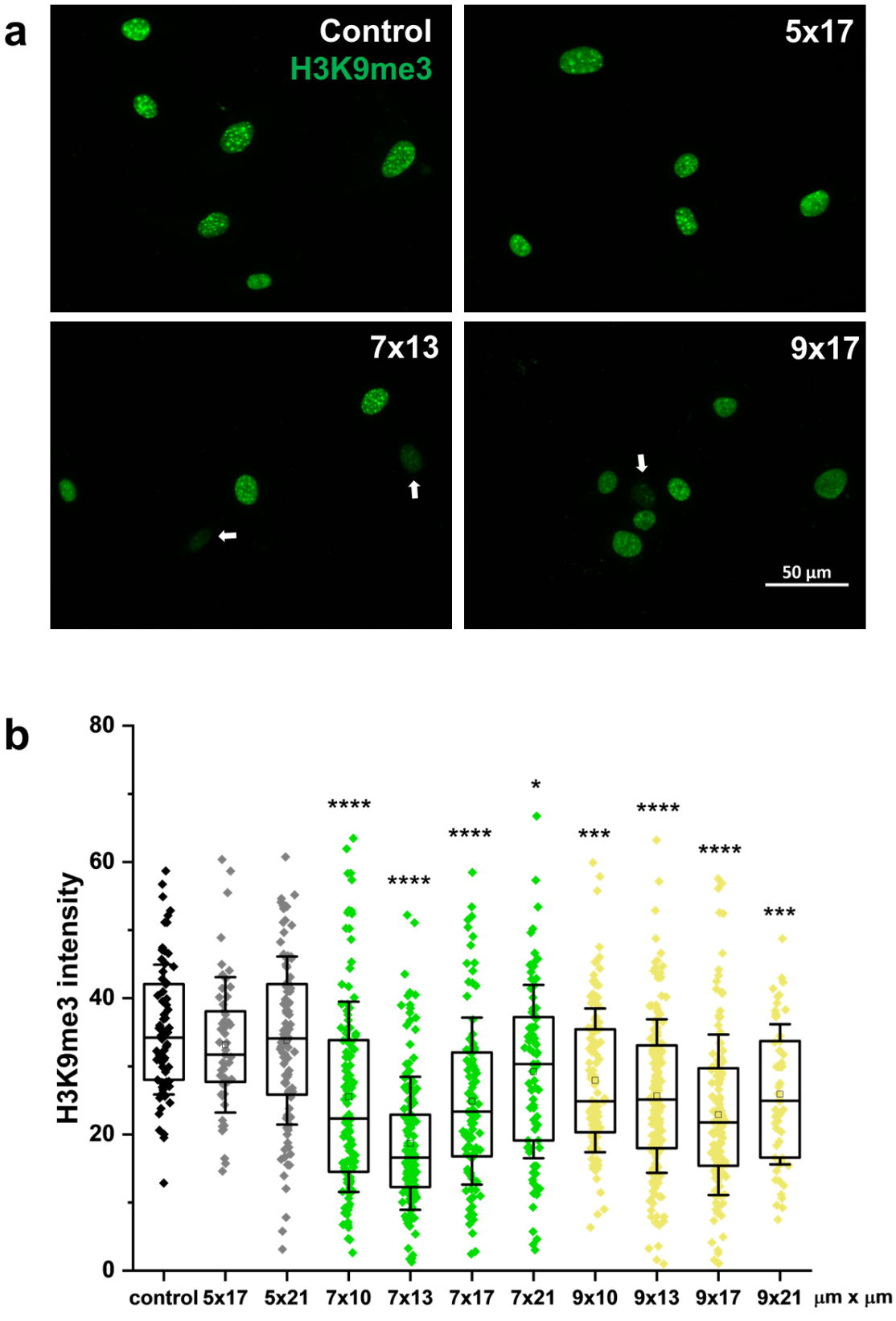
a
Control
H3K9me3
5x17
7x13
9x17
50 µm
b
H3K9me3 intensity
0
20
40
60
80
control
5x17
5x21
7x10
7x13
7x17
7x21
9x10
9x13
9x17
9x21
µm x µm
****
****
****
*
***
****
****
***

Fig. 3.6. H3K9me3 changes after squeezing. (a) Representative images of H3K9me3 staining of squeezed mouse fibroblasts 3 hours after nuclear deformation, with selected geometries. White arrow indicates the cells with decreased H3K9me3 level. Scale bar, 50 μm. (b) Quantification of H3K9me3 intensity in control and squeezed groups 3 hours after squeezing (based on experiments in a; $n > 50$). Statistical significance was determined by a one-way ANOVA and Tukey's multiple comparison test.

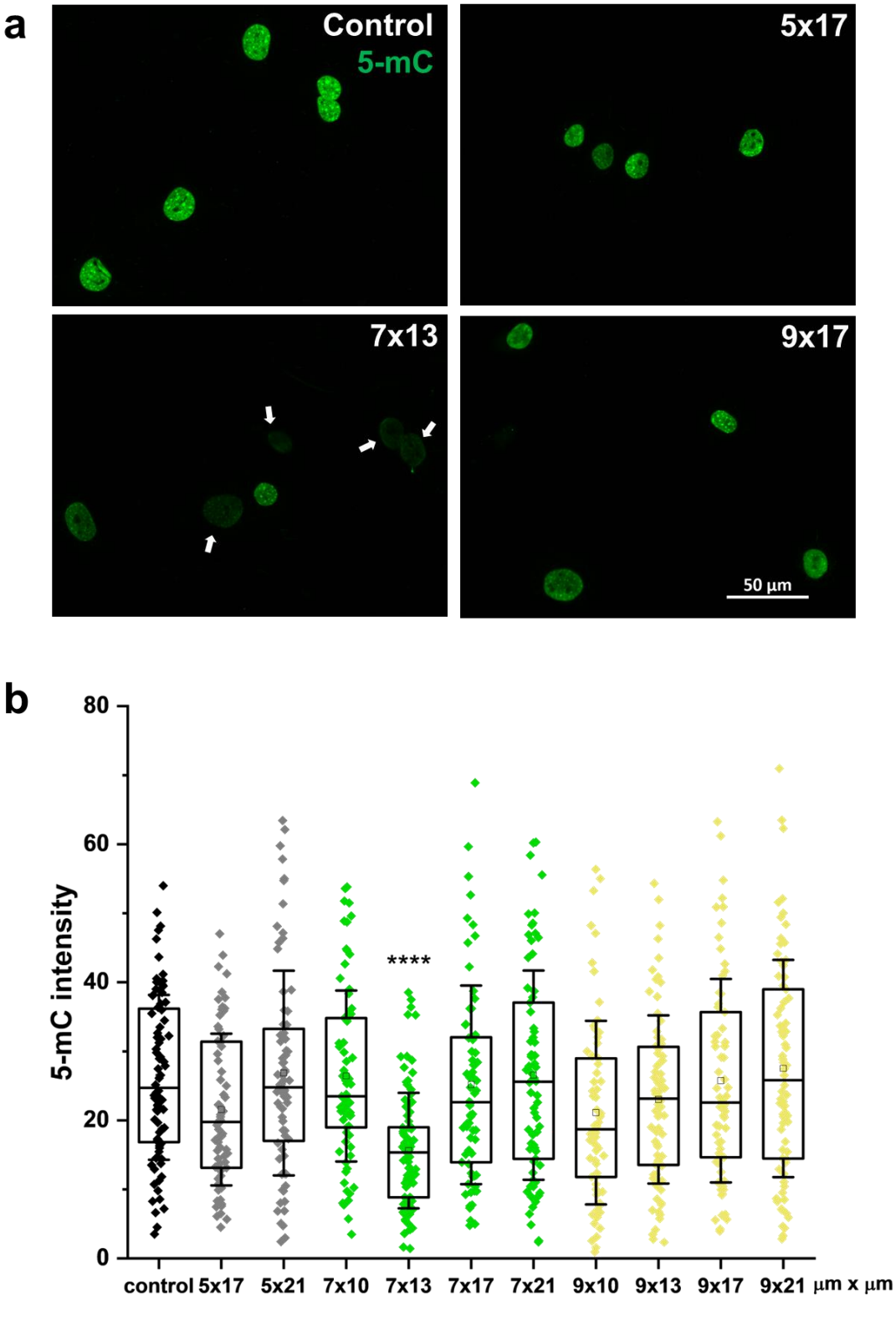
a
Control
5-mC
5x17
7x13
9x17
50 µm
b
5-mC intensity
80
60
40
20
0
****
control
5x17
5x21
7x10
7x13
7x17
7x21
9x10
9x13
9x17
9x21
µm x µm

Fig. 3.7. 5-mC changes after squeezing. (a) Representative images 5-mC staining of squeezed mouse fibroblasts 3 hours after nuclear deformation, with selected geometries. White arrow indicates the cells with decreased 5-mC level. Scale bar, 50 μm. (b) Quantification of 5-mC intensity in control and squeezed groups 3 hours after squeezing (based on experiments in a; $n > 65$). Statistical significance was determined by a one-way ANOVA and Tukey's multiple comparison test.

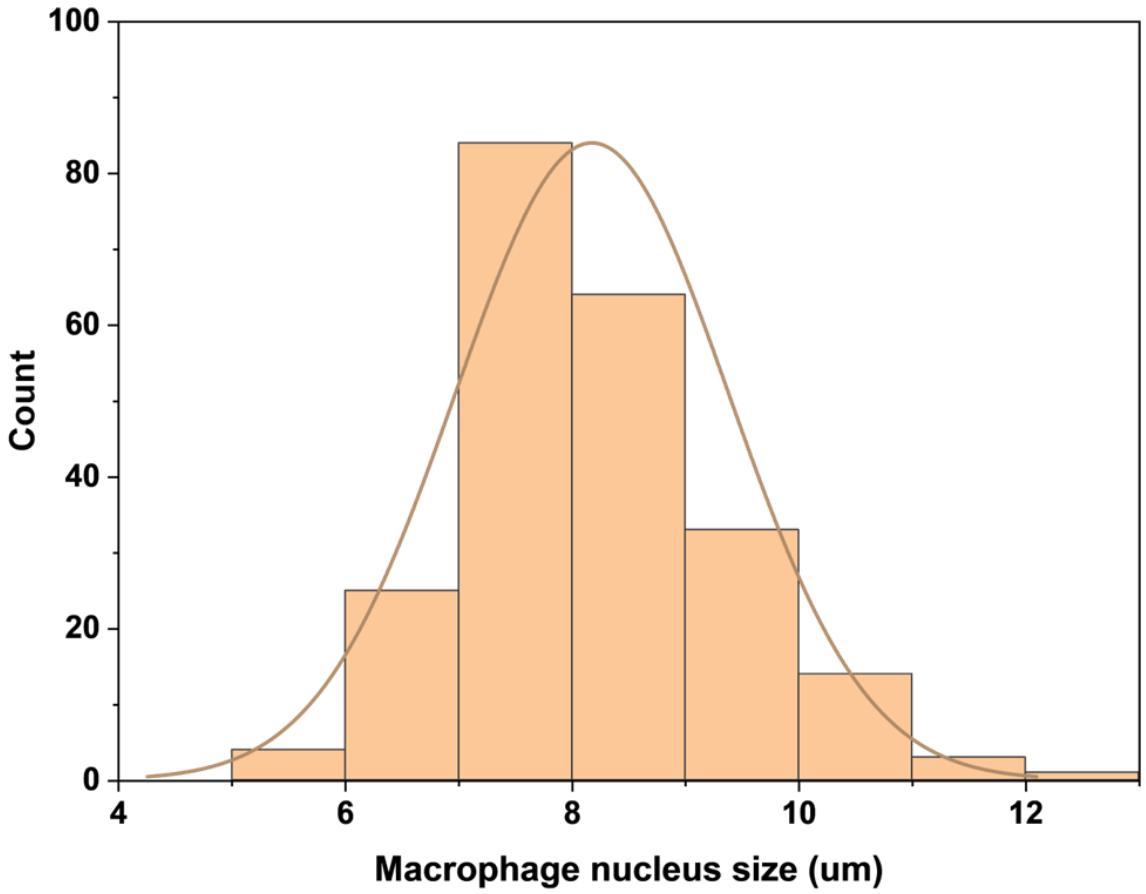

Fig. 3.8. Nucleus size of mouse macrophage. Quantification of mouse macrophage nuclear diameter based on Hoechst staining (n = 228).

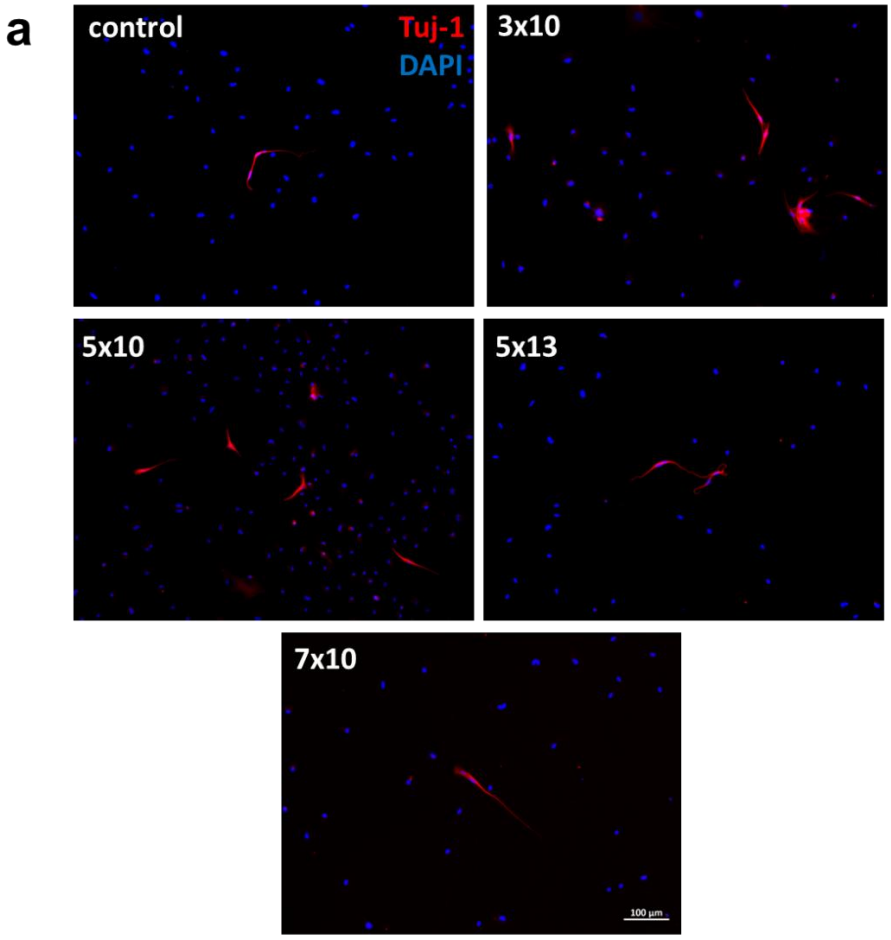
a
control
Tuj-1
DAPI
3x10
5x10
5x13
7x10
100 µm
b
Macrophage to iN reprogramming efficiency (%)
0
2
4
6
8
10
**
****
**
control
3x10
5x10
7x10
5x13
µm x µm

Fig. 3.9. Reprogramming of mouse macrophage into iN. (a) Representative immunostaining images of $Tuj1^+$ cells (reprogrammed from macrophage) on day 10 after nuclear deformation with various geometries. Scale bar, 100 μm. (b) Effect of microchannel geometry on iN reprogramming (from macrophage) efficiency on day 10 based on Tuj1 staining (n = 3).

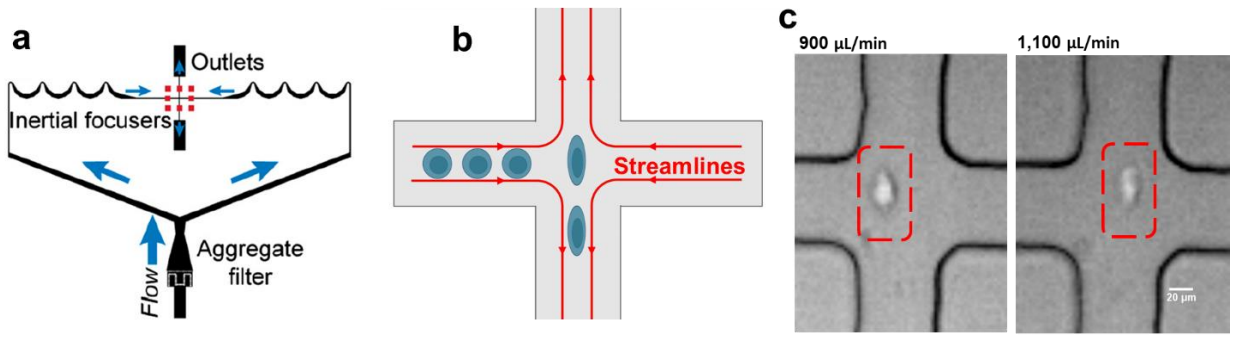

Fig. 3.10. Cellular deformation induced by hydrodynamic stretching. (a) A schematic view of the microfluidic device for hydrodynamic stretching[17]. (b) A schematic view of the cellular deformation in the center of an extensional flow. (c) Representative high-speed microscopic images showing a deformed cell within the extensional flow region with various flow rates. Scale bar, 20 μm.

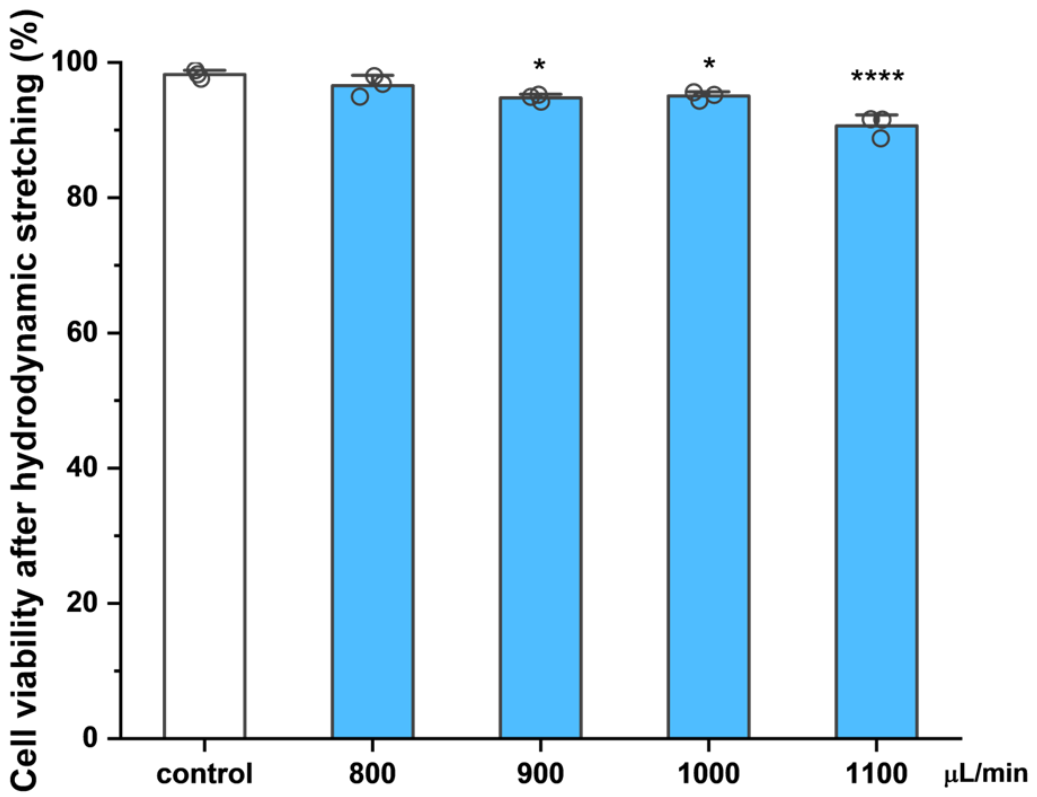

Fig. 3.11. Cell viability after hydrodynamic stretching. The percentage of live cells (determined by LIVE/DEAD staining) one hour after fibroblasts were deformed by hydrodynamic stretching with various flow rates (n = 3). Statistical significance was determined by a one-way ANOVA and Tukey's multiple comparison test.

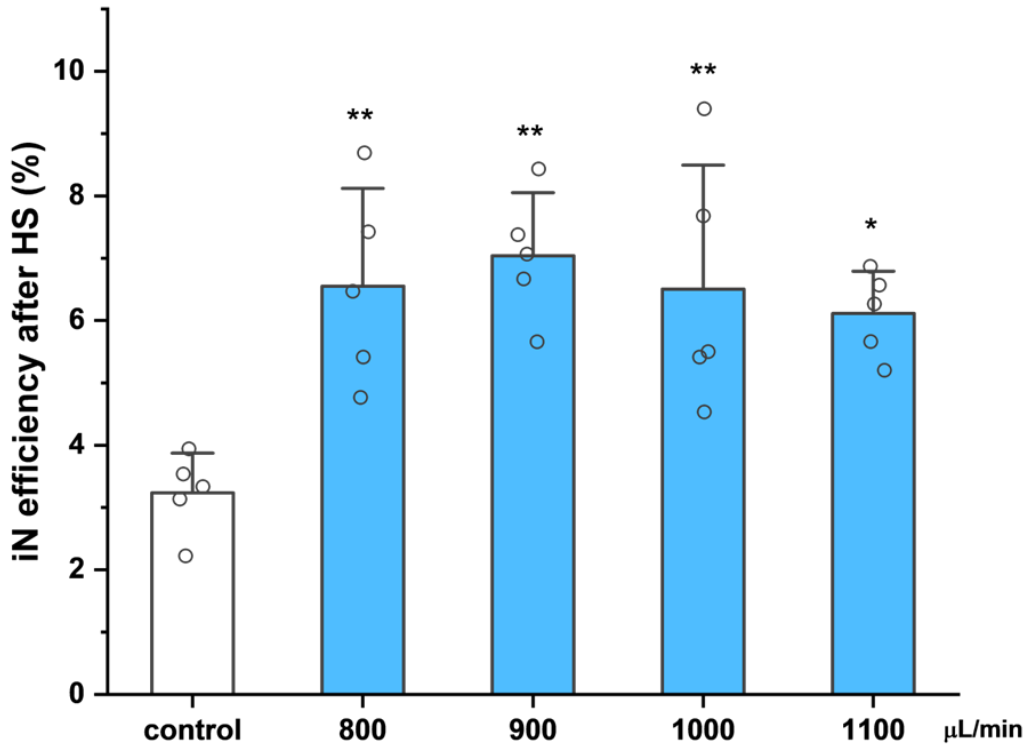

Fig. 3.12. iN reprogramming efficiency after hydrodynamic stretching. Effect of flow rates on iN reprogramming (from mouse fibroblast) efficiency at day 7 based on Tuj1 staining (n = 5).

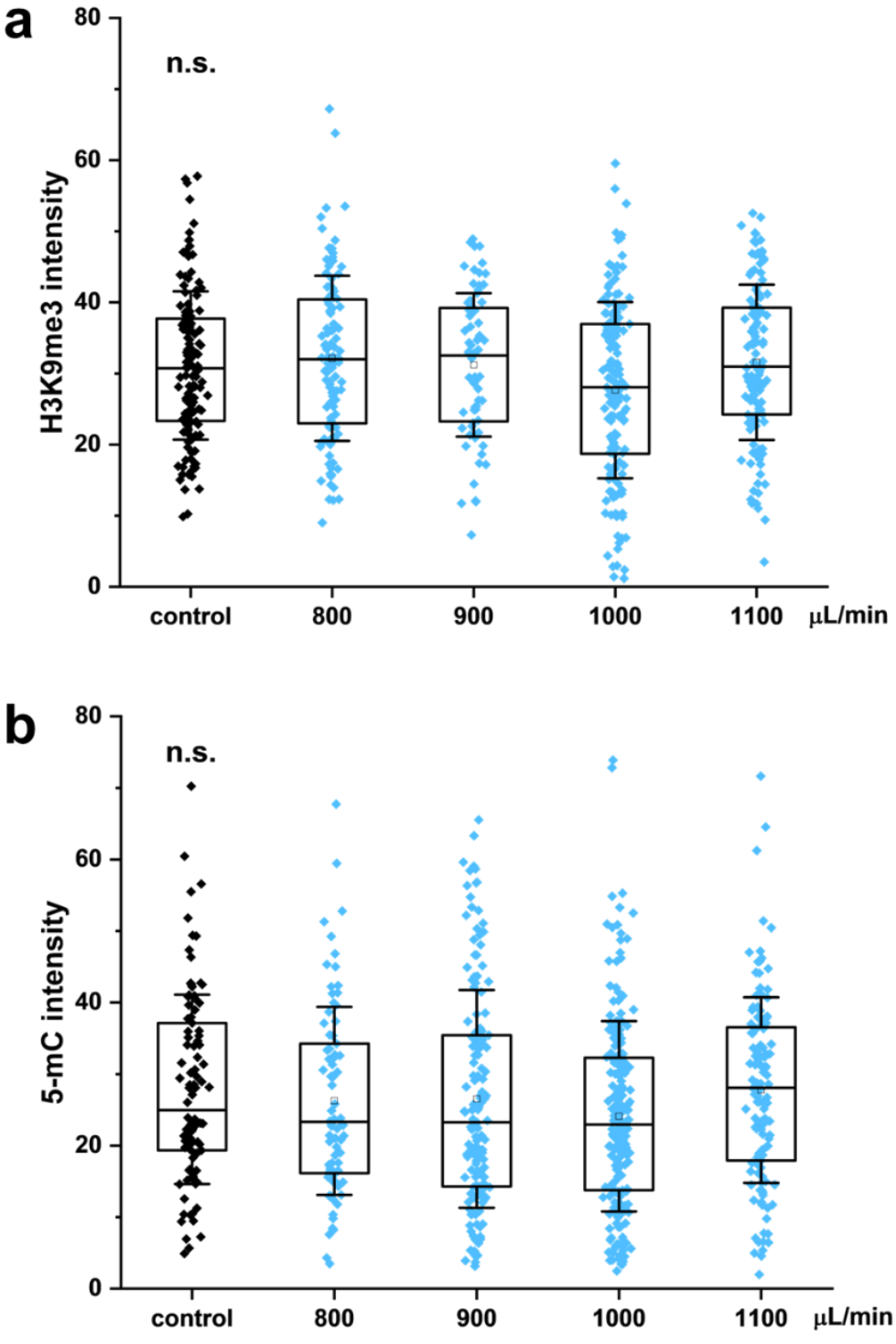
a
n.s.
H3K9me3 intensity
0
20
40
60
80
control
800
900
1000
1100
μL/min
b
n.s.
5-mC intensity
0
20
40
60
80
control
800
900
1000
1100
μL/min

Fig. 3.13. Epigenetics changes after hydrodynamic stretching. (a) Quantification of H3K9me3 intensity in control and hydrodynamic stretched fibroblasts 3 hours after squeezing (based on immunostaining images; n > 70). Statistical significance was determined by a one-way ANOVA and Tukey's multiple comparison test. n.s., not significant. (b) Quantification of 5-mC intensity in control and hydrodynamic stretched fibroblasts 3 hours after squeezing (based on immunostaining images; n > 78). Statistical significance was determined by a one-way ANOVA and Tukey's multiple comparison test. n.s., not significant.

Tables

Microchannel geometry (width x height)	NR	AR
5 x 17	0.895	0.294
5 x 21	1.105	0.238
7 x 10	0.737	0.7
7 x 13	0.958	0.538
7 x17	1.253	0.412
7 x 21	1.548	0.333
9 x 10	0.948	0.9
9 x 13	1.232	0.692
9 x17	1.611	0.529
9 x 21	1.990	0.429

Table 3.1. Calculated NR and AR based on fibroblast nuclear diameter for each geometry.

Chapter IV

Conclusion and future directions

My thesis focuses on addressing the problem of low cell reprogramming efficiency with an engineering approach. By harnessing the power of microfluidics, an innovative way is proposed to achieve a significantly higher cell reprogramming efficiency by squeezing cells through defined constrictions. Furthermore, parabolic response surface (PRS) is employed to optimize the design of microfluidics devices for different cell types in a more efficient way, which further expands the applications of this approach.

As discussed in Chapter 2, a novel microfluidics device consisting of microchannels with specific geometric design is developed to induce a well-controlled deformation on cell nucleus in a high throughput manner. This mechanical stimulation on cell nucleus can promote the reprogramming of mouse fibroblasts into induced neuronal cells significantly through its unique mechanism, by transient downregulation of H3K9me3 level and 5-mC level, assisting to overcome the epigenetic barriers. Compared to other approaches with biochemical cues (treatment with inhibitors), this mechanical squeezing has unique advantages with little induced DNA damage[1]. Compared to conventional mechanical approaches (e.g., tuning of substrate stiffness, topography-based cell deformation), this microfluidics-based approach provides a better control on the mechanical stimulation and studies the effect of nuclear deformation directly by removing various confounding factors (e.g., focal adhesions) in adherent cells.

Based on the existing findings, it remains a lot to explore, to further optimize and unleash the full potential of this microfluidics system. First, after a period of time usage, this constriction-based cell squeezing might cause potential clogging at the entrance of the microchannels, which will

disturb the pressure distribution within the microfluidics device and lower the overall throughput. A better design of the microfluidics device or a better protocol with pretreatment of lubricants should be developed to solve the clogging issue. Second, we can combine this mechanical squeezing with other biochemical approaches[2], to investigate if this could further increase the reprogramming efficiency. Moreover, the iN reprogramming model used in this study depends on viral transduction, a further explore on the compatibility of this device with other reprogramming models based on mRNA[3] or CRISPR/Cas9[4] could potentially further expand its applications. Lastly, it has been shown that there is a transient global decrease on H3K9me3 and 5-mC level, sequencing techniques, such as Assay for Transposase-Accessible Chromatin using sequencing (ATAC-seq)[5], could be employed to profile the chromatin accessibility throughout the genome after squeezing, providing a better understanding of the underlying mechanisms.

Following the development of the prototype of the microfluidics device, a second-order quadratic model and PRS is constructed to optimize the microfluidic device design. This optimization finds the optimal geometric design of the microchannel to achieve the highest reprogramming efficiency from mouse fibroblasts to induced neurons, in a more efficient and less costly approach by getting rid of laborious enumeration experiments. Additionally, a general guideline for designing microfluidics devices for different types of cells is provided, based on two dimensionless numbers nuclear ratio and aspect ratio which are defined by the geometric factor of the cells and microchannels. The design rule facilitates the expansion of the application of this microfluidics device to other reprogramming models with different starting cell types. In addition, the effect of cellular deformation induced by hydrodynamic stretching is compared with this nuclear deformation induced by squeezing, suggesting that a defined deformation on cell

nucleus induced by biaxial compression via physical constriction and a minimum requirement of straining time might be required to trigger the enhancement on cell reprogramming.

To further improve the optimization process, more factors can be brought in such as flow rate or transit time of cells passing through the microchannels. However, this will cause a factorial growth in the number of required experimental conditions. This could be alleviated by using an orthogonal array composite design (OACD)[6-8] to minimize the number of required testing conditions. Also, the suggested design rule was only validated with mouse fibroblasts and mouse macrophages, further studies with different cell types are necessary for verification.

In conclusion, this microfluidics system provides a high-throughput platform for cell engineering and enables a significant enhancement on cell reprogramming through its distinct mechanism. Its adaptability extends beyond a single cell type, demonstrating compatibility with diverse reprogramming models including various starting and target cell types. The impressive efficiency and broad versatility of this microfluidics system will contribute to the ongoing advancements in cell reprogramming and could have significant implications for cell therapies and regenerative medicine.

References

1. Song, Y., et al., Transient nuclear deformation primes epigenetic state and promotes cell reprogramming. Nat Mater, 2022. 21(10): p. 1191-1199.

2. Huangfu, D., et al., Induction of pluripotent stem cells by defined factors is greatly improved by small-molecule compounds. Nat Biotechnol, 2008. 26(7): p. 795-7.

3. Warren, L. and C. Lin, mRNA-Based Genetic Reprogramming. Mol Ther, 2019. 27(4): p. 729-734.

4. Chakraborty, S., et al., A CRISPR/Cas9-based system for reprogramming cell lineage specification. Stem Cell Reports, 2014. 3(6): p. 940-7.

5. Liu, C., et al., An ATAC-seq atlas of chromatin accessibility in mouse tissues. Sci Data, 2019. 6(1): p. 65.

6. Jia, X., et al., Application of sequential factorial design and orthogonal array composite design (OACD) to study combination of 5 prostate cancer drugs. Comput Biol Chem, 2017. 67: p. 234-243.

7. Jaynes, J., et al., Use of Orthogonal Array Composite Designs to Study Lipid Accumulation in a Cell-Free System. Quality and Reliability Engineering International, 2016. 32(5): p. 1965-1974.

8. Fan, J. and J. Pan, Contemporary Experimental Design, Multivariate Analysis and Data Mining. 2020: Springer.

Appendix

Changes on mechanical properties of cells during reprogramming

Previous results have shown that biophysical cues contribute to cell reprogramming[1, 2] but the role of mechanotransduction through intracellular structures, such as cytoskeleton, during reprogramming is poorly understood. A better understanding of the role of cytoskeleton during cell reprogramming may lead to novel engineering approaches for cell reprogramming.

Results

To study this, a direct reprogramming model converting fibroblasts into induced neuronal (iN) cells was employed[3]. Primary fibroblasts isolated from adult mice were transduced with doxycycline (Dox)-inducible lentiviral vectors encoding three key reprogramming factors, *Brn2*, *Ascl1*, and *Myt1l* (BAM), and seeded onto tissue culture polystyrene dishes coated with laminin. After one day culture, dox was added (marked as day 0) to initiate the expression of the transgenes and cells were cultured in neuronal medium (i.e., N3 medium) from day 1 to the conclusion of the experiment (Fig. A1).

To investigate how the actin cytoskeleton was altered during the early phase of iN reprogramming, immunostaining of actin was performed, and the results showed that by day 1 of the reprogramming process, actin assembled into a network with a cage-like structure around the nucleus, but this structure along with most of the cytoskeleton gradually disappeared by day 3 (Fig. A2). To study if these structural changes resulted in differences in the mechanical phenotype of cells, the mechanical properties of BAM-transduced fibroblasts was measured at similar time points using quantitative deformability cytometry (q-DC), in which the timescale of a cell to transit through a narrow constriction provides a metric for cell deformability[4] (Fig. A3).

This microfluidics-based methodology overcomes the limitation of measuring one cell at a time with conventional measurement techniques, such as micropipette aspiration, atomic force microscopy (AFM) and optical tweezers[5], q-DC enables a measurement in a high-throughput manner. The results showed that cell transit time and stiffness increased by day 1 and was followed by a decrease on day 3 (Fig. A4a-d), which coincided with the observed cytoskeletal changes. AFM was employed for validation and the results showed a similar trend, consistent with q-DC findings, and demonstrated more profound differences in cell stiffness across the various time points. These changes in cellular mechanical properties were transgene-specific as transduction with green fluorescent protein (GFP) did not produce a similar effect (Fig. A4e). These results suggest that the actin cytoskeleton and mechanical properties of cells are modulated during the early phase of reprogramming, possibly playing a role in iN reprogramming.

Methods

For other methods, refer to the methods section in Chapter II.

Quantitative Deformability Cytometry (q-DC)

To perform Quantitative Deformability Cytometry (q-DC), standard soft lithography methods were used to fabricate microfluidic channels in polydimethylsiloxane (PDMS). A mixture of 10:1 ratio of base to crosslinker (Sylgard 184, Dow Corning) was poured onto a master wafer containing bifurcating channels42. After curing, the PDMS device layer was bonded to a No. 1.5 glass coverslip (Thermo Fisher) using plasma treatment (Plasma Etch, Carson City, NV). Within 48 hours of device fabrication, cell suspensions of 1 x 10^6 cells/mL were driven through

constrictions of 9 μm (width) x 10 μm (height) by applying 69 kPa of air pressure. We captured images of cells during deformation through the constrictions using a CMOS camera with a capture rate of 1600 frames/s (Vision Research, Wayne, NJ) mounted on an inverted Axiovert microscope (Zeiss, Oberkochen, Germany) equipped with a 20x/0.4NA objective. To analyze the time-dependent shape changes of individual cells during deformation, we used a custom MATLAB (MathWorks, Natick, MA) code (https://github.com/rowatlab)[4]. To determine the mechanical stresses applied to individual cells, we used devices that had been calibrated with agarose particles of defined elastic modulus as previously described[6]. Stress-strain curves were obtained for single cells and a power-law rheology model was subsequently fitted to the data to yield measurements of elastic modulus, fluidity, and transit time.

Atomic force microscopy (AFM)

To analyze the mechanical property of cells during the direct reprogramming of fibroblasts into neurons, mechanical measurements of single cells were performed using atomic force microscopy (AFM) (Bruker BioscopeResolve, Bruker Corp., USA) with silicon tipless cantilevers (NPO-10, Bruker Corp., USA), a high sensitive cantilever k=0.06 N/m, and sample Poisson's ratio of 0.499 at the UCLA Nano and Pico Characterization Facility. Fibroblasts were transduced with individual or different combinations of the transgenes and then we measured the cell stiffness at various time points during the reprogramming process (e.g. days 0, 1, and 3), wherein for each condition at least 30 cells were analyzed. During the measurements, cells were cultured on a glass bottom dish with pre-warmed PBS and set on a temperature-controlled stage at 37°C. The force-distance curves were recorded and the elastic modulus of cells was calculated by NanoScope Analysis (Bruker Corp., USA) using the Hertz model as the Fit Model. Similar

AFM measurements were also conducted on control samples of non-transduced and GFP-transduced fibroblasts.

References

1. Downing, T.L., et al., Biophysical regulation of epigenetic state and cell reprogramming. Nat Mater, 2013. 12(12): p. 1154-62.

2. Song, Y., et al., Transient nuclear deformation primes epigenetic state and promotes cell reprogramming. Nat Mater, 2022. 21(10): p. 1191-1199.

3. Vierbuchen, T., et al., Direct conversion of fibroblasts to functional neurons by defined factors. Nature, 2010. 463(7284): p. 1035-41.

4. Nyberg, K.D., et al., The physical origins of transit time measurements for rapid, single cell mechanotyping. Lab Chip, 2016. 16(17): p. 3330-9.

5. Song, Y., et al., Cell engineering: Biophysical regulation of the nucleus. Biomaterials, 2020. 234: p. 119743.

6. Nyberg, K.D., et al., Quantitative Deformability Cytometry: Rapid, Calibrated Measurements of Cell Mechanical Properties. Biophys J, 2017. 113(7): p. 1574-1584.

Figures

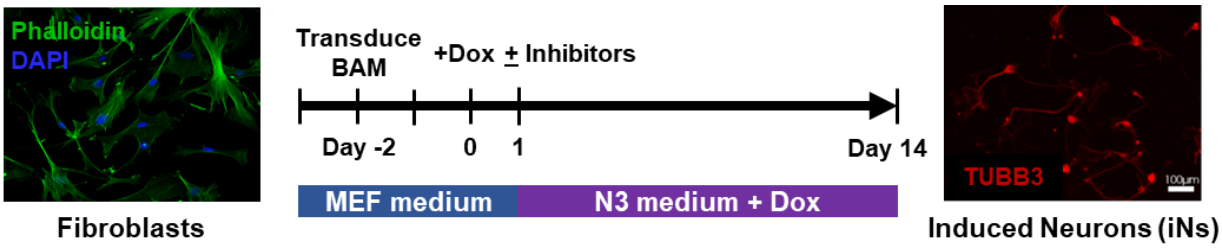

Fig. A1. iN reprogramming protocol.

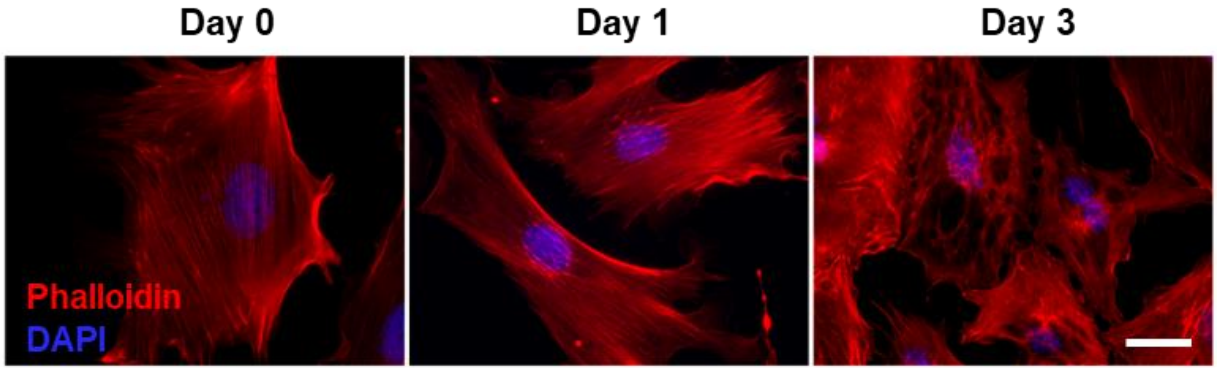

Fig. A2. Changes on actin during cell reprogramming. Representative images show fluorescence micrograph of the actin network (phalloidin, red) and nucleus (DAPI, blue) in BAM-transduced fibroblasts at the indicated time points. Scale bars, 20 μm.

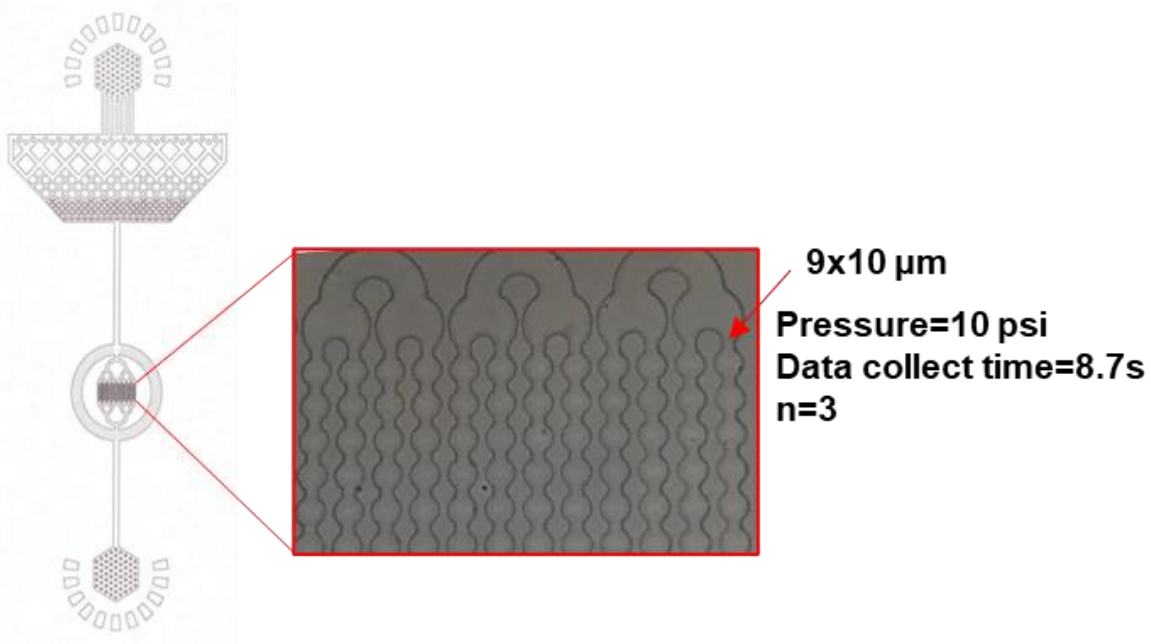

Fig. A3. Design of q-DC. Image of the microfluidics device that enables single cells to transit through micro-constrictions under specific pressure. (9 µm × 10 µm, 10 psi).

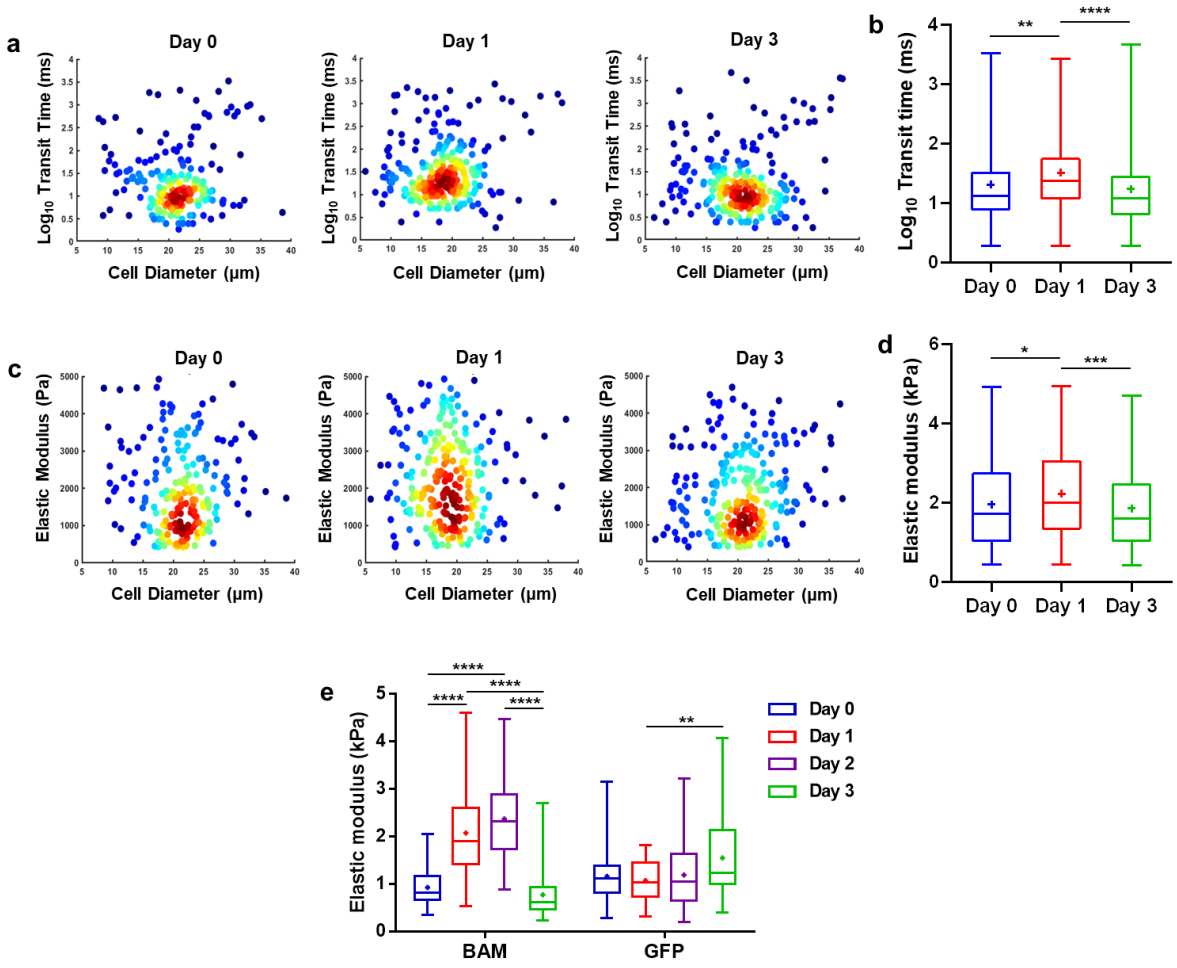

Fig. A4. Changes on mechanical properties of cells during reprogramming. (a) Density scatter plots show the log of transit time as a function of cell diameter for BAM-transduced fibroblasts deforming through 9 μm × 10 μm constrictions at the indicated time points (day 0, n= 211; day 1= 257; day 3, n= 253). Dots represent single-cell data. (b) Box plots illustrate the log of transit time of BAM-transduced fibroblasts at the indicated time points (day 0, n = 211; day 1 n = 257; day 3, n = 253) as derived by q-DC. (c) Density scatter plots show the elastic modulus as a function of cell diameter for BAM transduced fibroblasts deforming through 9 μm × 10 μm constrictions at the indicated time points (day 0, n= 211; day 1 n= 257; day 3, n=253). Dots represent single-cell data. (d) Box plots illustrate the elastic modulus of BAM-transduced

fibroblasts at the indicated time points (day 0, n = 211; day 1 n = 257; day 3, n = 253) as derived by q-DC. (e) Box plots illustrate the variation in elastic modulus of BAM- or GFP-transduced fibroblasts at the indicated time points as acquired using AFM, where GFP serves as a control. The number of biological replicates, n, was equal to 55 per condition.